# Toward Adaptive Planar Magnetic Levitation Systems for Variable Load Transport: Design and Estimation Strategies

by

Ridwan Bari

A thesis
presented to the University of Waterloo
in fulfillment of the
thesis requirement for the degree of
Master of Applied Science
in
Mechanical and Mechatronics Engineering

Waterloo, Ontario, Canada, 2025

© Ridwan Bari 2025

## Author's Declaration

I hereby declare that I am the sole author of this thesis. This is a true copy of the thesis, including any required final revisions, as accepted by my examiners.

I understand that my thesis may be made electronically available to the public.

## Abstract

Magnetic levitation offers unique advantages for industrial automation—frictionless actuation, silent operation, and fully decoupled multi-degree-of-freedom (DOF) motion—but these benefits are often offset by practical challenges in real-world deployment. In particular, sensitivity due to misalignment in mover and stator magnetic fields, manufacturing tolerances, and external disturbances from variable payloads. These limitations make it difficult to deploy levitation platforms in dynamic environments where the mass and location of transported objects cannot be tightly controlled. Motivated by a growing demand for intelligent transport systems in flexible manufacturing lines and collaborative robotic workcells, this research presents the development of an adaptive control strategy for planar magnetic levitation systems capable of estimating unknown payload mass and center-of-mass location data in real time. Performance in the face of variable payloads maintains stability and preserves control performance across a wide range of operating scenarios.

An adaptive linear quadratic regulator (ALQR) framework was implemented on two planar Halbach-array-based mover units—one with a 6-pole configuration and another with a 5-pole layout. The control architecture incorporates online parameter estimation to recover payload characteristics from force and torque measurements without requiring extensive prior calibration or external measurements of the load. This enables the system to dynamically compensate for mass disturbances and maintain control accuracy across varying operating conditions.

Experimental validation shows that the 5-pole array achieves an average payload mass estimation error of less than 2% of the true value, with the payload's center of mass localized within $\pm 1.9$ cm. For the 6-pole mover array, the average mass estimation error is below 4%, and the location estimation error is within $\pm 0.5$ cm. These results varied across multiple stator locations and mover configurations. A series of experiments—including sequential payload loading, off-center placement, and mid-trajectory dynamic loading—demonstrated the estimator's robustness and its resilience to transient noise and visual occlusion artifacts. To support consistent estimator performance across the stator, a compensation method was developed to account for geometric deviations in the stator. This included a payload mass offset profile derived through iterative calibration, which enables accurate levitation and estimation throughout the workspace without relying on predefined lookup tables. When tracking motion trajectories, the adaptive controller and mass offset profile significantly reduced steady-state error in the payload mass estimation following load application—from 25% to below 3%—and improved vertical and yaw response times when compared to a fixed-parameter LQR control scheme.

Together, these contributions demonstrate a magnetic levitation platform suitable for collaborative and flexible automation tasks. The system adapts to unknown payloads in real time, estimates key inertial parameters during operation, and maintains performance without requiring redesign or calibration for each payload. These capabilities form a foundation for future research in multi-agent manipulation, intelligent load sharing, and sensorless coordination in levitated transport systems.

**Acknowledgements**

I would first like to express my sincere gratitude to my supervisor, Dr. Behrad Khamesee, whose vision, guidance, and patience have been instrumental in shaping my growth as a researcher. His unwavering support and encouragement have been invaluable, and I am deeply grateful for the opportunity to learn under his mentorship.

I would also like to express my sincere thanks to the members of the Maglev Microrobotics Laboratory for their technical support, collaborative spirit, and the many insightful discussions I enjoyed during my time in the lab. I am especially grateful to the PhD students—Yang (Bob) Wang, Chanuphon (Cha) Trakarnchaiyo, and Zhenchuan (Daniel) Xu—for their invaluable guidance and patience in answering all my questions. To the rest of the team—Joseph Nofech, Afarin Khabbazian, Sebastian Viancha, Yufeng (Hugo) Huang, Anderson Borja Velez, and Mahdi Naserzad—thank you for the engaging debates, shared laughter, and unwavering dedication.

Finally, I extend my sincere appreciation to the RoboHub staff for their operational support and guidance, especially Robert Wagner, Dr. Brandon DeHart, and Dr. Alexander Werner.

## Dedication

This is dedicated to my family, without whose support I would not be here today.

# Table of Contents

**Author's Declaration** ii

**Abstract** iii

**Acknowledgements** v

**Dedication** vi

**List of Figures** xi

**List of Tables** xv

**List of Abbreviations** xvi

**1 Introduction** 1

1.1 Introduction to Magnetic Levitation . . . . . 1

1.2 Industrial Applications . . . . . 4

1.2.1 General Applications . . . . . 4

1.2.2 Application to Flexible Manufacturing . . . . . 5

1.3 Objectives and Contributions . . . . . 7

1.3.1 Main Objectives . . . . . 8

1.3.2 Contributions . . . . . 9

1.4 Thesis Outline . . . . . 10

**2 Literature Review** **11**

2.1 Repulsive Levitation Stages . . . . . 11

2.2 Attractive/Rotary Levitation Stages . . . . . 15

2.3 Modeling Methods . . . . . 17

2.4 Secondary Functions and Control Algorithms . . . . . 19

**3 Related Background Theory** **22**

3.1 Magnet Properties and Halbach Arrays . . . . . 22

3.2 Coordinate Systems and Transformations . . . . . 25

3.3 Magnetic Modeling . . . . . 28

3.3.1 Lorentz Force and Torque . . . . . 28

3.3.2 Magnetic Nodes . . . . . 29

3.3.3 Real Time Method . . . . . 32

3.4 Adaptive Control & Linear Quadratic Controllers . . . . . 36

3.4.1 System and Parameter Identification (PI) . . . . . 36

3.4.2 Parameter Identification Algorithms and Modifications . . . . . 37

3.4.3 Adaptive LQR Control and Error Tracking Formulation . . . . . 39

3.4.4 Discrete Derivative and Integration . . . . . 42

**4 Electromagnetic Hardware Design** **45**

4.1 Stator Assembly . . . . . 45

4.1.1 Electromagnetic Coil Design . . . . . 46

4.2 Mover Units . . . . . 48

4.2.1 Force and Torque Zones . . . . . 50

4.2.2 Maximum Weight of Payload . . . . . 52

4.3 Measurement and Control System . . . . . 57

**5 Software Design** **59**
5.1 Coil and Current Management . . . 59
5.1.1 Active Coil Selection . . . 59
5.1.2 Direct Wrench Decoupling . . . 60
5.1.3 Current Recalculation . . . 62
5.1.4 Coil Measurement Adjustment . . . 65
5.2 Control Strategies . . . 68
5.2.1 Derivative Adjustment . . . 68
5.2.2 Adaptive Control Parameterization . . . 68
5.3 Other Software Features . . . 75
5.3.1 Calibration and Mass Compensation . . . 75
5.3.2 End User Upgrades . . . 77

**6 Results and Discussion** **79**
6.1 Experiment 1: Single Mass Loading . . . 79
6.2 Experiment 2: Sequential Mass Loading . . . 84
6.3 Experiment 3: Offset Mass Loading . . . 88
6.4 Experiment 4: Mass Loading During Trajectory Tracking . . . 92

**7 Conclusion and Future Work** **95**
7.1 Conclusion . . . 95
7.2 Future Work . . . 97

**References** **99**

**APPENDICES** **107**

**A Additional Plots** **108**
A.1 Maximum Payload Mass Analysis - Supplementary Plots . . . 108
A.2 Experiment 2 - Alternative Stator Locations . . . 111

**B Mathematical Definitions** **115**

B.1 Statistical Measures . . . . . 115

# List of Figures


1.1 Existing magnetically levitated planar motor platforms at the University of Waterloo. . . . 3

1.2 Omni-directional conveying solution produced by Omnia Wheel Ltd.. . . . 6

1.3 Examples of existing commercially available magnetically levitated planar motor systems developed for industrial applications. . . . 7

2.1 Examples of repulsive magnetic levitation stages from key studies. . . . 14

2.2 Long-stroke repulsive levitation stage utilizing a herringbone stator coil arrangement and a 2D Halbach mover array. . . . 14

2.3 Examples of rotary levitation stages in literature . . . 16

2.4 Magnetic levitation stage utilizing attractive forces to achieve stable suspension of a microrobot. . . . 16

2.5 Diagrams of various magnetic field modeling methods. . . . 18

2.6 Example of a magnetic suspension mass comparison device. . . . 20

2.7 Examples of automatic weighing functions for industrial applications. . . . 21

3.1 Flux lines and magnetization vectors in a 1D linear Halbach array. Areas of denser flux lines correlate with increased **B** field strength. . . . 24

3.2 Magnetization vectors and relevant parameters depicted for a 2D planar Halbach array. . . . 25

3.3 Top-down view schematic illustrating the coordinate frames used in the Maglev system. . . . 27

3.4 Side view schematic illustrating the coordinate frames used in the Maglev system. . . . 27

3.5 Illustration of the coil conductor model. . . . . 27
3.6 Magnetic node distribution for single and multi-magnet configurations. . . 29
3.7 Permanent magnet with a horizontally aligned magnetization vector . . . . 31
3.8 Magnetic node representation of a permanent magnet with a horizontally aligned magnetization vector. . . . . 31
3.9 Block diagram representation of the Maglev system. . . . . 43

4.1 Multiple perspectives of TestBench, the rapid testing planar magnetic levitation platform located in the Maglev Microrobotics Laboratory. . . . . 46
4.2 Design of a single electromagnetic coil. Detailed dimensions are provided in Table 4.1. . . . . 47
4.3 Actual coil located within stator. . . . . 48
4.4 6-pole 2D Halbach magnetic mover unit. *Left:* Perspective view of the assembled mover unit. *Right:* Schematic showing the magnetization vectors of each permanent magnet, viewed from the bottom (i.e., bottom of the mover facing the observer). . . . . 49
4.5 5-pole 2D Halbach magnetic mover unit. *Left:* Perspective view of the assembled mover unit. *Middle:* Bottom view of the assembled mover unit. The bottom is covered in a clear epoxy. *Right:* Schematic showing the magnetization vectors of each permanent magnet, viewed from the bottom (i.e., bottom of the mover facing the observer). . . . . 50
4.6 Magnetic flux density comparison between the magnetic node and harmonic models for the 5-pole mover. . . . . 51
4.7 Magnetic flux density comparison between the magnetic node and harmonic models for the 6-pole mover. . . . . 51
4.8 Bottom view of the designated regions for computing force and torque distributions under both Halbach arrays. . . . . 52
4.9 Top-down schematic of the stator assembly. The shaded green area denotes the evaluation region. Due to the symmetry of the stator layout in the $x$-$y$ plane, performance metrics computed within this region are representative of the entire working area. . . . . 53
4.10 Number of saturated coils as a function of payload mass for each mover. . . 54

4.11 Maximum supported payload as a function of the mover's levitation height. 55
4.12 Maximum coil current and corresponding number of saturated coils across various stator locations for each mover configuration. . . . . 56
4.13 Profile view of the 5-pole mover, showing the z-direction offset distance ($d_{offset}$) from the center marker to the desired object reference frame. . . . 58
4.14 Hardware configuration of the TestBench Maglev system. . . . . 58

5.1 Coil activation for various positions and yaw orientations of the mover unit. 60
5.2 Idealized coil height adjustment from a curved mover. . . . . 65
5.3 Measured curvature profile of the 5-pole Halbach array obtained through experimental mapping. A projection of a flat magnet array is shown below. 66
5.4 Delaunay triangulation of measured surface points for interpolating vertical z-offsets resulting from the 5-pole Halbach array's top-plate curvature. . . . 67
5.5 Exaggerated side view of the 5-pole Halbach array, illustrating its surface curvature and annotated with relevant geometric quantities. . . . . 67
5.6 Free body diagram of payload center loading. Forces in the z-direction are only shown. . . . . 69
5.7 Free body diagram of payload offset loading. . . . . 72
5.8 Complete user interface for monitoring and controlling the magnetic levitation system. . . . . 77
5.9 Zoomed in view of the user interface illustrating elements that enhance usability and operator interaction. . . . . 78

6.1 Payloads used throughout experiments. . . . . 80
6.2 Example of center loading on the 6-pole Halbach mover, levitated at a height of 6 mm. . . . . 81
6.3 Summary of mass loading performance at three stator locations for the 6-pole Halbach mover. . . . . 82
6.4 Summary of mass loading performance at three stator locations for the 5-pole Halbach mover. . . . . 83
6.5 Summary of successive mass loading performance when the 6-Pole Halbach is between 4 coils. . . . . 86

6.6 Summary of successive mass loading performance when the 5-Pole Halbach is above a single coil. . . . . 87
6.7 Example of side loading on the 5-pole Halbach mover, levitated at a height of 7 mm. A plastic spacer is used to constrain the load's center of mass within a smaller, well-defined area. . . . . 88
6.8 Summary of loading location estimates for the 6-pole Halbach mover. . . . 90
6.9 Direct parameter estimate curves at loading location (11 cm, 10.5 cm) for the 6-pole Halbach array. . . . . 90
6.10 Summary of loading location estimates for the 5-pole Halbach mover. . . . 91
6.11 Direct parameter estimate curves at loading location (5.0 cm, 8.0 cm) for the 5-pole Halbach array. . . . . 91
6.12 Mass offsetting profile for a rectangle trajectory . . . . . 92
6.13 Control signals for the 6-Pole Halbach mover during the rectangle trajectory tracking. . . . . 93
6.14 Mass loading curve while the mover is tracking a rectangle trajectory for the 6-Pole Halbach mover . . . . . 93

A.1 Extended plots for the 5-pole mover showing the maximum coil current, # of saturated coils, and power consumption when levitating a load mass at various stator locations. . . . . 109
A.2 Extended plots for the 6-pole mover showing the maximum coil current, # of saturated coils, and power consumption when levitating a load mass at various stator locations. . . . . 110
A.3 Summary of successive mass loading performance when the 5-Pole Halbach is between 2 coils. . . . . 111
A.4 Summary of successive mass loading performance when the 5-Pole Halbach is between 4 coils. . . . . 112
A.5 Summary of successive mass loading performance when the 6-Pole Halbach is between 2 coils. . . . . 113
A.6 Summary of successive mass loading performance when the 6-Pole Halbach is above a single coil. . . . . 114

B.1 Behavior of the MAPE and MAAPE statistical measures. . . . . 116

# List of Tables


3.1 Common terminology related to magnetic materials. . . . . 23

3.2 Computation times (in seconds) for calculating the forces and torques on two mover units using different methods. . . . . 35

3.3 Relevant equations to the control blocks present in the overall control block diagram (given in Figure 3.9). . . . . 44

4.1 Dimensions of the rounded square coils used in the TestBench for generating the levitation field. . . . . 47

4.2 Mover unit properties . . . . . 49

5.1 6-Pole Halbach adaptive linear quadratic regulator (ALQR) control parameters for each motion axis. . . . . 74

5.2 5-Pole Halbach ALQR control parameters for each motion axis. . . . . 75

5.3 Deviation between calibrated mover mass and torque offset from their true values at representative stator locations. . . . . 76

6.1 Summary of real-time estimation results for payload mass and center-of-mass location during levitation experiments. . . . . 94

# List of Abbreviations

**ALQR** adaptive linear quadratic regulator xv, 7, 9, 42, 44, 68, 74, 75, 92, 97

**ARE** Algebraic Riccati Equation 39

**DOF** degrees of freedom 2, 6, 12, 13, 18–20, 60, 68

**EPM** Electro-Dynamic Planar Motor 12

**ERS** European Remote Sensing 4

**LQR** linear quadratic regulator 39, 40, 68, 92

**MAAPE** mean arctangent absolute percentage error 9

**MAPE** mean absolute percentage error 9, 80, 84, 85

**MLPM** magnetically levitated planar motor 2, 3, 5, 6, 10, 13, 25

**MSB** magnetic suspension balance 19, 85

**PCB** printed circuit board 15

**PI** parameter identification 37

**PID** Proportional–Integral–Derivative 20

**RMS** root mean square 15

**SISO** single-input single-output 68

**SPM** static parametric model 36, 37, 70, 73, 76

**SPOT** Satellite Pour l'Observation de la Terre 4

*In other words, to put it into Euclid, or old-fashioned plane geometry, a straight line is not the shortest distance between two points.*

MADELEINE L'ENGLE
A WRINKLE IN TIME (1962)

# Chapter 1

# Introduction

## 1.1 Introduction to Magnetic Levitation

From the hoverboards of *Back to the Future* to high-speed bullet trains, the idea of objects floating freely above the ground has long captured the imagination. What once belonged to science fiction is now a field of active engineering research: magnetic levitation. Since the 1970s, magnetic levitation—or simply Maglev—has been a focal point in efforts to reduce the friction inherent in mechanical systems. Modern Maglev systems rely on various combinations of magnetic components—such as electromagnets and permanent magnets—and materials like superconductors and non-ferromagnetic metals to generate the electromagnetic forces needed to achieve stable, controllable levitation. This seamless control over contactless motion now underpins a growing class of advanced mechanical systems, from high-speed transit to next-generation motion platforms.

Magnetic levitation represents a groundbreaking technology due to its capability to facilitate friction-free movement. This technology eliminates contact forces between moving surfaces, thereby minimizing or completely preventing wear and tear on mechanical components. As a result, the durability of these components is significantly enhanced, leading to reduced maintenance and repair costs over time. The friction-free environment created by magnetic levitation also plays a crucial role in reducing the generation of particulate matter caused by mechanical rubbing, making it particularly suitable for applications requiring a clean room environment. The absence of friction enables higher speeds to be achieved with lower energy consumption—as exemplified by magnetically levitated trains. Additionally, the reduced wear on components contributes to increased safety and reliability, as it minimizes the likelihood of mechanical failures. Compared to traditional systems,

magnetically levitated systems also exhibit lower noise levels, thereby positively impacting the health and safety of individuals working in proximity to these systems.

This technology has demonstrated transformative impacts across a spectrum of applications, ranging from small-scale manufacturing, such as in the semiconductor industry, to large-scale transportation systems like railways. In small-scale manufacturing, magnetic levitation has revolutionized photolithography in semiconductor manufacturing by enabling precise handling and positioning of delicate materials, leading to advancements in manufacturing efficiency, reliability, and product quality. On a larger scale, magnetic levitation has significantly influenced transportation systems, particularly in the development of high-speed Maglev trains. These trains utilize magnetic levitation to achieve ultra-smooth and efficient movement without physical contact with rails, offering faster travel speeds and reduced operational costs compared to conventional rail systems. The adoption of magnetic levitation in both small and large-scale applications underscores its versatility and transformative potential across various industries.

While magnetic levitation systems span a wide range of scales and applications, this research targets an intermediate class: motion platforms that can transport objects precisely, repeatedly, and autonomously across a flat workspace, such as those found on factory floors. Specifically, this research focuses on macro-scale magnetically levitated planar motors (MLPMs) employing repulsive-type electromagnetic levitation. This technology involves a flat planar stator composed of square electromagnetic solenoids with rounded corners, accompanied by movers embedded with an array of permanent magnets. The movers are actuated by the stator coils and can achieve six degrees of freedom (DOF) motion: translational motion described by (x, y, z) coordinates, and rotational motion described by ($\alpha$, $\beta$, $\gamma$) angles.

Within the Maglev Microrobotics Laboratory at the University of Waterloo, two MLPM platforms are operational. The first—known as TestBench—is a $2' \times 2'$ rapid development platform containing a stator module with 64 electromagnetic coils covered by an aluminum sheet. Various movers can be positioned on this platform and sensing of the mover's position and orientation is facilitated by four infrared motion tracking cameras. The second platform is a larger $6' \times 8'$ system comprising eight stator modules that are similar to the module in TestBench. This platform, named "Maglev Floor", or simply MagFloor, houses nearly 800 electromagnets and can be lowered to floor level through the built-in hydraulic lift. The larger footprint of MagFloor enables the execution of multi-mover trajectories and collaborative robotics tasks. Both platforms use the same four-camera motion capture tracking systems and reduce the temperature of the electromagnetic coils by passing air across them. All electronics are housed in the base of the support structures to avoid interference with the magnetic field generated by the coils, keeping the working area free

of obstructions.

These platforms within the laboratory are instrumental in investigating and advancing the capabilities of macro-scale magnetically levitated planar motors. These motors can form the basis of larger manufacturing systems that require the precise manipulation of large payloads, making them invaluable for improving the control, automation, and flexibility of existing systems. MLPMs offer unique opportunities for research in optimizing manufacturing techniques, expanding collaborative robotics tasks, and mitigating the impact of friction in existing systems. By leveraging the wide range of configurations and numerous capabilities of MLPMs, researchers can design, test, and deploy systems that push the boundaries of current robotic technologies, such as autonomous assembly lines and multi-robot cooperation in shared environments.

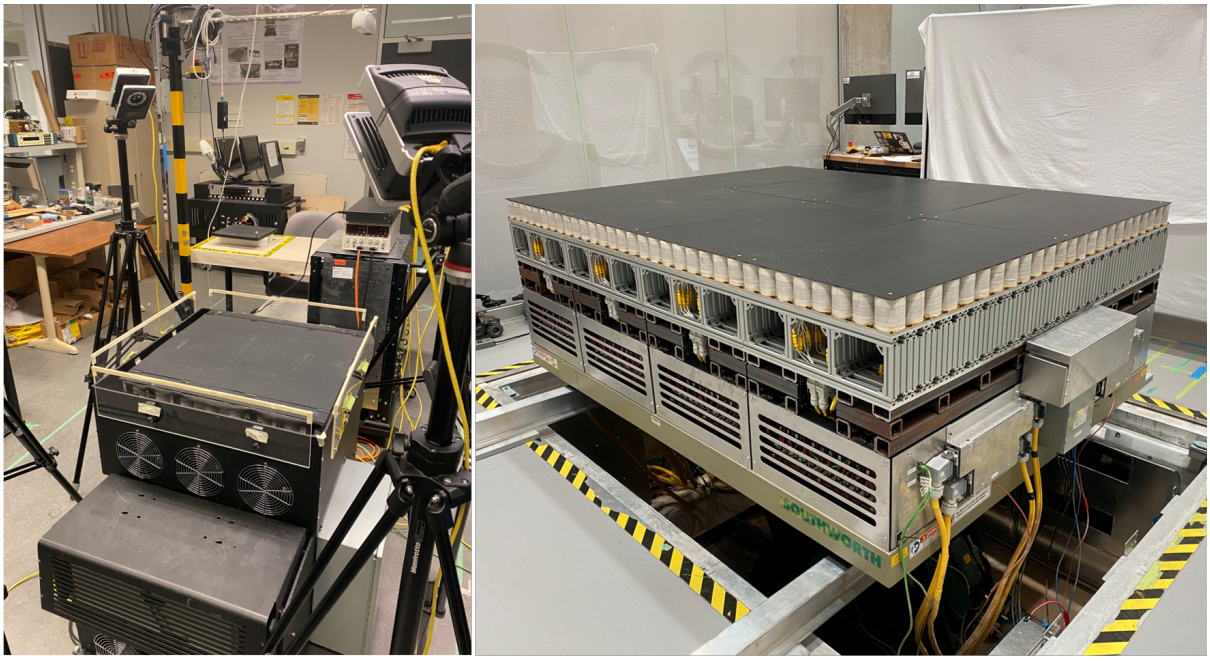



Figure 1.1: Existing magnetically levitated planar motor platforms at the University of Waterloo. *(Left)* Small-scale planar motor platform, *TestBench*, containing 64 electromagnetic coils with four motion capture cameras. *(Right)* Large-scale planar motor platform, *MagFloor*, lifted to the highest position. The height of the MagFloor can be lowered to match the level of the surrounding floor.

## 1.2 Industrial Applications

### 1.2.1 General Applications

Extending far beyond academic research, magnetic levitation has profoundly impacted various industries ranging from aerospace to medicine. In aeronautical and aerospace applications, magnetically levitated bearings have replaced traditional bearings in turbines and attitude control reaction wheels—such as those used in the first three SPOT satellites in the mid-1980s and later in the ERS satellites in the early 1990s [1, 2]. When compared to traditional rolling or sleeve bearings, these magnetically levitated systems eliminate the need for lubrication, maintain functionality at extreme temperature conditions, and enable active control of the bearing position [3]. Moreover, companies such as *MagLev Aero* have proposed rotor systems that utilize magnetic suspension to improve energy delivery, increase thrust efficiency, and reduce noise throughout the operation of rotary-wing aircrafts [4]. In the medical field, magnetic levitation is advancing biomedical research by levitating cells to measure their density and establish unique levitation profiles for different cell types [5, 6]. This technology holds great promise for advancing diagnostic capabilities, potentially leading to the development of low-cost, rapid, and portable diagnostic tools [5]. Particularly in regions where traditional imaging methods are impractical or prohibitively expensive, magnetic levitation can help improve healthcare accessibility and affordability.

In the category of long-range transportation, magnetic levitation technology has become a key driver in the development of high-speed trains—colloquially known as *Maglev Trains*. Over large distances, Maglev trains achieve frictionless movement at remarkable speeds to produce efficient and environmentally friendly transportation solutions [7]. With a maximum commercial speed of 460 km/h, *Shanghai Maglev* currently holds the speed record among public transportation systems using such technology[1] [8]. At a much smaller scale, however, magnetic levitation also plays a critical role in advanced semiconductor manufacturing processes. The precise positioning and control enabled by magnetic levitation are essential for the rapid and accurate movements required in photolithography [9]. This facilitates the production of increasingly smaller-scale transistors required in modern-day processors. While magnetic levitation has proven effective at both large and small scales, current research increasingly focuses on its potential to enhance the flexibility and expandability of intermediate-scale systems in broader manufacturing contexts.

[1] While there have been demonstrations and proposals for faster trains, China operates the most widely used magnetically levitated train system. Covering a distance of 30 km, *Shanghai Maglev* shuttles passengers from Shanghai Pudong International Airport directly to the city center (Longyang Road station) in just about eight minutes!

### 1.2.2 Application to Flexible Manufacturing

Historically, manufacturing layouts have been largely dominated by systems that are highly specialized and rigid; such specialized workflows excel at producing a limited range of products in a single factory. Products typically move along conveyor belts to dedicated, specialized equipment in a largely linear sequence. Consequently, equipment failures, evolving market demands, and changing business objectives make existing manufacturing set-ups extremely difficult and time consuming to modify. Incorporating flexible manufacturing principles early in the process design can be pivotal for companies to address these challenges in a timely and cost-effective manner. The concept of flexible manufacturing involves creating systems that rapidly adjust to disruptions and shifting production requirements to reduce factory downtime and increase product variety.

Traditional mechanical conveyor belt systems in modern-day manufacturing are plagued by issues such as excessive vibrations, noise, high maintenance costs, and limited adjustability. In the era of flexible manufacturing, these shortcomings severely hinder the adaptability of production systems to meet the diverse and complex needs of modern companies. A crucial aspect of successful flexible manufacturing lies in routing flexibility, expansion flexibility, and material handling flexibility [10]. Routing flexibility involves allowing products to take alternative routes in the manufacturing process without significantly affecting performance outcomes [11]. Expansion flexibility refers to the ease of system expansion in a modular manner [12]. Material handling flexibility pertains to efficiently positioning and moving different process components within the manufacturing facility [13]. Conveying systems that can incorporate these aspects into a manufacturing process would allow companies to be more agile in meeting their objectives.

Current solutions aimed at achieving these flexibility aspects often utilize omnidirectional conveying platforms, such as those shown in Figure 1.2. These platforms typically feature omnidirectional wheels—wheels capable of moving forward, backward, and laterally—integrated into manufacturing tables. Each wheel contained in the table can be independently powered, enabling translational and rotational positioning of objects within the plane. This provides a straightforward solution that can be incorporated throughout existing conveyor belt systems. Omnidirectional platforms are characterized by their lightweight design, cost-effectiveness, and inherent modularity, making them superior alternatives to traditional conveyor belt systems. If the objects to be moved are sensitive to friction-induced wear or require cleanroom standards, contact-based solutions such as omnidirectional tables, however, are wholly inadequate. Replacing these omnidirectional conveyors with MLPMs, similar to those used in this research, combines the advantages of omnidirectional platforms with the transformative benefits of Maglev technology.




Figure 1.2: Omni-directional conveying solution produced by Omnia Wheel Ltd.. Image from [14].

Industrial systems that incorporate Maglev planar motors would provide friction-free motion throughout the conveying of objects, significantly reducing the wear and tear on equipment. They would reduce the noise produced when compared to traditional conveyor belts. As well, these platforms would offer full six DOF motion, allowing precise control and manipulation of objects in all translational and rotational axes. This level of precision control makes magnetically actuated platforms suitable for advanced machining operations, akin to photolithography, on a larger scale. Figure 1.3 highlights some magnetically levitated planar motors currently produced throughout industry.

Magnetically levitated planar motors offer a compelling foundation for designing flexible manufacturing systems that minimize production downtime, increase operational efficiency, and deliver greater precision in handling materials for modern manufacturing. Building on these capabilities, this thesis addresses key limitations in existing MLPMs through novel design and control structures aimed at increasing the adaptability of systems utilizing these motors, with the ultimate goal of establishing a framework for broader adoption of Maglev technology in flexible manufacturing contexts.

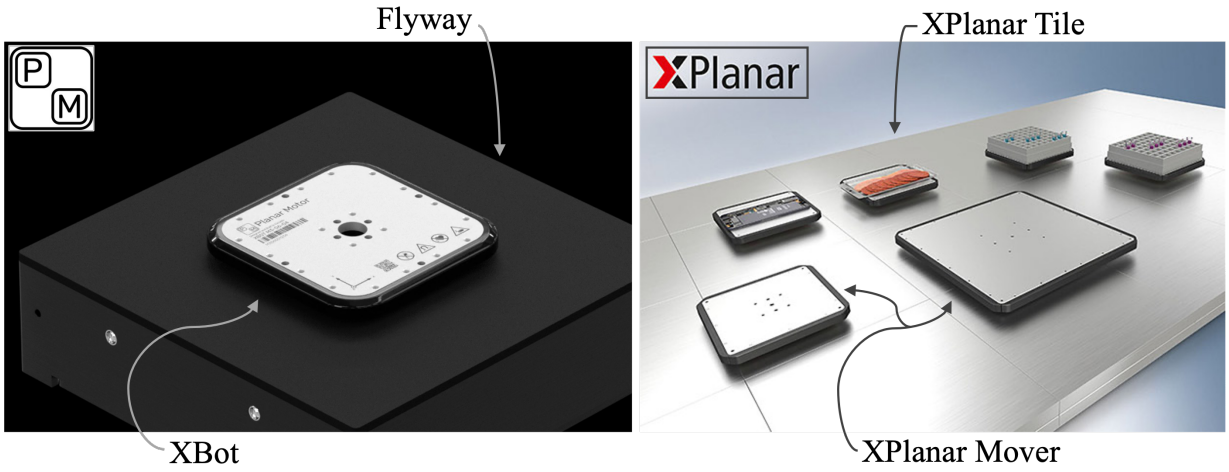



Figure 1.3: Examples of existing commercially available magnetically levitated planar motor systems developed for industrial applications. (*Left*) The XBot system from Planar Motor Inc.. Image adapted from [15]; (*Right*) The XPlanar platform developed by Beckhoff Automation Ltd.. Image adapted from [16].

## 1.3 Objectives and Contributions

The research presented in this thesis focused on the development of an adaptive control strategy for real-time payload estimation. The ALQR controller is aimed at enhancing system performance when key payload parameters—specifically, mass and loading location—are unknown. This strategy was implemented and evaluated using two planar magnetic levitation mover units that are based on a 2D Halbach magnet array configuration: an existing 6-pole layout and a novel 5-pole layout. In the process of manufacturing the 5-pole Halbach mover, strong internal magnetic forces introduced a curvature across the array surface, necessitating the development of a compensation technique to correct for these deviations in the magnetic field model.

The original design and real-time model of both 2D Halbach array movers were developed by Dr. Zhenchuan Xu. The assembly of the 6-pole mover was done by Dr. Zhenchuan Xu and Curtis Stewart; the assembly of the 5-pole mover was carried out by Dr. Zhenchuan Xu, Dr. Chanuphon Trakarnchaiyo, and myself. My contributions focused on completing the construction of the mover, integrating the mover units into the levitation platform, and designing the adaptive control strategies and payload estimation and compensation techniques used throughout this work.

### 1.3.1 Main Objectives

The main objectives of this research are as follows:

**O1:** Evaluate the performance of a planar magnetic levitation platform using a novel 5-pole 2D Halbach array mover.

- (a) Construct and integrate the 5-pole Halbach mover into the existing planar stator system.
- (b) Compare its levitation and load-handling performance to the previously developed 6-pole Halbach configuration.
- (c) Characterize its magnetic field distribution through both experimental measurements and finite element simulations.

**O2:** Develop a real-time adaptive control framework capable of estimating unknown load mass and location during levitation.

- (a) Derive an estimator based on a simplified model that identifies changes in vertical force and rotational torque during disturbances.
- (b) Implement online identification to estimate mass, center-of-mass offset, and inertial contributions from unknown payloads.

**O3:** Assess estimator accuracy and control performance across a variety of experiments designed to test loading dynamics.

- (a) Measure estimator robustness in single, sequential, and off-center loading scenarios.
- (b) Analyze response time, absolute error, and minimum resolvable load across both Halbach configurations.
- (c) Evaluate the adaptive control scheme under dynamically loaded trajectory tracking.

**O4:** Lay the foundation for collaborative applications by enabling generalized load handling across arbitrary stator positions.

- (a) Enable on-the-fly calibration of force and torque offsets across the stator workspace.
- (b) Demonstrate repeatable estimation without the need for predefined calibration tables.

### 1.3.2 Contributions

The major contributions of this thesis are as follows:

**C1:** Implemented and experimentally validated a real-time estimation scheme for unknown payload and center-of-mass location on a planar Halbach-array-based magnetic levitation system.

An ALQR control framework was developed, incorporating online parameter estimation to identify payload characteristics during levitation without requiring prior calibration. The approach achieved accurate mass estimation within 2% error and localized the center of mass within ±1.9 cm across various mover positions on the stator.

**C2:** Developed a methodology for comparative evaluations between a previously developed 6-pole Halbach mover and a newly integrated 5-pole Halbach configuration.

By varying both the payload mass and loading location, this work quantified differences in estimator sensitivity, resolution, and control behaviour across magnetic field distributions and stator locations, using mean absolute percentage error (MAPE), mean arctangent absolute percentage error (MAAPE), and absolute difference metrics. The 5-pole mover exhibited superior payload mass estimation fidelity in most loading regimes, while the 6-pole array demonstrated finer sensitivity in the payload loading location.

**C3:** Developed a payload mass and torque offset compensation method to improve estimation repeatability across the stator workspace.

Rather than relying on static lookup tables, the system uses local calibration and iterative learning to build force and torque offset profiles. This method enables consistent estimator performance even under mover and stator irregularities, such as coil height variation and mover top plate curvature.

## 1.4 Thesis Outline

The rest of this thesis is outlined as follows:

In Chapter 2, the existing literature on magnetically levitated motion platforms is reviewed. The chapter characterizes the various categories of levitation stages and outlines the established methods for modeling the magnetic fields of constituent elements. It concludes with a critical analysis of control strategies used in modern magnetic levitation systems, identifying strengths, limitations, and potential opportunities for improvement.

Chapter 3 establishes the theoretical foundation for understanding the operating principles of MLPMs. It begins with a general overview of key terminology related to magnetic materials and common permanent magnet arrangements. The discussion then defines the coordinate systems used to characterize the platform and examines the relevant electromagnetic theory—including magnetic field modeling, principles of force and torque generation, and a real-time model formulation suitable for control. The chapter concludes with a detailed description of adaptive controller theory, laying the groundwork for subsequent controller design.

Chapter 4 focuses on the design aspects of the electromagnetic hardware components comprising the magnetic levitation system implemented in this research. It details the design considerations and specifications for the stator, movers, and position feedback sensing system. This chapter also presents an analysis of the maximum payload capacity of the movers and concludes with a high-level overview of the hardware feedback cycle that governs the operation.

Chapter 5 discusses the software design and implementation of controllers for the magnetic levitation system. It covers axis-specific parameter estimation techniques, the validity of assumptions, and constraints associated with the controller design. It also presents a current-force decoupling strategy used to simplify the control architecture. The chapter concludes with a description of end-user upgrades aimed at improving system usability.

Chapter 6 presents the experimental findings from the implemented adaptive magnetic levitation system. It describes the primary experimental setups investigated, analyzes and interprets the accuracy of the payload estimation scheme, and discusses the performance under various operating conditions. Finally, Chapter 7 summarizes the key findings and contributions of the thesis. It also offers insights into potential directions for future research.

# Chapter 2

# Literature Review

Magnetic levitation systems are widely studied throughout academia and implemented across a variety of scales, depending on their intended applications. While most systems are categorized as either a repulsive levitation system or an attractive levitation system– where repulsive is simply regarded as levitation and attractive as suspension–nine distinct electromagnetic methods are commonly used to support, move, or rotate masses [17]. Some of these include levitation from forces generated by the eddy current induced on a conducting body from varying magnetic fields [18]; levitation using superconducting materials and permanent magnets [19, 20]; levitation between magnetic fields and diamagnetic materials [21]; rotating bodies using forces acting on a current carrying linear conductor in a magnetic field [22]; or even, suspension using a DC electromagnet and the attractive forces between magnetized bodies [23]. While there are many mechanisms in which magnetic fields can be leveraged for mechanical movement, recent advances in stator designs, control algorithms, mover configurations, and modelling approaches have enabled more efficient, scalable, and precise Maglev systems. This review will focus on the macro-scale applications of these technologies, highlighting how specific design choices improve the system's performance and adaptability.

## 2.1 Repulsive Levitation Stages

Repulsive levitation stages benefit significantly from the integration of structural and electrical components within a base layer, leaving the area above unobstructed. This open design allows for additional manufacturing process components to be closely integrated

with the stage, or for the levitation system to be flexibly adapted across a range of industrial applications. This design is particularly advantageous in clean room applications, as it enables the base to be fully isolated from the mover, which interacts with sensitive materials, or fully enclosed to meet stringent sanitation requirements.

One of the earliest exhibits of repulsive magnetic levitation was at the Centennial Exhibition of the Dominion of New Zealand in the 1940s [24]. This event showcased an aluminum pan floating in the air with a strong alternating-current magnetic field—cooking an egg in a pan with the excess heat generated from the eddy currents in the aluminum. The table top concealed an iron core with windings that are powered with alternating current, which produced the toroidal magnetic fields required to generate the levitation force. However, because of the immense power required to maintain such fields, this apparatus had only a publicity appeal. The world's first Maglev stage that provided high precision and the ability to be applied in industrial settings was introduced by Kim et al. in 1998 [9]. The stage consisted of a mover unit made up of four 1D Halbach-type magnet arrays glued to the bottom of a platen, which is able to achieve full 6-DOF movements. The stator—which is fully isolated from below—contained four ironless core square coils with a three-phase winding pattern [25]. This type of design was introduced to improve precision movements in photolithography during the semiconductor manufacturing process, achieving precision movements of up to 5 nm in the $x$ and $y$ axes, 10 nm in the $z$ axis, and 1-$g$ acceleration. This was a significant improvement in the precision control of levitated platforms without the same excessive power consumption previously required.

In the years that followed, a few other groups were able to recreate Maglev stages with similar precision results. Jung et al. constructed a system with a working range of 32 mm in the $xy$ plane and 1.5 mm in the $z$-axis with a repeatability resolution of $\sim 0.5\mu m$ in those same axes [26] while Verma et al. achieved a positional resolution of 5 nm in the translation directions just a couple of years after [27]. Notably, Verma et al. were able to achieve a threefold increase in maximum acceleration (3-$g$) in the horizontal directions when compared to Kim et al. [9]. In 2007, Zhang et al. further improved the precision capability while making the system significantly more compact [28]. The precision achieved was 1.1 nm for x, 0.74 nm for y, and 4.4 nm for z. The range, however, of such a stage is a 2 mm $\times$2 mm $\times$2 mm translational range and a $4^\circ \times 4^\circ \times 4^\circ$ rotational range. Since the modeling techniques employed by this system paired each coil to specific magnets, the range of motion is severely limited. Magnets in the mover cannot move far away from their paired coil, making long-stroke motions impossible or reliant on external robotics or human interactions to compensate.

By considering a 2D Halbach pattern for the magnet array and using long rectangular coils rotated at 45°, Compter was able to construct an Electro-Dynamic Planar Motor

(EPM) that could achieve long stroke motions in the $xy$-plane in 2004 [29]. The main benefits of their design were that the coil winding length could be infinitely extended to meet the requirements of the intended application. They used non-overlapping coils to enable ortho-cyclic winding, increasing the packing density of the coils and improving heat transfer. The mover used a group of three rectangular coils parallel to each other with a three-phase current to control the full 6-DOF. A disadvantage of their design, however, comes from disturbances induced by the cabling that provides power and cooling to the coils on the mover unit. Jansen et al. inverted the setup presented by Compter and analyzed the performance of various coil geometries on the system performance [30]. The mover unit used was constructed as a 2D Halbach magnet array. The stator coils were split into four topologies: the first three topologies consisted of rectangular coils arranged in a herringbone pattern while the fourth topology consisted of a grid of square coils. They found that square coils provided the largest force ripple—caused by cyclical patterns in the magnetic field of the Halbach array—and the herringbone pattern provided consistently lower power dissipation throughout operation. Rectangular coils with a 1:3 width-to-length ratio in their geometry produced a levitation stage with the lowest power dissipation while minimizing the force and torque ripple. When levitating in one spot, the tracking error was comparable to Kim et al. at $0.1\mu m$ and $1\mu rad$ in the translational and rotation axes, respectively—with the added benefit of achieving long stroke motion Kim et al. weren't able to achieve [30, 9]. Rovers et al. conducted another in-depth multiphysics study of the herringbone design in 2013, comparing it to the square coil layout from Jansen et al. and the three-coil group layout from Compter [31]. The static, dynamic, and thermal simulations confirmed the superiority of the herringbone coil pattern in terms of power dissipation and force rippling; however, topologies involving herringbone patterned coils exhibit directional inconsistencies in the levitation performance. In addition, the non-symmetrical nature of the coil design is inherently disadvantageous when a modular conveying system is required [31, 32].

Taking advantage of the simplicity of the square coil topology and inherent symmetry in force and torque production, Trakarnchaiyo et al. presented a levitation stage with rounded square coils [33]. Throughout their work, optimal coil dimensions are found by Fabry factor optimization, and two different coil layouts are compared: a symmetric grid layout and a zig-zag pattern. The zigzag array was found to provide a more uniform magnetic flux density across the working array of the mover. However, noting that since the design of the magnet mover is more significant in levitation efficiency, a straight grid pattern may be preferred if one desires an extendable modular stator in all directions. The optimal coil dimensions presented by Trakarnchaiyo et al. were used for the coils in the stator of the MLPM used in the research presented in the following chapters.

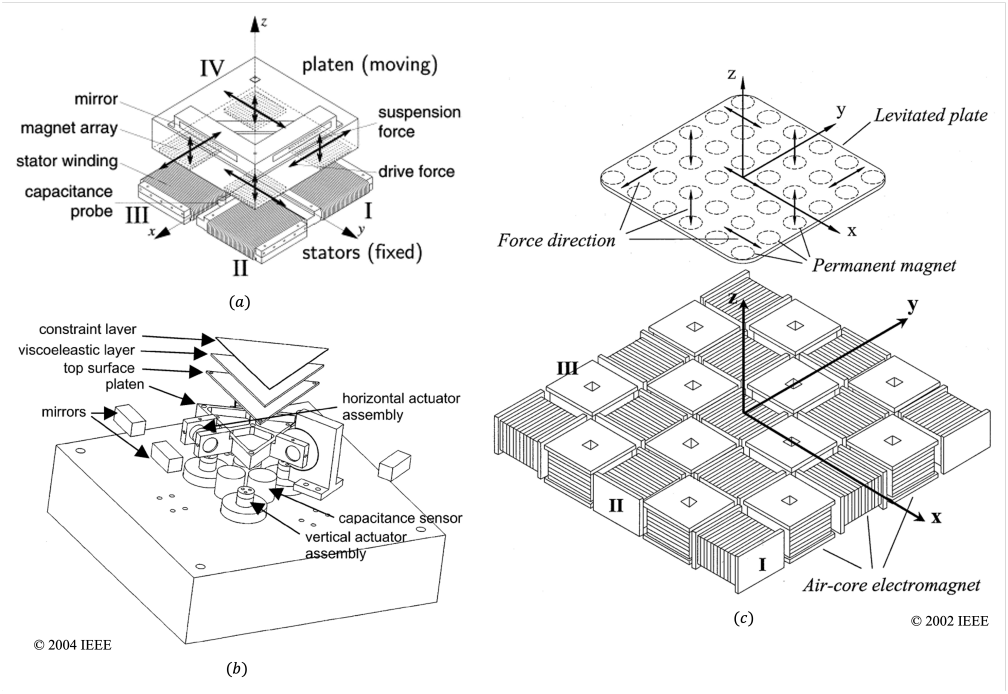



Figure 2.1: Examples of repulsive magnetic levitation stages from key studies: (a) a stage developed for photolithography [9], (b) a triangular levitation stage [27], and (c) a DC driven planar motor [26].

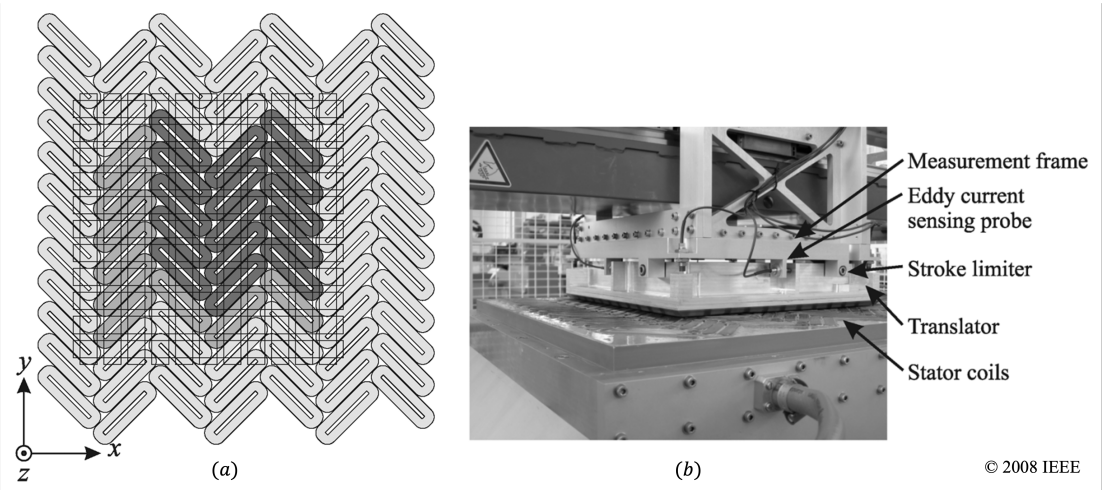



Figure 2.2: Long-stroke repulsive levitation stage utilizing a herringbone stator coil arrangement and a 2D Halbach mover array, adapted from [30].

## 2.2 Attractive/Rotary Levitation Stages

Applications where the geometry of repulsive-type levitation systems inhibits the intended functionality may require a different class of levitation stage. In such cases, attractive levitation stages—which suspend objects from above—can provide the desired friction-free motion in specific operating conditions. Alternatively, some stages may employ a combination of attractive and/or repulsive magnetic interactions to enable more complex motions, such as rotation.

In 2015, Lu et al. proposed a magnetically levitated rotary table with a mover comprised of ninety-four permanent magnets arranged in a circular Halbach pattern. The stator consists of a printed circuit board (PCB) with embedded coils. The coils are separated into four quadrants, where each quadrant can produce a force tangential to the circle of the mover—providing the rotational motions—and a force parallel to the z direction—providing the levitating effect [34]. The sensing equipment is embedded in the center of the rotating assembly. The range of motion achieved by the assembly was $\pm 200 \mu m$ in the $x$- and $y$- axes, $\pm 150 \mu m$ in the $z$-axis, $\pm 0.54^{\circ}$ in rotation about the $x$- and $y$- axes, and unlimited yaw rotations. Xu et al. also built a similar rotary table in 2022 [35]. Their stator consists of physical coil windings forming a toroidal configuration and a mover unit with a curved 1D Halbach array. Xu et al. further implemented multiple control strategies to compensate for external disturbances caused by variations in the external load, such as random air drag considerations. This is important if such a rotary table is to be applied, for example, to a mill machine.

In 2002, Khamesee et al. presented an attractive levitation stage to control a magnetic microrobot with a microscale grip end effector [23]. The microrobot is actuated by a magnetic drive unit consisting of eight electromagnets (in four pairs), two permanent magnets, a pole piece covering the electromagnets, and a return yoke made from soft magnetic iron. The mover consists of a permanent magnet head, a body containing a PCB and batteries, and fingers made from two thin ribbons of a copper alloy. Using this system, the mover can levitate within a volume of $29\text{mm}^3 \times 29\text{mm}^3 \times 26\text{mm}^3$ and can move with a translational precision of 0.05 mm. Since the mover is equipped with an end effector capable of grabbing payloads, performance variations will be prevalent while operating with and without a load mass. They addressed this by implementing a model-reference adaptive control scheme to achieve precise positioning along the $z$-axis during pick-and-place operations. When compared to standard PID control, the rise time was worse for the adaptive control scheme, but overshoot was reduced to almost zero while RMS positional error was kept almost constant throughout payload masses changed. Elbuken et al. also developed a similar attractive levitation stage for micro-manipulation of a small-scale robot embedded with a

permanent magnet [36]. The stator consists of seven electromagnets, a circular pole piece, and a soft iron yoke; the mover is a fully passive structure with two permanent magnets perpendicularly magnetized.

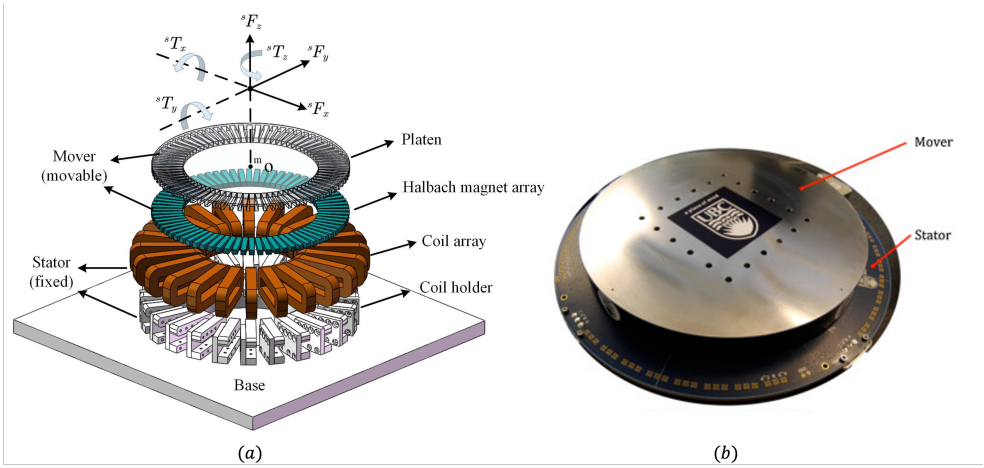



Figure 2.3: Examples of rotary levitation stages in literature: (a) a rotary levitation stage designed by Xu et al. [35], and (b) A rotary levitation stage developed by Lu et al. [34].

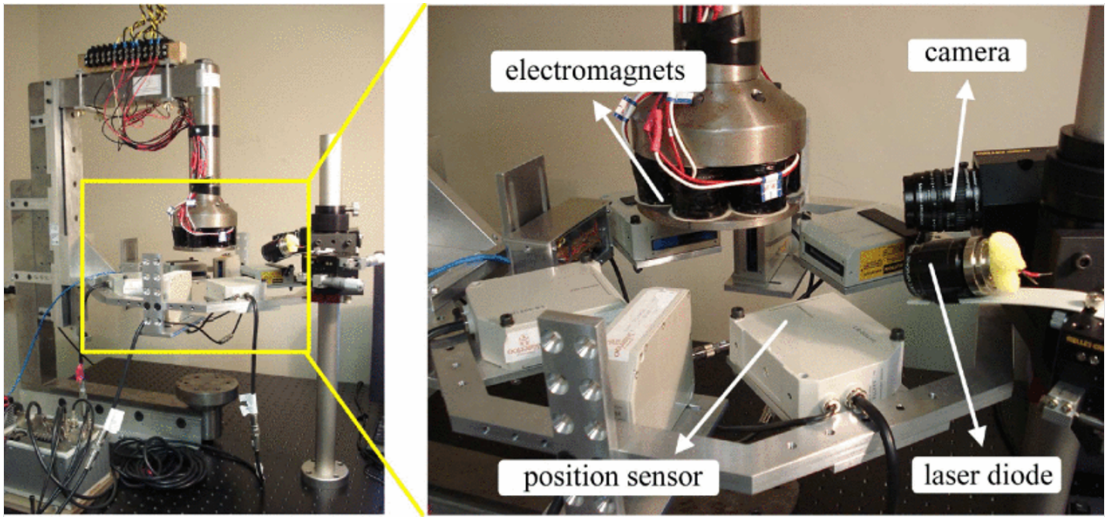



Figure 2.4: Magnetic levitation stage from [36], utilizing attractive forces to achieve stable suspension of a microrobot.

## 2.3 Modeling Methods

To achieve precise control, at each sampling period of the control system, the forces and torques to be applied to the mover must be accurately determined. Numerical algorithms for integrating the three-dimensional forces and torques, as expressed in Equation 3.8, rely on an accurate model of the magnetic field generated by the permanent magnets embedded in the system. Several methods for calculating the magnetic field of permanent magnets have been documented in the literature.

In 1984, Akoun et al. proposed an analytical solution to the "magnetic flux problem" by modeling a permanent magnet as having a *magnetic surface charge* from which the magnetic flux density emanates [37]. Analogous to the surface charge density in electrostatics, this model asserts that there is a fictitious magnetic charge density on the surface of the magnet in the direction of the magnetization. This approach provides relatively straightforward formulae and leverages an intuitive analogy to electrostatics—however, modeling multiple magnets becomes computationally expensive and increasingly time-consuming when incorporating materials with relative permeabilities that significantly deviate from air [38]. To address these challenges, Bancel introduced the concept of "magnetic nodes" which represent each magnet as a collection of nodes located at its corners [39]. This approach offers greater flexibility in the construction of complex magnet shapes and arrays while maintaining manageable computational complexity [40]. For magnet arrays with simple repeatable patterns, such as Halbach arrays, their magnetic fields can be approximated using harmonic functions [41, 42]. This enables real-time calculations, albeit with limitations; these models assume infinite array length and neglect edge effects near the boundaries [43]. Moreover, typical harmonic representations rely on Fourier analysis, whose accuracy depends on the computational ability to account for an infinite series of terms. Establishing a magnetic flux density model enables the computation of the forces and torques resulting from the field's influence.

Researchers from Eindhoven University highlight three primary analytical methods for computing electromagnetic force: the virtual work method, the Maxwell stress method, and the Lorentz force method [45]. The virtual work method finds its prominence in fluid electromagnetic calculations [46, 47] and is commonly used in popular 3D electromechanical simulation software such as ANSYS Maxwell [48, 49]. The Maxwell stress method is typically employed when intricate combinations of magnetic source types are introduced—such as those requiring the accommodation of ferromagnetic materials, like an iron core [46, 50]. In contrast, the Lorentz force method, recognized for its simplicity of implementation, is particularly advantageous for systems involving current-carrying elements. Depending on the composition of the electromagnetic system, each model can be properly

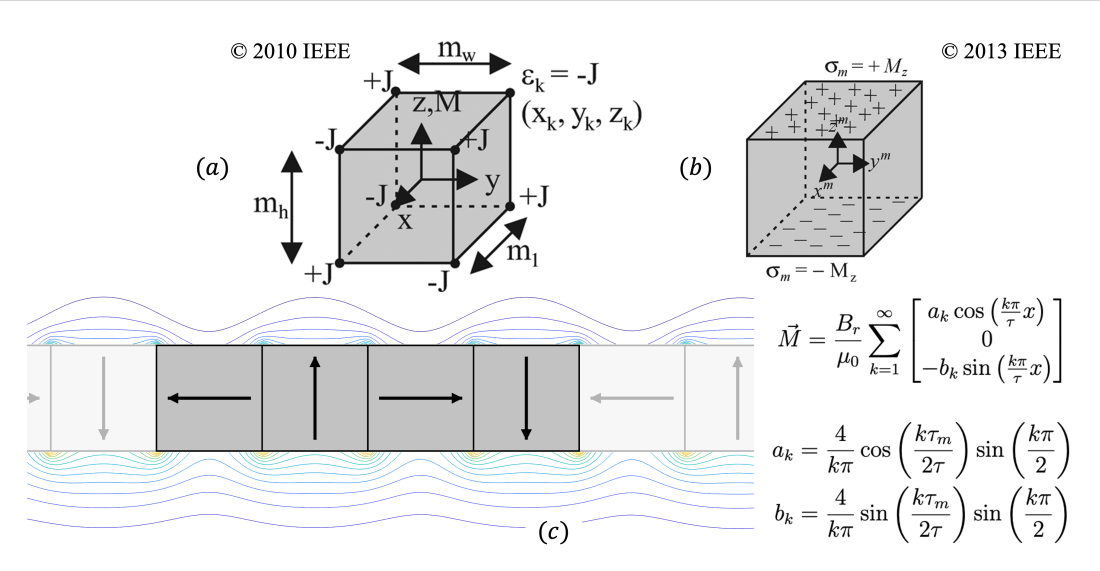



Figure 2.5: Magnetic field model diagrams: (a) illustrates magnetic nodes [44], (b) represents magnetic surface charge [38], and (c) depicts a periodic representation of the magnetic field density of a 1D Halbach. An infinite Fourier series represents the magnetization of the magnet array. The light grey blocks indicate the infinite extension of the 1D Halbach required to define the Fourier function.

employed to ease the calculation complexity and reduce the computation time; however, the fundamental physics that the models obey is the same.

The Lorentz force and subsequent torque can be numerically calculated using the magnetic field models represented in Figure 2.5—however, they are typically time-consuming and require significant computation for real-time operations. A priori calculation of the force and torque values at different locations and orientations of the magnet mover and then storing them in a lookup table can be a viable solution if the necessary computational power is available offline [33, 51, 52]. The advantages of lookup tables are that they can provide extremely fast access times while utilizing more complex models to more accurately calculate the force and torque integrals [53]. However, long-stroke motions, a large number of activated coils, and large DOF requirements drastically increase the storage size of the look-up table if the system's symmetries are not utilized [54, 53]. Peng et al. developed a real-time force and torque model for a 2D Halbach by using a composite numerical integral rule and the Newton-Leibniz formula to complete the integration of the corner of the coils [55]. However, such methods require the use of infinite-horizon harmonic models for the

magnetic flux density, which, as previously mentioned, do not include the edge effect of such arrays. In 2019, Yuan et al. were able to modify the periodicity of such harmonic models to include the edge effect of 2D Halbach arrays [56]. Model improvements become difficult, however, since only the first one or two harmonic components of the Fourier expansion were implemented due to computational limitations. While methods exist to estimate higher-order harmonics, these are typically used for rapid prototyping design constraints and not for real-time control deployment [57]. Xu et al. were able to compute the wrench without requiring infinite terms by incorporating numeric data fitting to account for the edge and corner effects of 2D Halbach arrays. This method improves the accuracy of the modeled wrench when a low number of Fourier terms are used [58]. This model, presented by Xu et al. is used throughout this research and is described in more detail in Section 3.3.3.

## 2.4 Secondary Functions and Control Algorithms

While Maglev systems provide manufacturing processes with the benefits of friction-free movement and up to 6-DOF actuation, some *secondary functions* can be implemented to further benefit its applicators. In assembly processes, Maglev systems that implement automated weighing throughout their frictionless movement can provide seamless transitions between conveying systems, machining processes, and assembly procedures. This would reduce certain high-volume production times and ideally wouldn't require any additional sensors or devices. Currently, the only industrial Maglev planar motor with an integrated weighing function is produced by Planar Motors Inc. [59]. Planar Motor Inc. claim a precision of 0.1g with 0.2g repeatability for their XBot systems. Unfortunately, the proprietary nature of these systems means the method of determination is not reported in the literature.

In a comparable context, magnetic suspension balances (MSBs) have been developed to perform weight measurements of objects when stationary. In 2017, Benck et al. proposed a mass calibration system that compares the masses of objects in a vacuum with those suspended in air, using a magnetically levitated weighing chamber [60]. A typical MSB consists of a permanent magnet and an electromagnet placed on opposite sides of a wall that separates the measurement area from the observation area. The permanent magnet is attached to the object to be weighed, while the electromagnet's current is actively adjusted to achieve stable suspension of the object–permanent magnet assembly. The object's weight is then inferred from the current required to maintain suspension [61]. This principle was first demonstrated in 1947 by Clark [62]. They achieved a measurement

sensitivity of 50 milligrams per milliampere[1]. More recent improvements to precision involve using the magnetic suspension solely for levitation, while a conventional analytical balance, mechanically linked to the magnets, provides the weight measurements. In such configurations, the accuracy of the mass reading is entirely determined by the precision of the chosen analytical balance [61].

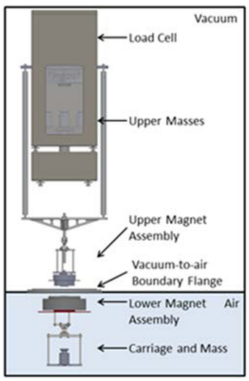



Figure 2.6: Magnetic suspension mass comparison device developed by [60].

Further progress to such secondary functions involves improvements in controller designs. Hu et al. proposed a learning adaptive robust controller for a Maglev positioner [63]. The adaptive robust control compensates for the parametric variation—such as mass variations—while the iterative learning control (ILC) corrects the unknown disturbances. The ILC control improved the performance on repeatable trajectories but has difficulty generalizing to new paths, which is important for flexible manufacturing plants. Such investigations focus more on using parameter estimation and adaptive control to improve control performance. There is no work directly related to reporting payload characteristics in addition to guaranteeing the control performance in the literature.

Standard controllers for magnetically actuated and levitated systems typically include Proportional–Integral–Derivative (PID) or lead-lag controllers. These controllers are implemented because they are easy to use and intuitive to define. Trakarnchaiyo et al. used five independent PID controllers to control the 5-DOF of their single disk mover, while Xu et al. used six independent PID controllers to control the 6-DOF of their Halbach magnet mover [54, 64]. While these controllers are easy to implement, low manufacturing tolerances and system model errors increase the computation cost of some of the PID terms. Sinha et al. developed a model-reference adaptive control with stable maximum

[1]Since the output was displayed on an ammeter, each milliampere change corresponded to a mass change of 50 milligrams




(*a*) (*b*)

Figure 2.7: Examples of automatic weighing functions for industrial applications (by Planar Motors Inc.): (a) demonstrates automated weighing for general conveying systems; while (b) illustrates its use in hygienic, food-grade environments. Images from [59].

descent [65]. The error between the actual and reference model is reduced through constraints and adaptive proportional–integral–derivative parameters are derived. In 2020, an observer-based adaptive controller was proposed on a 1D Maglev system [66]. A non-linear observer was implemented to find the velocity. The system could run without information about the system because the system could rapidly compute all the parametric variations. Adaptive sliding mode controls are also investigated on Maglev planar motors and rotary motors to compensate for the system nonlinearities [67, 68]. While, there exist previous works regarding implementing adaptive control over Maglev planar motors, additional application-specific implementation is still required.

Additional secondary functions Maglev systems could implement include 'magnetic locking' of the movers on the stator by reversing coil currents. This can ensure the non-slippage of platforms during assembly tasks [64]. They also allow quicker on and off switching when compared to conventional mechanical locking platforms. However, reports implementing this task have not been published in the literature or highlighted in industry. Implementing these secondary functions into the control systems of Maglev platforms would allow for the entire system to be easy to use, as the user would not have to worry about the distribution of weights in the packages they place. As well, since the implementation is strictly software (i.e., strictly within the control structures), no extra hardware would be required to conduct such seamless operations. As a result, large-scale planar Maglev conveying systems that implement automated weighing control and other secondary functions are highly desired within the flexible manufacturing field, and such, are implemented throughout this work.

# Chapter 3

# Related Background Theory

This chapter establishes the theoretical framework necessary to understand magnetically levitated stages and their operation. It begins by defining key terminology related to magnetics, followed by an introduction to the essential parameters that characterize the system. Subsequently, the chapter introduces the principles of magnetic field modeling and formulates the electromagnetic forces involved. The discussion concludes with a detailed presentation of the adaptive control framework utilized, and necessary stability arguments are presented.

## 3.1 Magnet Properties and Halbach Arrays

Magnets are very useful in everyday life because of the *action-at-a-distance*[1] properties they exhibit. While there are a whole host of materials that can be constructed to create a magnet-like structure, common minerals that are used to create magnets typically consist of some alloy of neodymium, iron, and boron (Nd-Fe-B). These rare earth magnets produce significantly higher energy products $(BH)_{max}$ and can be used to provide extremely strong forces [70]. They are typically categorized by grade, ranging from about N35 to N52, where a higher number corresponds to a greater maximum energy product $(BH)_{max}$. In practical terms, higher-grade magnets produce stronger magnetic fields and exhibit a greater maximum pulling force [71]. While not an exhaustive list, Table 3.1 defines some of the common properties used to describe magnets and magnetic materials.

[1]The existence of physical media as a mechanism to transmit mechanical forces generated by magnetic interactions has been debated in physics and philosophy since the early 18th century. Hesse provides a narrative review of the *action-at-a-distance* discussions led by prominent physicists of the time [69].

Table 3.1: Common terminology related to magnetic materials.

| Property | Symbol | Description |
|---|---|---|
| Magnetization | $\mathbf{M}$ | The magnetization of a material is the magnetic dipole moment per unit volume within a material. This may be temporary or permanently induced by external magnetic fields, depending on the material properties. [Units: A/m] |
| Remanence | $B_r$ | A measure of the magnetization left behind in a ferromagnetic material after removing an external magnetic field. While it can be expressed as a vector, the magnitude of the vector is typically stated by manufacturers for simple comparisons. [Units: T] |
| Magnetic Flux Density | $\mathbf{B}$ | A magnetic field, or magnetic flux density, is a vector field generated by electric currents and magnetic materials, guiding the motion of charged particles and interacting with other magnetic objects. [Units: T] |
| Magnetic Permeability | $\mu$ | A measure of the relative change in the magnetic field inside a material in the presence of an external magnetizing field. The relative permeability ($\mu_r$) is the ratio of the magnetic permeability of a material to the permeability of free space, $\mu_0$. [Units: $N/A^2$] |
| Coercivity | $H_c$ | A metric characterizing a ferromagnetic material's ability to retain its magnetization in the presence of an external magnetic field. [Units: A/m] |

Halbach arrays are collections of permanent magnets in which the magnetization of each magnet follows a rotating pattern. They were independently developed by Klaus Halbach [72] in the 1980s and John C. Mallinson [73] in the 1970s. These magnetic arrays are of interest because they exhibit a sort of "one-sided flux". Denoted the "strong side", the flux is concentrated on this one side while the resulting magnetic flux density on the opposing side is fairly weak (denoted the "weak side"). This is particularly useful in directing the energy associated with the magnetic field and not losing flux to undesirable locations. A traditional 1D Halbach array consists of adjacent magnets with magnetization vectors rotated 90 degrees to each other, as shown in Figure 3.1—more acute angles can be chosen, but more magnets are required to complete the magnetization pattern to achieve the desired effect. Two-dimensional extensions of the linear Halbach array can be constructed to create

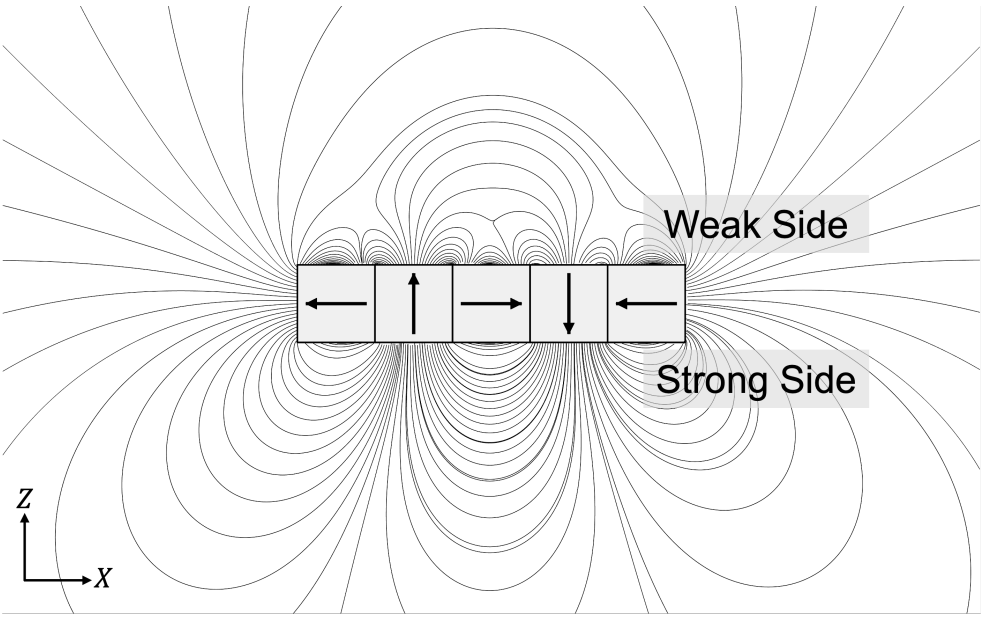



Figure 3.1: Flux lines and magnetization vectors in a 1D linear Halbach array. Areas of denser flux lines correlate with increased **B** field strength.

a plane of magnetic flux with one side stronger than the other (shown in Figure 3.2). The existing applications that employ Halbach magnet arrays range from refrigerator magnets to the generation of synchrotron light in free electron lasers [74, 75]. The modeling of magnetic fields and resultant forces produced by such magnet arrays is explored throughout Section 3.3.

There are specific parameters associated with the construction of a Halbach permanent magnet array. The pole pitch ($\tau$) is the center-to-center distance between magnets whose magnetization vector is oriented parallel (or anti-parallel) to the z-axis. If the z-aligned magnets are square, then the z-magnet width ($\tau_m$) and height of all the magnets ($h$) are all that is needed to specify the dimensions of the entire array. The number of poles in a Halbach array is the number of z-aligned permanent magnets. Another important parameter is the rotation angle, which describes the change in angle of the magnetization vector between adjacent magnets. In the Halbach arrays used throughout this work, the rotation angle is 90°. Figure 3.2 illustrates the arrangement and definitions of these parameters for a 2D Halbach array.

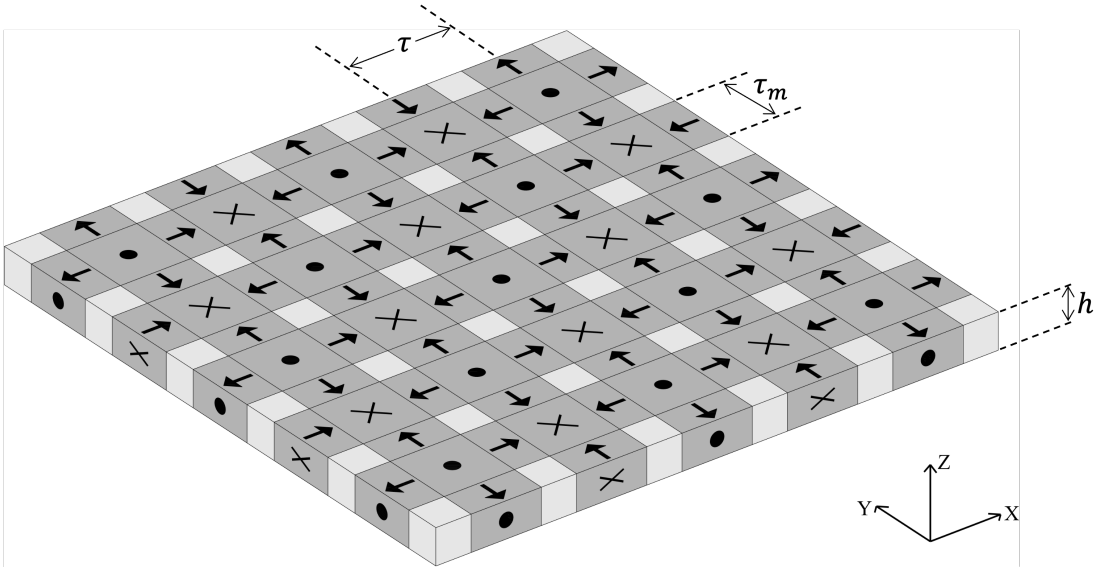



Figure 3.2: Magnetization vectors and relevant parameters depicted for a 2D planar Halbach array. The configuration shown produces a weaker magnetic flux density in the region above the array (positive z) and a stronger magnetic flux density in the region below (negative z).

## 3.2 Coordinate Systems and Transformations

Accurate computation of force and torque requires clearly defined coordinate systems to describe the position and orientation of the magnetically levitated planar motor components. Three distinct coordinate systems are established for this purpose: the coil-fixed frame, the mover-fixed frame, and a global reference frame.

$\{g\}$ Global coordinate system – The origin is defined at the center of the top surface of the coil array. It should be noted that the protruding length of the bobbin each coil is wound around protrudes by 1.5 mm above the coil's top surface. The motion capture measurement system is aligned with this global coordinate system, while all other frames are defined relative to this fixed global coordinate frame.

$\{c\}$ Coil coordinate system – Each electromagnetic coil has an associated coordinate frame with an origin at the center of the coil's top surface. The x and y axes are parallel with the corresponding global coordinate frame axes. The position of the $i$th coil center in global coordinates is denoted by ${}_g\mathbf{c}_i = {}_g [c_{x,i}, c_{y,i}, c_{z,i}]^T$.

$\{m\}$ Mover coordinate system – The origin is located at the bottom center of the mover's magnet array and parallel with its edges. This coordinate system, fixed to the mover, moves and rotates with it. The mover's center expressed in global coordinates is ${}_g\mathbf{m} =_g [m_x, m_y, m_z]^T$.

The mover's orientation is expressed in terms of XYZ Euler angles relative to the global frame: roll (rotation about $X_g$), pitch (rotation about $Y_g$), and yaw (rotation about $Z_g$) angles are denoted as $\alpha$, $\beta$, $\gamma$ respectively. Using these, the orientation of the mover frame, $\{m\}$, expressed in the global frame, $\{g\}$, can be determined using the following rotation matrices

$$ {}_g\mathbf{R}_m = \mathbf{R}_{xyz} = \mathbf{R}_x\mathbf{R}_y\mathbf{R}_z \tag{3.1} $$

$$ \mathbf{R}_x = \begin{bmatrix} 1 & 0 & 0 \\ 0 & \cos(\alpha) & -\sin(\alpha) \\ 0 & \sin(\alpha) & \cos(\alpha) \end{bmatrix}, \quad \mathbf{R}_y = \begin{bmatrix} \cos(\beta) & 0 & \sin(\beta) \\ 0 & 1 & 0 \\ -\sin(\beta) & 0 & \cos(\beta) \end{bmatrix} \tag{3.2} $$

$$ \mathbf{R}_z = \begin{bmatrix} \cos(\gamma) & -\sin(\gamma) & 0 \\ \sin(\gamma) & \cos(\gamma) & 0 \\ 0 & 0 & 1 \end{bmatrix} $$

where the left subscript of Equation 3.1 denotes the previous frame and the right subscript denotes the new frame. By combining the rotation matrices with the translational position of the mover unit, any vector in the mover frame can be transformed into the global frame using the homogeneous transformation matrix:

$$ {}_g\mathbf{T}_m = \left[\begin{array}{c|c} {}_g\mathbf{R}_m & {}_g\mathbf{m} \\ \hline \mathbf{0} & \mathbf{I} \end{array}\right] \tag{3.3} $$

where ${}_g\mathbf{m}$ is the location of the mover center in global coordinates, as shown in Figures 3.3 and 3.4. The inverse of this transformation matrix allows for transforming vectors from the global frame back to the mover frame:

$$ {}_m\mathbf{T}_g = ({}_g\mathbf{T}_m)^{-1} \tag{3.4} $$

This formulation is computationally efficient and simplifies notation by canceling common subscripts. For example, the position of a coil center transformed from the global frame (${}_g\mathbf{c}$) to the mover frame (${}_m\mathbf{c}$) is given by:

$$ {}_m\mathbf{c} = [{}_m\mathbf{T}_g]{}_g\mathbf{c} = [{}_m\mathbf{T}_{\not g}]{}_{\not g}\mathbf{c} \tag{3.5} $$

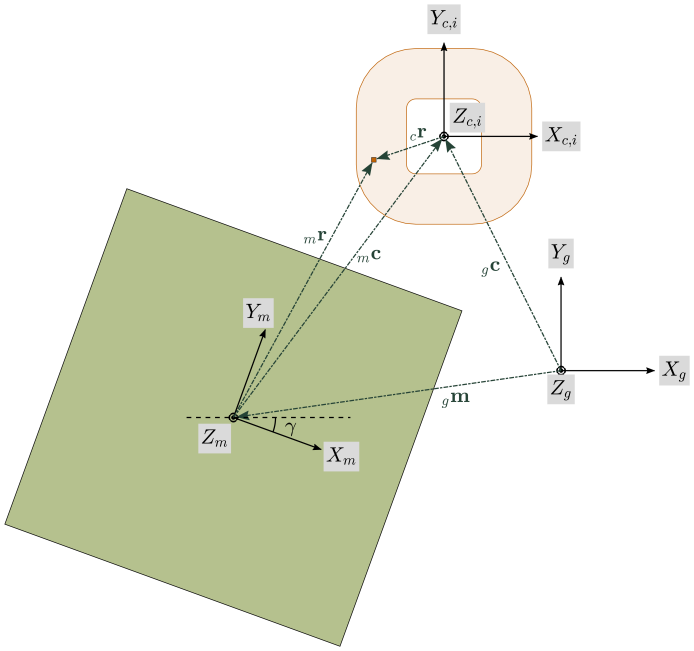



Figure 3.3: Top-down view schematic illustrating the coordinate frames used in the Maglev system. The green rectangular area represents the mover unit used in this research, with its coordinate frame positioned at the bottom center. Positive rotations are defined as counterclockwise when viewed from above.

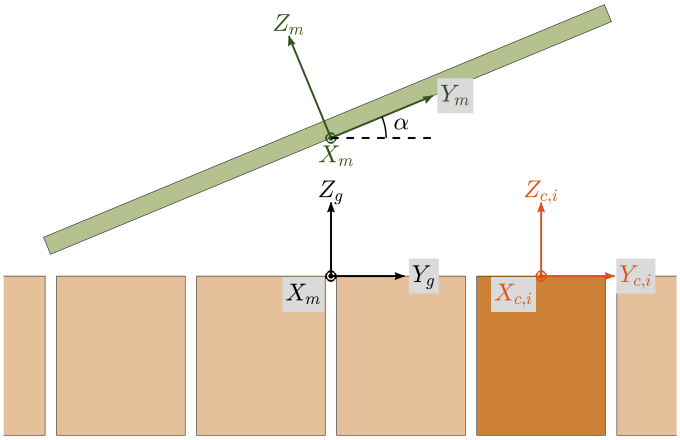



Figure 3.4: Side view schematic illustrating the coordinate frames used in the Maglev system.

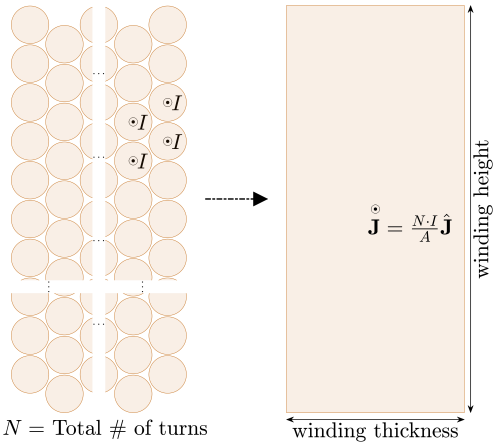



Figure 3.5: Illustration of the coil conductor model.

## 3.3 Magnetic Modeling

### 3.3.1 Lorentz Force and Torque

Magnetic levitation systems involve the interaction between electromagnetic coils and permanent magnets—the current in the coils interacts with the magnetic field produced by the permanent magnets of the mover. The forces that fundamentally describe interactions between moving charges and magnetic fields can be described through the Lorentz Force law. For a given point charge $q$, the Lorentz force experienced by that charge is given by

$$\mathbf{F} = q(\mathbf{E} + \mathbf{v} \times \mathbf{B}) \tag{3.6}$$

Assuming that an arbitrary charge distribution can be modeled as a collection of point charges, the force $dF$ on an infinitesimal part of the charge distribution $dq$ is given by the Lorentz Force law. Given that the charge density $\rho = \frac{dq}{dV}$ and that no electric fields are present in the magnetic levitation system (on the scale that is non-negligible), the force density $\boldsymbol{f}$ is

$$\boldsymbol{f} = \frac{d\mathbf{F}}{dV} = \frac{dq}{dV}(\cancel{\mathbf{E}} + \mathbf{v} \times \mathbf{B}) = \rho\mathbf{v} \times \mathbf{B} \tag{3.7}$$

Recognizing that $\rho\mathbf{v}$ describes the current density $\mathbf{J}$ of an arbitrary "moving" charge distribution, equation 3.7 can be integrated to determine the force imparted on any charge distribution, namely a coil in the stator. This is the force imparted by the permanent magnet (mediated through its magnetic field) to the coil; through Newton's second law, the force on the mover unit is equal and opposite to the force on the coil.

$$\mathbf{F}_{\text{coil}} = \int_{V_{\text{coil}}} \boldsymbol{J} \times \boldsymbol{B}\, \mathrm{d}V_{\text{coil}} \qquad\qquad \mathbf{F}_{\text{mover}} = -\mathbf{F}_{\text{coil}}$$

The torque experienced on the mover is given by the cross-product of the force on the mover and the torque arm, $\mathbf{r}$. Therefore, the force and torque experienced by the mover are

$$\begin{aligned} \mathbf{F}_{\text{mover}} &= -\int_{V_{\text{coil}}} \mathbf{J} \times \mathbf{B} \mathrm{d}V_{\text{coil}}, \\ \mathbf{T}_{\text{mover}} &= -\int_{V_{\text{coil}}} \boldsymbol{r} \times (\mathbf{J} \times \mathbf{B}) \mathrm{d}V_{\text{coil}}. \end{aligned} \tag{3.8}$$

Since no additional constraints exist on the system, these forces can be applied to actuate movers in free space. Two key elements are required to calculate these forces in practice. First, an expression is needed for the charge density ($\mathbf{J}$) in an infinitesimal segment of the coil. Calculating the current density of a coil involves dividing the total current by the

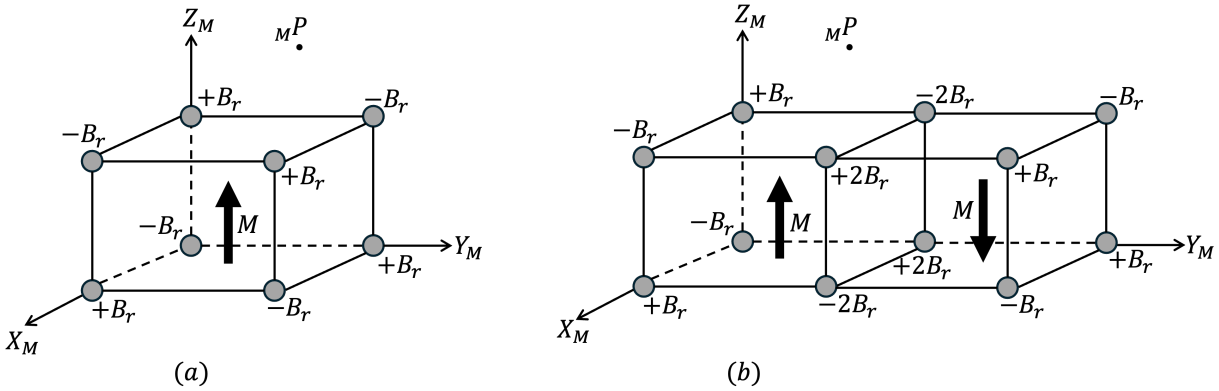



Figure 3.6: Magnetic node distributions. (a) Magnetic node representation of a single permanent magnet with vertical magnetization $M$. (b) Multi-magnet node configuration with alternating magnetization orientations. Here, $B_r$ denotes the remanent magnetization strength of the permanent magnet and ${}_mP$ is the point of interest.

perpendicular cross-sectional area of the coil. Since the cross-sectional area remains constant throughout the coil, the magnitude of the current density is uniform across all points in the coil. This simplification, which converts the winding model to a solid conductor model, is beneficial because it reduces the number of points required for numeric approximations of the magnetic field and forces. By treating the coil as a continuous conductor, computational resources are conserved, allowing for more efficient and accurate magnetic field interaction calculations. The coil conductor model is shown in Figure 3.5.

The second element required is a method to calculate the magnetic field ($\mathbf{B}$) produced by a complex permanent magnet array, taking into account any orientation and any point in space. Many models were introduced in section 2.3, however, this research continues with the Magnetic Nodes method.

### 3.3.2 Magnetic Nodes

The magnetic field external to an array of magnets can be determined using the magnetic nodes method, introduced by F. Bancel in 1999 [39]. This method models the external magnetic field of a permanent magnet as though it originates from the superposition of "magnetic charges" located at the corners of the magnet[2]. For a cuboidal magnet, these

[2]It is important to note that this is strictly a mathematical equivalence since no physical magnetic nodes have been shown to exist

magnetic charges, or "nodes," are positioned at each of the eight corners of the cube, with their signs assigned according to the conventions outlined by Bancel [39] and illustrated in Figure 3.6. This model relies on the assumption that the magnets are ideal, with a fixed and uniform magnetization, and that no nearby material influences or distorts the magnetic field. Based on the node arrangement in Figure 3.6, the magnetic flux density contribution from each node $k$ at a point $P(x, y, z)$ can be calculated by the following equations:

$$\begin{aligned} B_{xk}(x,y,z) &= \frac{\varepsilon_k}{4\pi} \ln\left(-y_r + \sqrt{x_r^2 + y_r^2 + z_r^2}\right) \\ B_{yk}(x,y,z) &= \frac{\varepsilon_k}{4\pi} \ln\left(-x_r + \sqrt{x_r^2 + y_r^2 + z_r^2}\right) \\ B_{zk}(x,y,z) &= \frac{\varepsilon_k}{4\pi} \arctan\left(\frac{x_r y_r}{z_r \sqrt{x_r^2 + y_r^2 + z_r^2}}\right) \end{aligned} \tag{3.9}$$

In this context, the parameters $x_r$, $y_r$, and $z_r$ represent the relative distances $x - x_k$, $y - y_k$, and $z - z_k$ from the point of interest to each node, respectively. The charge $\varepsilon_k$ at each node assumes values of $+B_r$ or $-B_r$, following the conventions illustrated in Figure 3.6. If the magnetization is reversed, the signs of $\varepsilon_k$ are also inverted accordingly.

To extend this model to configurations involving multiple magnets, the contributions of $\varepsilon_k$ from coincident nodes are superimposed. This summation comprehensively incorporates all nodes present in the system. It is critical to use magnets whose strength is below the coercivity threshold that would induce demagnetization between magnets to preserve the validity of this model's assumptions. It is important to note that the relative distances defined in Equations 3.9 are defined in a coordinate system relative to the permanent magnet array. In the Maglev system, this is the mover's coordinate frame $m$. Since the number of magnetic nodes in a system increases approximately linearly with the number of magnets in the array[3] the magnetic flux density at a point of interest P from the total number of magnetic nodes N in the magnetic array, expressed in the mover frame, is

$${}_m\mathbf{B} = \sum_{k=1}^{N} \begin{bmatrix} B_{xk} & B_{yk} & B_{zk} \end{bmatrix}^T \tag{3.10}$$

For completeness, it should be noted that the magnetic node formulation presented in [39] is strictly defined for permanent magnets with vertically oriented magnetization

[3]This is approximate because while every magnet added to the system does increase the number of nodes by 8 (if cuboidal magnets are only involved) if any side of the magnet is coincident with each other, the overlapping sides share 4 common nodes. Assuming that the thickness of each magnet is equal, $N = 8 \cdot (\#$ of permanent magnets$) - 4 \cdot (\#$of coincident sides).

vectors. To extend this model to magnets with horizontally aligned magnetization vectors, the position of interest, $P$, should be transformed from the mover frame to a temporary frame in which the z-axis is either parallel or anti-parallel to the magnetization vector. In this temporary frame, assign the magnetic node signs according to the conventions shown in Figure 3.6. Using Equations 3.9, calculate the magnetic flux density in this rotated frame. Finally, rotate the computed result back to the original mover frame before summing it with the magnetic field contributions from other "properly" aligned magnets. Figures 3.7 and 3.8 show the assigned magnetic node sign for a horizontally magnetized permanent magnet.

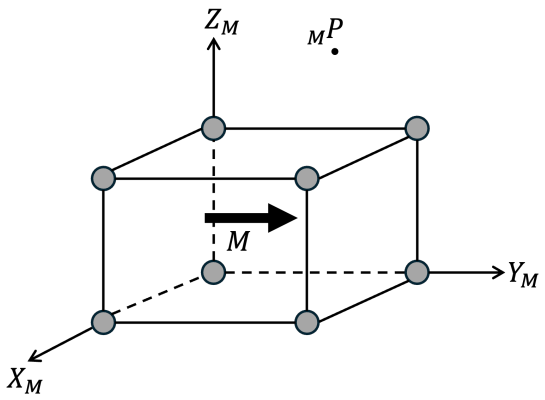



Figure 3.7: Permanent magnet with a horizontally aligned magnetization vector

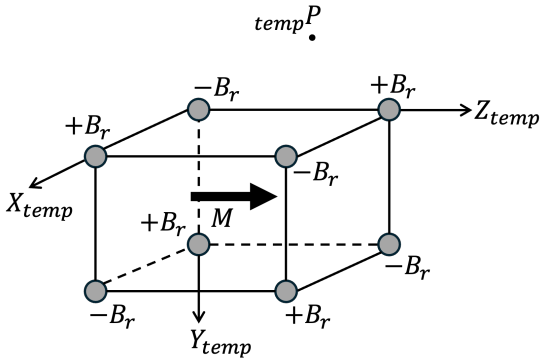



Figure 3.8: Magnetic node representation of a permanent magnet with a horizontally aligned magnetization vector with magnetic nodes assigned based on alignment relative to the temporarily transformed frame.

The force and torque exerted on the mover by each coil, as described in Equation 3.8, can be calculated by applying the magnetic node method alongside numerical integration techniques. While this approach can be used to generate a look-up table suitable for control, it is too slow for the 1000 Hz real-time control requirements of the present system. To address this constraint, Xu et al. developed a data-driven method capable of achieving the necessary processing speed for real-time control [58].

### 3.3.3 Real Time Method

A novel real-time method for calculating the 3D forces and torques on a 2D Halbach array above a coil is presented by Xu et al. [58]. This data-driven model utilizes modified Fourier series' to represent the force and torque based on the position of the coil with respect to specific zones under a 2D Halbach array. The area beneath the Halbach array is split into central, edge, and corner regions. The central region is defined as the area where the numerically calculated magnetic flux density closely aligns with the unmodified harmonic expression of the magnetic flux density, while the edge and corner regions encompass the areas where the magnetic flux density deviates significantly from this simplified representation. Further details on the modeling and specific dimensions of these zones are located in section 4.2.1.

The forces and torques on the mover when a coil is fully within the central region underneath a 2D Halbach can be modeled using a harmonic series [42]. Using a first-order harmonic function, the force on the mover from a coil in the central region is

$$ {}_m\mathbf{F}_{\text{center}}\ ({}_mc_x, {}_m c_y, {}_m c_z) = I \begin{bmatrix} K_x \cos(\eta_x) \sin(\eta_y) \\ K_y \sin(\eta_x) \cos(\eta_y) \\ K_z \sin(\eta_x) \sin(\eta_y) \end{bmatrix} \tag{3.11} $$

where $\eta_x = \pi_m c_x/\tau$ and $\eta_y = \pi_m c_y/\tau$. $I$ is the current running through the coil. $K_x, K_y$, and $K_z$ are exponential decay functions related to the air gap between the mover and coil with units of N/A. Equations for $K_x, K_y$, and $K_z$ are given by

$$ \begin{aligned} K_x &= \alpha_x e^{\beta_k |{}_m c_z|} \\ K_y &= \alpha_y e^{\beta_k |{}_m c_z|} \\ K_z &= \alpha_z e^{\beta_k |{}_m c_z|} \end{aligned} \tag{3.12} $$

The constants $\alpha_x$, $\alpha_y$, $\alpha_z$, and $\beta_k$ found from data fitting with numeric solutions using the magnetic node method and are dependent on the levitation height $|{}_m c_z|$. When a coil enters the edge region, the force distribution along one direction follows the same sinusoidal pattern as the central region, while the force distribution along the perpendicular axis follows a non-linear wave pattern that depends on the mover's height above the coil. The axis in which the force distribution follows this pattern is different for each edge region; however, due to the symmetry of the system, [58] found that only three non-linear functions are needed. These functions, $f_1$, $f_2$, $f_3$, are found by fitting a modified third-order Fourier series with numeric solutions calculated using the magnetic node model. The force

equations in the four edge regions can be calculated through

$$ {}_m\mathbf{F}_{\text{edge 1}}\left({}_m\boldsymbol{c}\right) = I \begin{bmatrix} K_x \cos\left(\eta_x\right) f_1\left({}_mc_y,\, {}_mc_z\right) \\ K_y \sin\left(\eta_x\right) f_2\left({}_mc_y,\, {}_mc_z\right) \\ K_z \sin\left(\eta_x\right) f_3\left({}_mc_y,\, {}_mc_z\right) \end{bmatrix} \tag{3.13a} $$

$$ {}_m\mathbf{F}_{\text{edge 2}}\left({}_m\boldsymbol{c}\right) = I \begin{bmatrix} K_x f_2\left(-{}_mc_x,\, {}_mc_z\right) \sin\left(\eta_y\right) \\ -K_y f_1\left(-{}_mc_x,\, {}_mc_z\right) \cos\left(\eta_y\right) \\ -K_z f_3\left(-{}_mc_x,\, {}_mc_z\right) \sin\left(\eta_y\right) \end{bmatrix} \tag{3.13b} $$

$$ {}_m\mathbf{F}_{\text{edge 3}}\left({}_m\boldsymbol{c}\right) = I \begin{bmatrix} K_x f_2\left({}_mc_x,\, {}_mc_z\right) \sin\left(\eta_y\right) \\ K_y f_1\left({}_mc_x,\, {}_mc_z\right) \cos\left(\eta_y\right) \\ K_z f_3\left({}_mc_x,\, {}_mc_z\right) \sin\left(\eta_y\right) \end{bmatrix} \tag{3.13c} $$

$$ {}_m\mathbf{F}_{\text{edge 4}}\left({}_m\boldsymbol{c}\right) = I \begin{bmatrix} -K_x \cos\left(\eta_x\right) f_1\left(-{}_mc_y,\, {}_mc_z\right) \\ K_y \sin\left(\eta_x\right) f_2\left(-{}_mc_y,\, {}_mc_z\right) \\ -K_z \sin\left(\eta_x\right) f_3\left(-{}_mc_y,\, {}_mc_z\right) \end{bmatrix}. \tag{3.13d} $$

When a coil enters the corner regions, the force distribution in both the X and Y directions follows the same nonlinear wave functions from the edge region. Therefore, to model all the forces, only three nonlinear functions need to be determined from data fitting of numeric solutions. The force equations under the corner regions are as follows.

$$ {}_m\mathbf{F}_{\text{corner1}}\left({}_m\boldsymbol{c}\right) = I \begin{bmatrix} K_x f_2\left(-{}_mc_x,\, {}_mc_z\right) f_1\left({}_mc_y,\, {}_mc_z\right) \\ -K_y f_1\left(-{}_mc_x,\, {}_mc_z\right) f_2\left({}_mc_y,\, {}_mc_z\right) \\ -K_z f_3\left(-{}_mc_x,\, {}_mc_z\right) f_3\left({}_mc_y,\, {}_mc_z\right) \end{bmatrix} \tag{3.14a} $$

$$ {}_m\mathbf{F}_{\text{corner2}}\left({}_m\boldsymbol{c}\right) = I \begin{bmatrix} K_x f_2\left({}_mc_x,\, {}_mc_z\right) f_1\left({}_mc_y,\, {}_mc_z\right) \\ K_y f_1\left({}_mc_x,\, {}_mc_z\right) f_2\left({}_mc_y,\, {}_mc_z\right) \\ K_z f_3\left({}_mc_x,\, {}_mc_z\right) f_3\left({}_mc_y,\, {}_mc_z\right) \end{bmatrix} \tag{3.14b} $$

$$ {}_m\mathbf{F}_{\text{corner3}}\left({}_m\boldsymbol{c}\right) = I \begin{bmatrix} -K_x f_2\left(-{}_mc_x,\, {}_mc_z\right) f_1\left(-{}_mc_y,\, {}_mc_z\right) \\ -K_y f_1\left(-{}_mc_x,\, {}_mc_z\right) f_2\left(-{}_mc_y,\, {}_mc_z\right) \\ K_z f_3\left(-{}_mc_x,\, {}_mc_z\right) f_3\left(-{}_mc_y,\, {}_mc_z\right) \end{bmatrix} \tag{3.14c} $$

$$ {}_m\mathbf{F}_{\text{corner4}}\left({}_m\boldsymbol{c}\right) = I \begin{bmatrix} -K_x f_2\left({}_mc_x,\, {}_mc_z\right) f_1\left(-{}_mc_y,\, {}_mc_z\right) \\ K_y f_1\left({}_mc_x,\, {}_mc_z\right) f_2\left(-{}_mc_y,\, {}_mc_z\right) \\ -K_z f_3\left({}_mc_x,\, {}_mc_z\right) f_3\left(-{}_mc_y,\, {}_mc_z\right) \end{bmatrix}. \tag{3.14d} $$

The torque equations are found through a cross-product with the force on the mover. However, since there is no physical connection from the coil to the mover unit, Xu et al.

introduce the effective torque arm on the mover as such

$$ {}_m\mathbf{T}_{\text{center}} = \begin{bmatrix} r_{y1}^{\text{eff}} F_z - r_{z1}^{\text{eff}} F_y \\ -r_{x1}^{\text{eff}} F_z + r_{z2}^{\text{eff}} F_x \\ r_{x2}^{\text{eff}} F_y - r_{y2}^{\text{eff}} F_x \end{bmatrix} \tag{3.15} $$

where $r_{x1}^{\text{eff}}$ , $r_{x2}^{\text{eff}}$ , $r_{y1}^{\text{eff}}$ , $r_{y2}^{\text{eff}}$ , $r_{z1}^{\text{eff}}$ , and $r_{z2}^{\text{eff}}$ are the effective torque arms. In the central region, functions describing the effective torque arms are fit using either a linear function or inclined tangent planes.

In the edge and corner regions, similar to before, third-order Fourier series' are fitted with numeric data solutions. Because of the symmetry of a Halbach array, only three functions $t_1, t_2$, and $t_3$ are needed to model all the torque components. The torque in the edge regions is given by

$$ \begin{aligned} {}_m\mathbf{T}_{\text{edge 1}}\left({}_m\boldsymbol{c}\right) &= \begin{bmatrix} I\sin\left(\eta_x\right) t_1\left({}_mc_y,\, {}_mc_z\right) + I\sin\left(\eta_x\right) t_2\left({}_mc_y,\, {}_mc_z\right) \\ -r_{x1}^{\text{eff}} F_z + I\cos\left(\eta_x\right) t_3\left({}_mc_y,\, {}_mc_z\right) \\ r_{x2}^{\text{eff}} F_y + I\cos\left(\eta_x\right) t_4\left({}_mc_y,\, {}_mc_z\right) \end{bmatrix} \\ {}_m\mathbf{T}_{\text{edge 2}}\left({}_m\boldsymbol{c}\right) &= \begin{bmatrix} r_{y1}^{\text{eff}} F_z + It_3\left(-{}_mc_x,\, {}_mc_z\right)\cos\left(\eta_y\right) \\ -It_1\left(-{}_mc_x,\, {}_mc_z\right)\sin\left(\eta_y\right) - It_2\left(-{}_mc_x,\, {}_mc_z\right)\sin\left(\eta_y\right) \\ -It_4\left(-{}_mc_x,\, {}_mc_z\right)\cos\left(\eta_y\right) - r_{y2}^{\text{eff}} F_x \end{bmatrix} \\ {}_m\mathbf{T}_{\text{edge 3}}\left({}_m\boldsymbol{c}\right) &= \begin{bmatrix} r_{y1}^{\text{eff}} F_z - It_3\left({}_mc_x,\, {}_mc_z\right)\cos\left(\eta_y\right) \\ -It_1\left({}_mc_x,\, {}_mc_z\right)\sin\left(\eta_y\right) - It_2\left({}_mc_x,\, {}_mc_z\right)\sin\left(\eta_y\right) \\ -It_4\left({}_mc_x,\, {}_mc_z\right)\cos\left(\eta_y\right) - r_{y2}^{\text{eff}} F_x \end{bmatrix} \\ {}_m\mathbf{T}_{\text{edge 4}}\left({}_m\boldsymbol{c}\right) &= \begin{bmatrix} I\sin\left(\eta_x\right) t_1\left(-{}_mc_y,\, {}_mc_z\right) + I\sin\left(\eta_x\right) t_2\left(-{}_mc_y,\, {}_mc_z\right) \\ -r_{x1}^{\text{eff}} F_z - I\cos\left(\eta_x\right) t_3\left(-{}_mc_y,\, {}_mc_z\right) \\ r_{x2}^{\text{eff}} F_y + I\cos\left(\eta_x\right) t_4\left(-{}_mc_y,\, {}_mc_z\right) \end{bmatrix}. \end{aligned} \tag{3.16} $$

The torque on the mover when a coil enters the corner regions is similarly given by

$$
\begin{aligned}
{}_m\mathbf{T}_{\text{corner 1}}\left({}_m\boldsymbol{c}\right) &= I\begin{bmatrix} -f_3\left(-{}_mc_x,\,{}_mc_z\right)t_1\left({}_mc_y,\,{}_mc_z\right)+n\left({}_mc_z\right)t_3\left(-{}_mc_x,\,{}_mc_z\right)t_2\left({}_mc_y,\,{}_mc_z\right)\\ -t_1\left(-{}_mc_x,\,{}_mc_z\right)f_3\left({}_mc_y,\,{}_mc_z\right)+n\left({}_mc_z\right)t_2\left(-{}_mc_x,\,{}_mc_z\right)t_3\left({}_mc_y,\,{}_mc_z\right)\\ -t_4\left(-{}_mc_x,\,{}_mc_z\right)f_2\left({}_mc_y,\,{}_mc_z\right)+f_2\left(-{}_mc_x,\,{}_mc_z\right)t_4\left({}_mc_y,\,{}_mc_z\right)\end{bmatrix}\\
{}_m\mathbf{T}_{\text{corner 2}}\left({}_m\boldsymbol{c}\right) &= I\begin{bmatrix} f_3\left({}_mc_x,\,{}_mc_z\right)t_1\left({}_mc_y,\,{}_mc_z\right)-n\left({}_mc_z\right)t_3\left({}_mc_x,\,{}_mc_z\right)t_2\left({}_mc_y,\,{}_mc_z\right)\\ -t_1\left({}_mc_x,\,{}_mc_z\right)f_3\left({}_mc_y,\,{}_mc_z\right)+n\left({}_mc_z\right)t_2\left({}_mc_x,\,{}_mc_z\right)t_3\left({}_mc_y,\,{}_mc_z\right)\\ -t_4\left({}_mc_x,\,{}_mc_z\right)f_2\left({}_mc_y,\,{}_mc_z\right)+f_2\left({}_mc_x,\,{}_mc_z\right)t_4\left({}_mc_y,\,{}_mc_z\right)\end{bmatrix}\\
{}_m\mathbf{T}_{\text{corner 3}}\left({}_m\boldsymbol{c}\right) &= I\begin{bmatrix} -f_3\left(-{}_mc_x,\,{}_mc_z\right)t_1\left(-{}_mc_y,\,{}_mc_z\right)+n\left({}_mc_z\right)t_3\left(-{}_mc_x,\,{}_mc_z\right)t_2\left(-{}_mc_y,\,{}_mc_z\right)\\ t_1\left(-{}_mc_x,\,{}_mc_z\right)f_3\left(-{}_mc_y,\,{}_mc_z\right)-n\left({}_mc_z\right)t_2\left(-{}_mc_x,\,{}_mc_z\right)t_3\left(-{}_mc_y,\,{}_mc_z\right)\\ -t_4\left(-{}_mc_x,\,{}_mc_z\right)f_2\left(-{}_mc_y,\,{}_mc_z\right)+f_2\left(-{}_mc_x,\,{}_mc_z\right)t_4\left(-{}_mc_y,\,{}_mc_z\right)\end{bmatrix}\\
{}_m\mathbf{T}_{\text{corner 4}}\left({}_m\boldsymbol{c}\right) &= I\begin{bmatrix} f_3\left({}_mc_x,\,{}_mc_z\right)t_1\left(-{}_mc_y,\,{}_mc_z\right)-n\left({}_mc_z\right)t_3\left({}_mc_x,\,{}_mc_z\right)t_2\left(-{}_mc_y,\,{}_mc_z\right)\\ t_1\left({}_mc_x,\,{}_mc_z\right)f_3\left(-{}_mc_y,\,{}_mc_z\right)-n\left({}_mc_z\right)t_2\left({}_mc_x,\,{}_mc_z\right)t_3\left(-{}_mc_y,\,{}_mc_z\right)\\ -t_4\left({}_mc_x,\,{}_mc_z\right)f_2\left(-{}_mc_y,\,{}_mc_z\right)+f_2\left({}_mc_x,\,{}_mc_z\right)t_4\left(-{}_mc_y,\,{}_mc_z\right)\end{bmatrix}.
\end{aligned}
\tag{3.17}
$$

where $n({}_mc_z) = \alpha_n \cdot |{}_mc_z| + \beta_n$ is another function whose constants, $\alpha_n$ and $\beta_n$, are fit with numeric data used for normalization. The computational speeds of calculating the forces and torques on the mover from a single coil compared to traditional numeric integration techniques are shown in Table 3.2.

Table 3.2: Computation times (in seconds) for calculating the forces and torques on two mover units using different methods. Time values are averaged over 50 different mover pose orientations. Numerical integration utilizes the midpoint method for the Force/Torque calculation and the magnetic node method for magnetic flux density calculation with 69120 voxel units. The number of magnetic nodes for the 6 Pole and 5 Pole Halbach Movers is 960 and 680, respectively.

| Mover Unit Type | Numerical Integration | | Data Driven | |
|---|---|---|---|---|
| | Mean | Standard Deviation | Mean | Standard Deviation |
| 6 Pole | 6.9 | 0.13 | $2.9\times10^{-3}$ | $1.4\times10^{-3}$ |
| 5 Pole | 3.8 | 0.29 | $3.0\times10^{-3}$ | $1.4\times10^{-3}$ |

## 3.4 Adaptive Control & Linear Quadratic Controllers

Adaptive control refers to a class of control techniques that enable a system to drive its state toward a desired trajectory or setpoint, even in the presence of unknown or uncertain model parameters. When system dynamics are inaccurately modeled or subject to unmodeled variations, traditional linear controllers may become unstable or fail to perform adequately under non-optimal conditions. Originally motivated by the need for robust automation in early aircraft systems [76], adaptive control has since evolved into a powerful framework for enhancing the flexibility and robustness of modern control systems. It allows for real-time compensation of parametric uncertainty and, as demonstrated in this research, can also be leveraged to extract useful information for the end user. A typical adaptive control architecture consists of three main components: (1) system and parameter identification, (2) parameter identification algorithms and modifications, and (3) control laws that govern system behaviour based on the updated parameters.

### 3.4.1 System and Parameter Identification (PI)

All static and dynamic systems are governed by a set of equations that encapsulate the physical laws of their behaviour. If all the parameters in these models were known with perfect accuracy at all times, the system's future evolution could be predicted precisely. However, when these parameters are unknown or modeled inaccurately, control designs based on them can lead to unstable or unreliable behaviour.

A common approach to handling such uncertainties is to reformulate the governing equations in a way that isolates the unknown parameters from the known, measurable, and controllable quantities. This reformulation is known as a *parametric model*, and it serves as the foundation for many adaptive control strategies. While various types of parametric models exist (see [77] for alternatives), this work adopts the static parametric model (SPM).

Given a system's governing equation, the SPM is a reformulation that expresses the measurable output $z \in \mathbb{R}$ as the product of known signal terms $\phi \in \mathbb{R}^n$ and an unknown parameter vector $\theta^* \in \mathbb{R}^n$, as follows:

$$z = \theta^{*T}\phi. \tag{3.18}$$

The signals $z(t)$ and $\phi(t)$ are formed from a linear combination of quantities that are controllable or available for measurement. The true value of the unknown parameter is

denoted as $\theta^*$ where an estimate is denoted as $\hat{\theta}(t)$. This formulation is linear in the parameters and provides a foundation for parameter estimation.

The parameter identification (PI) problem can now be stated as follows: Given known signals $z(t)$ and $\phi(t)$, can an online recursive PI algorithm be constructed so that it ensures the estimated parameter vector $\hat{\theta}(t)$ converges to the true parameter vector $\theta^*$.

### 3.4.2 Parameter Identification Algorithms and Modifications

An estimation model $\hat{z}$ (given by Equation 3.19) is chosen to mirror the SPM described earlier with the unknown parameter vector $\theta^*$ replaced by its time-varying estimate $\hat{\theta}(t)$. The signal $\hat{z}$ represents an estimate of the measured quantity $z$, computed using $\hat{\theta}(t)$. Any discrepancy between $\hat{z}$ and $z$ arises from the difference between the estimated and true parameters. To account for scale and ensure numerical stability, a normalized estimation error is defined in Equation (3.20), using the normalization factor $m_s^2 = \zeta + \eta\phi^T\phi$ for some constants $\zeta, \eta > 0$.

$$\hat{z} = \hat{\theta}(t)^T\phi \tag{3.19}$$

$$\epsilon = \frac{z - \hat{z}}{m_s^2} \tag{3.20}$$

This formulation provides a way to characterize parameter estimation error using only signals available for measurement. A gradient-based algorithm is adopted to minimize the instantaneous cost function:

$$J(\theta) = \frac{1}{2}\epsilon^2 m_s^2 \tag{3.21}$$

By updating the parameters in the direction of the negative gradient of this cost function, i.e., $\dot{\theta} = -\Gamma\nabla J$, the resulting update law becomes:

$$\dot{\theta} = \Gamma\epsilon\phi \tag{3.22}$$

In this application, the parameters to be estimated correspond to the payload mass and its location on the mover. Prior information is available for both: the payload mass is bounded between zero and a known upper limit based on the stator's current capacity, and the location is constrained to a finite region on the mover platform. These constraints can be expressed as $\theta_{\min} \leq \theta(t) \leq \theta_{\max}$. To incorporate these bounds, a projection operator is used to modify the update law, leading to the following constrained adaptation rule:

$$\dot{\theta} = \Pr(-\Gamma \nabla J) = \begin{cases} \Gamma \epsilon \phi, & \text{if } \theta_{\min} < \hat{\theta} < \theta_{\max} \\ & \quad \text{or } (\hat{\theta} = \theta_{\min} \text{ and } \Gamma \epsilon \phi \geq 0) \\ & \quad \text{or } (\hat{\theta} = \theta_{\max} \text{ and } \Gamma \epsilon \phi \leq 0) \\ 0, & \text{otherwise} \end{cases} \tag{3.23}$$

where $\Gamma > 0$ is a positive definite adaptation gain. This projection ensures the parameter estimates remain within their feasible bounds and can accelerate convergence. Taken together, the estimation model (3.19), the normalized error (3.20), and the modified update law (3.23) form the core of the parameter identification algorithm. Theorem 3.1 defines necessary conditions on the input signals and summarizes the convergence properties of such algorithms[4].

**Theorem 3.1 (Parameter Identification Properties)** *The gradient algorithm that is described by Equation 3.23 guarantees the following properties:*

1. *The variables $\varepsilon, \varepsilon m_s$, and $\dot{\theta}$ belong to $\mathcal{L}_2 \cap \mathcal{L}_\infty$ and $\theta \in \mathcal{L}_\infty$.*
2. *If $\frac{\phi}{m_s}$ is persistently excited, that is,*

$$\int_t^{t+T_0} \frac{\phi(\tau)\phi^T(\tau)}{m_s^2(\tau)}\, d\tau > \alpha_0 T_0 I \quad \forall t \geq 0 \tag{3.24}$$

*for some constants $T_0 > 0$, $\alpha_0 > 0$, then $\theta(t) \to \theta^*$ exponentially fast. Furthermore,*

$$(\theta(t) - \theta^*)^T \Gamma^{-1} (\theta(t) - \theta^*) \leq (1 - \gamma_1)^n (\theta(0) - \theta^*)^T \Gamma^{-1} (\theta(0) - \theta^*), \tag{3.25}$$

*where $0 \leq t \leq nT_0$, $n = 0, 1, 2, \ldots$, and*

$$\gamma_1 = \frac{2\alpha_0 T_0 \lambda_{\min}(\Gamma)}{2 + \beta^4 \lambda_{\max}^2(\Gamma) T_0^2}, \quad \beta = \sup_t \left\| \frac{\phi(t)}{m_s(t)} \right\|. \tag{3.26}$$

3. *If the plant model has stable poles and no zero-pole cancellations, and if the input $u$ is sufficiently rich of order $n + m + 1$—that is, it contains at least $\frac{n+m+1}{2}$ distinct frequencies—then both $\phi$ and $\frac{\phi}{m_s}$ are persistently excited. In this case, the following quantities converge to zero exponentially fast: $|\theta(t) - \theta^*|$, $\varepsilon$, $\varepsilon m_s$, $\dot{\theta}$.*

[4]The proof is shown in [77] and the reader is encouraged to go there for further details regarding adaptive control.

### 3.4.3 Adaptive LQR Control and Error Tracking Formulation

Building upon the parameter identification framework discussed previously, this section presents how the estimated parameters can be used to generate control inputs in an adaptive feedback loop. Adaptive control, by nature, is a model-based strategy in which the real-time parameter estimates are used to continuously update the system model that governs the control law. As such, a suitable control law must be chosen.

Among the various model-based control schemes available, this work adopts the linear quadratic regulator (LQR) due to its simplicity, tractable mathematical structure, and widespread use in industrial control applications [78]. The standard practice involves first expressing the system dynamics in a linear time-invariant state-space form:

$$\dot{\mathbf{x}} = \mathbf{A}(\theta)\mathbf{x} + \mathbf{B}(\theta)\mathbf{u}, \tag{3.27}$$

where $\mathbf{x} \in \mathbb{R}^n$ is the state vector, $\mathbf{u} \in \mathbb{R}^m$ is the control input, and the system matrices $\mathbf{A}(\theta)$, $\mathbf{B}(\theta)$ are functions of the unknown parameter vector $\theta$.

The control objective is to regulate the state $\mathbf{x}(t)$ to the origin by minimizing the following infinite-horizon quadratic cost function:

$$J = \int_0^\infty \left(\mathbf{x}^T\mathbf{Q}\mathbf{x} + \mathbf{u}^T\mathbf{R}\mathbf{u}\right) dt, \tag{3.28}$$

where $\mathbf{Q} = \mathbf{Q}^T \succeq 0$ penalizes the state and $\mathbf{R} = \mathbf{R}^T \succ 0$ penalizes the control input. The optimal control input that minimizes (3.28) subject to (3.27) is given by:

$$\mathbf{u} = -\mathbf{R}^{-1}\mathbf{B}^T\mathbf{S}\mathbf{x}, \tag{3.29}$$

where $\mathbf{S} \in \mathbb{R}^{n\times n}$ is the positive semi-definite solution to the Algebraic Riccati Equation (ARE):

$$0 = \mathbf{S}\mathbf{A} + \mathbf{A}^T\mathbf{S} - \mathbf{S}\mathbf{B}\mathbf{R}^{-1}\mathbf{B}^T\mathbf{S} + \mathbf{Q}. \tag{3.30}$$

Existing literature may further denote the *kalman gain* as $\mathbf{K} = \mathbf{R}^{-1}\mathbf{B}^T\mathbf{S}$ which simplifies the control input (Equation 3.29) notation as $\mathbf{u} = -\mathbf{K}\mathbf{x}$.

Since the system matrices depend on the unknown parameters $\theta$, the adaptive control law is implemented by updating the system matrix estimates $\hat{\mathbf{A}}(\hat{\theta}(t))$ and $\hat{\mathbf{B}}(\hat{\theta}(t))$ at each time step using the latest parameter estimates. The control sequence is then executed as follows:

$$\text{Control Sequence} \rightarrow \begin{cases} \text{Step 1:} & \mathbf{S} \text{ solves } 0 = \mathbf{S}\hat{\mathbf{A}} + \hat{\mathbf{A}}^T\mathbf{S} - \mathbf{S}\hat{\mathbf{B}}\mathbf{R}^{-1}\hat{\mathbf{B}}^T\mathbf{S} + \mathbf{Q}, \\ \text{Step 2:} & \mathbf{u} = -\mathbf{K}\mathbf{x} \text{ where } \mathbf{K} = \mathbf{R}^{-1}\hat{\mathbf{B}}^T\mathbf{S}. \end{cases} \tag{3.31}$$

While the above method regulates the system to the origin, in many applications, the goal is to track a desired trajectory. This can be accomplished by reformulating the control objective in terms of a tracking error [78]. Consider a $n$th-order linear ordinary differential equation with a single input $u$ and some arbitrary state $x$:

$$\frac{d^n x}{dt^n} + a_{n-1}\frac{d^{n-1}x}{dt^{n-1}} + \cdots + a_1\frac{dx}{dt} + a_0 x = u \tag{3.32}$$

for some constants $a_{n-1}, ..., a_1, a_0$. Define the differential operator

$$D\{\cdot\} = \frac{d^n}{dt^n} + a_{n-1}\frac{d^{n-1}}{dt^{n-1}} + \cdots + a_1\frac{d}{dt} + a_0$$

so that $D\{x\} = u$. Then define the tracking error as

$$e = x_d - x, \tag{3.33}$$

where $x_d(t)$ is the desired reference trajectory. Applying the operator $D\{\cdot\}$ yields:

$$D\{e\} = D\{x_d - x\} = D\{x_d\} - D\{x\}. \tag{3.34}$$

If the reference signal is chosen such that $D\{x_d\} = 0$, the error dynamics reduce to

$$D\{e\} = -D\{x\} = -u, \quad \forall t. \tag{3.35}$$

In this case, the error system has the same structure as the original system, up to a negative sign. Since negation does not affect controllability or observability, the same LQR design can be applied directly to the error dynamics by replacing $\mathbf{x} \to \mathbf{e}$. This enables trajectory tracking for any reference $x_d(t)$ satisfying $D\{x_d\} = 0$. The corresponding error tracking control sequence becomes:

$$\text{Error Tracking Control Sequence} \to \begin{cases} \text{Step 1:} & 0 = \mathbf{S}\hat{\mathbf{A}} + \hat{\mathbf{A}}^T\mathbf{S} - \mathbf{S}\hat{\mathbf{B}}\mathbf{R}^{-1}\hat{\mathbf{B}}^T\mathbf{S} + \mathbf{Q}, \\ \text{Step 2:} & \mathbf{u} = -\mathbf{K}\mathbf{e} \text{ where } \mathbf{K} = \mathbf{R}^{-1}\hat{\mathbf{B}}^T\mathbf{S}. \end{cases} \tag{3.36}$$

**Aside:** Given that the system in question follows Newton's Second Law—as formulated in Section 5.2.2—it is useful to determine which trajectories satisfy the

condition $D\{x_d\} = 0$. Since the system is second order, we define the operator as:

$$D\{\cdot\} = \frac{d^2}{dt^2} + a_1\frac{d}{dt} + a_0, \tag{3.37}$$

$$D\{x_d\} = \frac{d^2x_d}{dt^2} + a_1\frac{dx_d}{dt} + a_0x_d = 0. \tag{3.38}$$

This is a homogeneous linear second-order differential equation. The general solution to this equation defines the class of reference trajectories $x_d(t)$ that the system can track using the error-state formulation discussed earlier. Solving this equation yields:

$$x_d(t) = c_1e^{\lambda_1 t} + c_2e^{\lambda_2 t}, \tag{3.39}$$

where $\lambda_1$ and $\lambda_2$ are the roots of the characteristic equation:

$$\lambda^2 + a_1\lambda + a_0 = 0, \tag{3.40}$$

and $c_1, c_2 \in \mathbb{R}$ are arbitrary constants determined by initial conditions. If the characteristic equation has real and distinct roots, the solution will be a linear combination of exponential functions. If the roots are complex, $x_d(t)$ will be an exponentially damped (or increasing) sinusoid, and if there is a repeated real root, the solution takes the form:

$$x_d(t) = (c_1 + c_2t)e^{-\frac{a_1}{2}t}. \tag{3.41}$$

The set of trackable trajectories under these formulations includes any signals that lie in the nullspace of the differential operator $D\{\cdot\}$. These reference trajectories represent the system's natural response and are exactly those that can be tracked asymptotically to zero by applying the control law derived in Equation (3.36).

Theorem 3.2 summarizes the conditions under which a linear time-invariant system ensures asymptotic stability. Since the system matrices of the system are of the form

$$\mathbf{A} = \begin{bmatrix} 0 & 1 & 0 \\ 0 & 0 & 0 \\ 1 & 0 & 0 \end{bmatrix} \quad , \quad \mathbf{B} = \begin{bmatrix} 0 \\ b \\ 0 \end{bmatrix} \tag{3.42}$$

for some parameter $b$ depending on the axis (details in Section 5.2.2), the penalty matrices $\mathbf{Q}$ and $\mathbf{R}$ are chosen as a diagonal matrix with strictly positive values to ensure positive

definiteness and observability with the system matrices. Since the matrix pair $(\mathbf{A}, \mathbf{B})$ of the error system is controllable—and therefore stabilizable—the closed-loop system is guaranteed to be asymptotically stable. A proof for this theorem is presented in [78]. The overall adaptive control framework, including parameter estimation and feedback generation, is illustrated in the block diagram shown in Figure 3.9.

**Theorem 3.2** *Let* $\mathbf{C}$ *be any matrix such that the penalty matrix* $\mathbf{Q} = \mathbf{C}^{\mathrm{T}}\mathbf{C}$. *Suppose the pair* $(\mathbf{A}, \mathbf{C})$ *is observable. Then, the pair of system matrices* $(\mathbf{A}, \mathbf{B})$ *is stabilizable if and only if the following conditions are satisfied:*

1. *There exists a unique positive definite limiting solution* $S(\infty)$ *to the Riccati equation. Moreover,* $S(\infty)$ *is the unique positive definite solution to the Algebraic Riccati Equation:*

$$0 = \mathbf{SA} + \mathbf{A}^T\mathbf{S} - \mathbf{SBR}^{-1}\mathbf{B}^T\mathbf{S} + \mathbf{Q}. \tag{3.43}$$

   *where* $\mathbf{Q} = \mathbf{C}^{\mathrm{T}}\mathbf{C}$ *and* $\mathbf{R} = \mathbf{R}^{\mathrm{T}} \succ 0$ *are the state and control penalty matrices, respectively.*

2. *The closed-loop system*

$$\dot{\mathbf{e}} = (\mathbf{A} - \mathbf{BK})\mathbf{e} \tag{3.44}$$

   *is asymptotically stable, where the optimal state feedback gain* $K$ *is given by*

$$\mathbf{K} = \mathbf{R}^{-1}\mathbf{B}^T\mathbf{S}. \tag{3.45}$$

### 3.4.4 Discrete Derivative and Integration

The adaptive linear quadratic regulator (ALQR) control scheme derived above assumes that the full state vector is available for feedback. However, in the present system, only position measurements are directly accessible through the motion capture setup (see Section 4.3). To approximate the full state, discrete-time differentiation and integration techniques are employed. Let $f(t)$ represent a time-varying scalar signal sampled at a uniform interval $\Delta t$. At discrete time index $n$, with $t_n = n\Delta t$, the first-order backward difference approximation is used to estimate the time derivative:

$$\frac{df(t_n)}{dt} \approx \frac{f(t_n) - f(t_{n-1})}{\Delta t}. \tag{3.46}$$

Conversely, when estimating the integral of a signal $f(t)$, the backward Euler method is applied. Let $F_n$ denote the discrete-time estimate of the integral up to time $t_n$, then:

$$F_n = F_{n-1} + \Delta t \cdot f(t_n), \tag{3.47}$$

where $F_0$ is initialized to zero or some known value. These approximations enable real-time estimation of the full state vector from position data alone. To mitigate the effects of high-frequency measurement noise inherent in discrete differentiation, a low-pass filter is applied to the derivative estimate. This is given by the following equation, in the z-domain, as

$$G(z) = \frac{\frac{T}{T_c} z}{z + \left(\frac{T}{T_c} - 1\right)} \tag{3.48}$$

where $T$ is the sample time of 1 ms and $T_c$ is the time constant for the filter. This time constant was chosen to be 2 ms for the 64-coil TestBench, as reported when it was first constructed by [79].

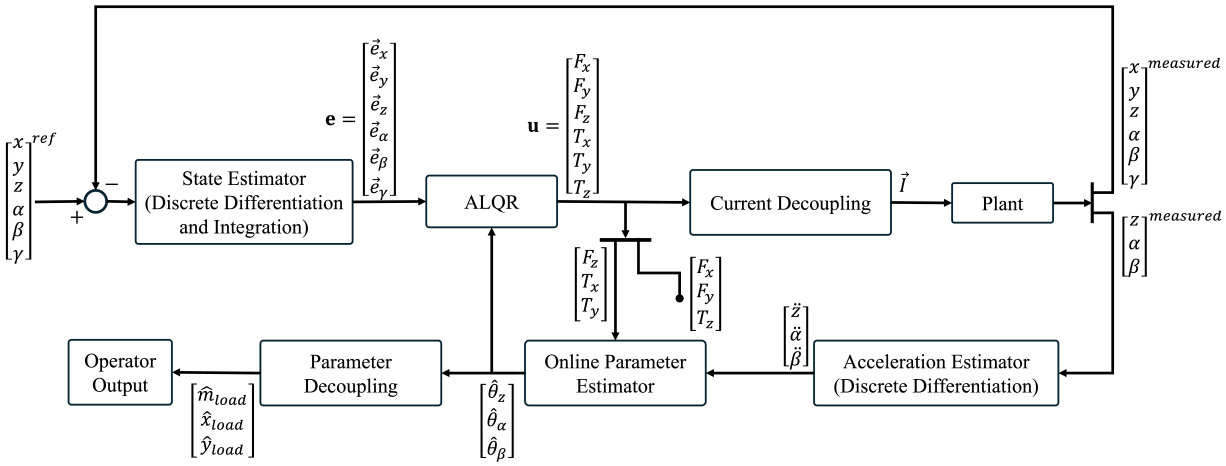



Figure 3.9: Block diagram representation of the Maglev system. The input to the plant is the desired net forces and torques on the system (which is converted to coil currents in the "current decoupling" block). The output is the mover position and orientation in the global reference frame.

Table 3.3: Relevant equations to the control blocks present in the overall control block diagram (given in Figure 3.9).

| Block | Associated Equations | Relevant Sections |
|---|---|---|
| ALQR | $\mathbf{u} = -\mathbf{Ke}$ where $\mathbf{K} = \mathbf{R}^{-1}\hat{\mathbf{B}}^T\mathbf{S}$ and $\mathbf{S}$ satisfies $0 = \mathbf{S}\hat{\mathbf{A}} + \hat{\mathbf{A}}^T\mathbf{S} - \mathbf{S}\hat{\mathbf{B}}\mathbf{R}^{-1}\hat{\mathbf{B}}^T\mathbf{S} + \mathbf{Q}$ | 3.4.3 |
| Online Parameter Estimator | $\int \dot{\theta} dt$ where $\dot{\theta} = \Pr(-\Gamma\nabla J)$<br>$\hat{z} = \hat{\theta}(t)^T\phi \quad , \quad \epsilon = \frac{z-\hat{z}}{m_s^2}$ | 3.4.1<br>3.4.2 |
| State/Acceleration Estimator | The discrete integration and derivative of the necessary state $f$ using $\frac{df(t_n)}{dt} \approx \frac{f(t_n)-f(t_{n-1})}{\Delta t}, F_n = F_{n-1} + \Delta t \cdot f(t_n)$ | 3.4.4 |
| Parameter Decoupling | $\hat{m}_{load} = \hat{\theta}_z$ , $\hat{x}_{load} = -\frac{\hat{\theta}_\beta}{\hat{\theta}_z+\epsilon}$, $\hat{y}_{load} = \frac{\hat{\theta}_\alpha}{\hat{\theta}_z+\epsilon}$ | 5.2.2 |
| Current Decoupling | $\mathbf{I} = \mathbf{\Gamma}^T(\mathbf{\Gamma}\mathbf{\Gamma}^T)^{-1}\boldsymbol{W}_{total}$ | 5.1.2 |

# Chapter 4

# Electromagnetic Hardware Design

This section provides a comprehensive overview of the hardware components integral to the magnetic levitation system utilized in this research. The system comprises three primary subsystems: *Stator Assembly* – This includes the electromagnetic coils responsible for generating the actuation magnetic field, along with the necessary amplifiers and control electronics that regulate coil operation. *Mover Unit* – A fully isolated component featuring permanent magnets. The mover is designed to interact with the stator's magnetic field without any direct power connection. *Measurement and Control System* – This encompasses the sensors, data acquisition hardware, and control computer that monitor and manage the system's performance. Throughout the following sections, each component is detailed with respect to its design specifications, material selections, and functional roles within the overall system.

## 4.1 Stator Assembly

The primary testing system utilized in this thesis is the Magnetic Levitation Testing Bench, referred to as the TestBench. This system was designed, fabricated, and assembled by the MagLev Microrobotics Laboratory team. It functions as the stator for the magnetic movers and consists of sixty-four rounded square coils, arranged in an $8 \times 8$ grid. The coils are spaced in three-inch intervals in both the x and y directions, with all coils aligned at the same height along the z-axis. Each row of coils is mounted on an aluminum frame and reinforced by a steel structure to provide overall structural stability. The aluminum frame also plays a key role in minimizing magnetic hysteresis effects between the coils and the steel structure.

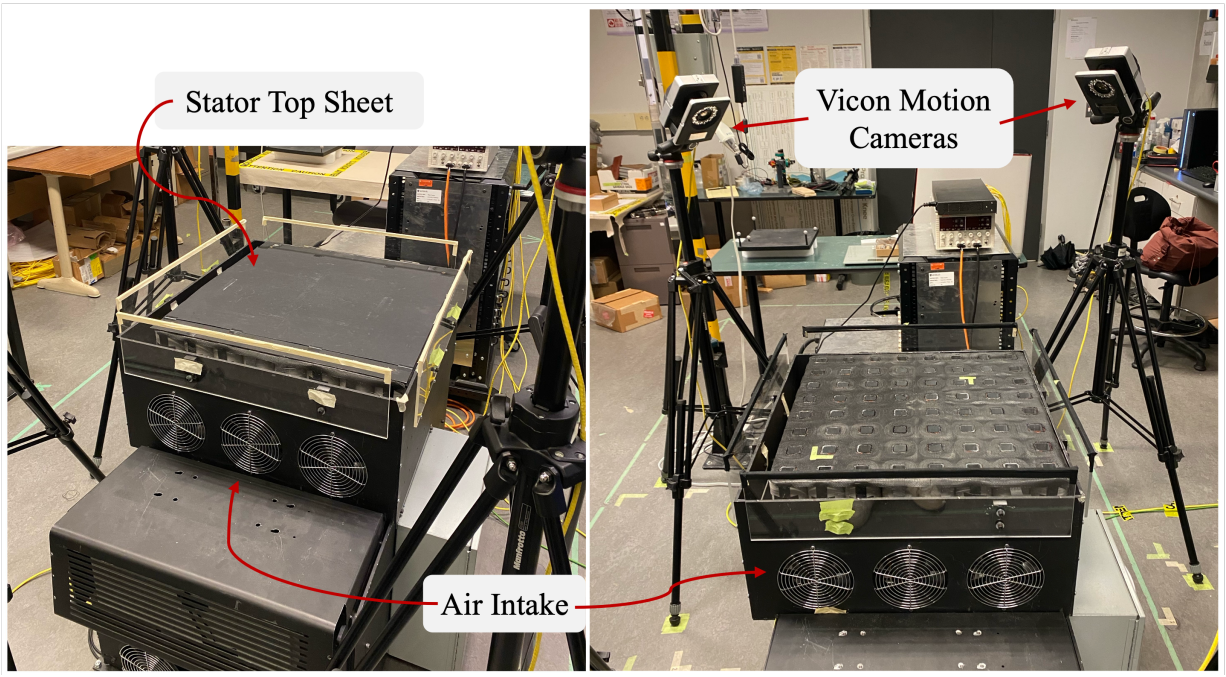



Figure 4.1: Multiple perspectives of TestBench, the rapid testing planar magnetic levitation platform located in the Maglev Microrobotics Laboratory. The xy-plane corresponds to the top level of the coils, with a total levitation area of 610 mm × 610 mm (24″ × 24″).

The current amplifiers, housed within the steel structure, are capable of supplying up to 80 VDC (Volts Direct Current) and 10 A to each coil. However, to prevent overheating and excessive current flow, the maximum current supplied to each coil is limited to 9 A through the control interface. Although the system includes thermocouples for monitoring the temperature of coil pairs, they were not actively used in this research. Heat dissipation from both the coils and the electronics is managed through a built-in cooling system, which uses fans to continuously direct cooler air across the coils, preventing thermal buildup. The dimensions and characteristics of the coils are detailed in Table 4.1. The total levitation area of the TestBench measures 610 mm × 610 mm (24” × 24”).

### 4.1.1 Electromagnetic Coil Design

The coils used in this apparatus are designed as squared solenoids with rounded corners—a schematic is shown in Figure 4.2. This design was chosen based on previous studies comparing it to cylindrical coils, which found that rounded square coils produce a higher

average magnetic field strength across the surface [52]. The specific dimensions of the coil are provided in Table 4.1, with the inner and outer coil widths determined from commercially available aluminum square tubing and the thickness of the copper wire used in the windings. Trakarnchaiyo et al. optimized the coil's height using the Fabry factor, a dimensionless measure that helps achieve near-optimal magnetic flux density [33].

Structurally, each coil features a hollow aluminum frame—known as a bobbin—filled with air. This aluminum structure not only provides mechanical stability and prevents deformation of the windings under repeated loading but also functions as a heat sink, dissipating excess heat generated during extended operation. Regardless of the aluminum bobbin, the modeling of these coils assumes a perfect air coil, an approach taken to eliminate complexities associated with magnetic hysteresis effects. This is assumed since aluminum is paramagnetic and, as such, demonstrates very little magnetic hysteresis. As well, the small thickness of the aluminum minimizes the impact of induced eddy currents on the magnetic field. To further enhance the durability and integrity of the coils, they are wrapped in fibreglass cloth tape, and the top surface is coated with epoxy to prevent the unwinding of the copper wire. These protective measures ensure the long-term stability of the coils during operation while maintaining consistent performance characteristics.

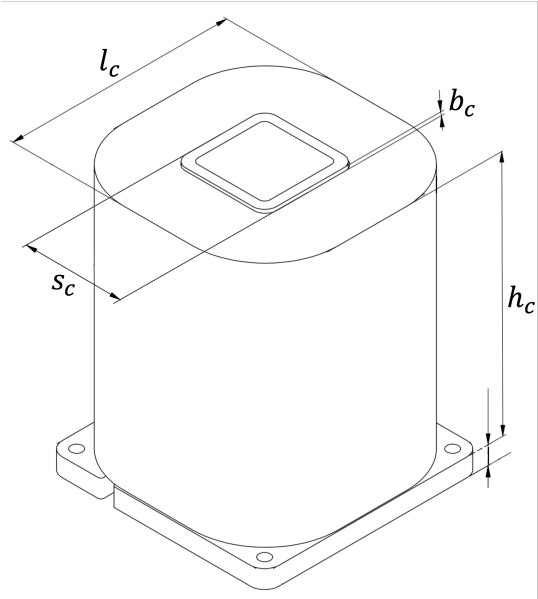



Figure 4.2: Design of a single electromagnetic coil. Detailed dimensions are provided in Table 4.1.

Table 4.1: Dimensions of the rounded square coils used in the TestBench for generating the levitation field.

| Parameter | Values |
|---|---|
| Outer width ($l_c$) | 75 mm |
| Inner width ($s_c$) | 32 mm |
| Height ($h_c$) | 86.5 mm |
| Bundle width ($w_c$) | 21.5 mm |
| Bobbin Protrusion ($b_c$) | 1 mm |
| Wire Gauge | 16 AWG |
| Number of turns | 975 $\pm$5 |
| Resistance | 2.6 $\Omega$ |
| Inductance | 17 mH |

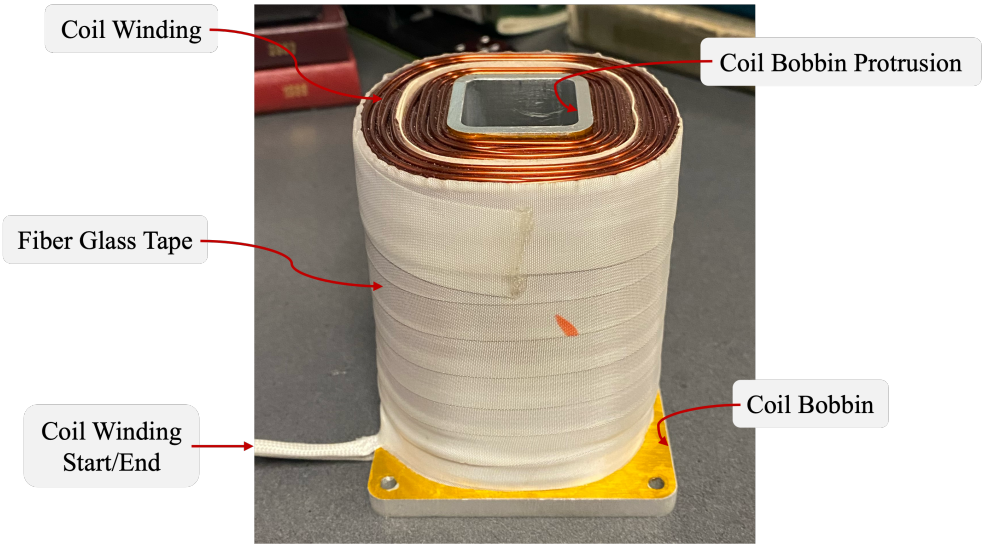



Figure 4.3: Actual coil located within stator.

## 4.2 Mover Units

Two distinct magnetic movers were evaluated in this thesis, both based on variations of the 2D Halbach array configuration mentioned in Chapter 3. The first mover incorporates a 6-pole Halbach array, which utilizes $1'' \times 1'' \times 0.25''$ X, Y, and Z magnets, with a pole pitch of $2''$. These magnets are composed of Neodymium-Iron-Boron (NdFeB) material with a grade of N42, offering a high magnetic field strength and good thermal stability. The magnets are completely housed in an aluminum frame and held in place with epoxy. The Maglev Microrobotics Laboratory team previously constructed this configuration [80]. The selection of this design was driven by the goal of optimizing horizontal acceleration while minimizing power consumption. This optimization was achieved by selecting commercially available magnets with either $1''$ or $1.5''$ square dimensions, which provided a balance between magnetic field strength and system efficiency. The magnets are enclosed within an aluminum housing, and aluminum crossbars are included to reinforce structural integrity. Additionally, reflective markers were affixed to the mover to enable precise tracking within an infrared (IR) motion capture system. Figure 4.4 showcases the final mover assembly and schematic of the magnet's magnetization orientation.

The second mover features a 5-pole Halbach array, composed of $2'' \times 2'' \times 0.5''$ Z magnets and $1'' \times 0.5'' \times 0.5''$ X and Y magnets. These magnets are also made of Neodymium-Iron-Boron (NdFeB) but have a higher grade of N52, providing even greater magnetic field

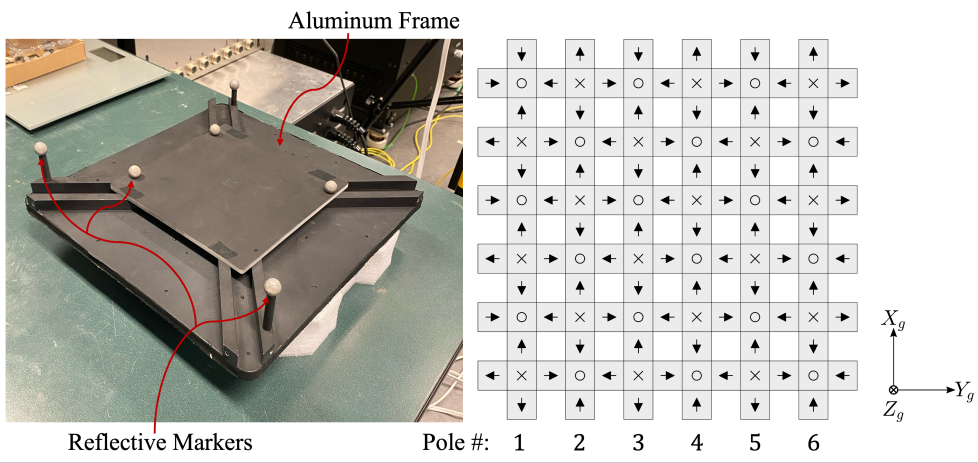



Figure 4.4: 6-pole 2D Halbach magnetic mover unit. *Left:* Perspective view of the assembled mover unit. *Right:* Schematic showing the magnetization vectors of each permanent magnet, viewed from the bottom (i.e., bottom of the mover facing the observer).

strength to enhance the payload-carrying capacity of the levitation system. The magnets are housed in an aluminum case that includes a 0.25″ top plate. Unlike the first mover, the bottom of this mover's case is coated with a layer of clear epoxy, which serves to reduce the magnetic damping effect caused by the stator coils. Additionally, the epoxy was leveled using a CNC machine to compensate for the curvature induced by the internal magnetic forces and achieve a flat, even bottom surface. To prevent unwanted light interference during motion tracking, the mover was painted black, and reflective markers were applied for use with the IR motion capture system. Figure 4.5 showcases the final mover assembly and schematic of the magnet's magnetization orientation. The center view showcases the epoxy bottom layer where the physical magnets are visible.

Table 4.2: Mover unit properties

| Mover Unit Type | 6 Pole Mover | 5 Pole Mover |
|---|---|---|
| Magnet Grade | N42 | N52 |
| $B_r$ | 1.32 T | 1.48 T |
| Pole Pitch ($\tau$) | 50.8 mm | 63.5 mm |
| Magnet Height | 6.35 mm | 12.7 mm |
| Z Magnet Width ($\tau_m$) | 25.4 mm | 50.8 mm |

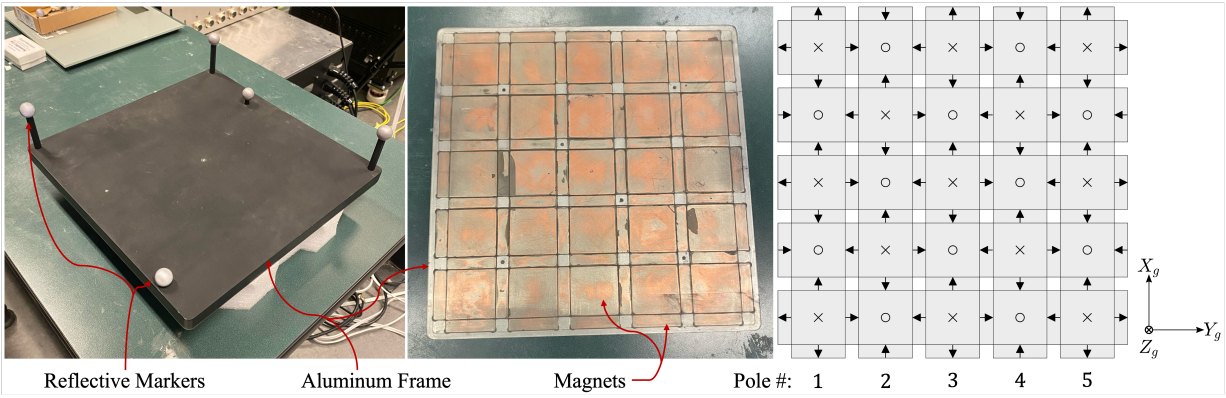



Figure 4.5: 5-pole 2D Halbach magnetic mover unit. *Left:* Perspective view of the assembled mover unit. *Middle:* Bottom view of the assembled mover unit. The bottom is covered in a clear epoxy. *Right:* Schematic showing the magnetization vectors of each permanent magnet, viewed from the bottom (i.e., bottom of the mover facing the observer).

### 4.2.1 Force and Torque Zones

To determine the zones in which to calculate the edge effect of the Halbach, the magnetic flux density along the $X_m$ and $Y_m$ axes under the Halbach array is compared using two methods: the magnetic node model and the harmonic model. Regions under the array which closely align with a simple harmonic function define the central area; regions that significantly deviate construct the edge and corner regions. This method was first presented by Xu et al., and results for the 6-pole mover have already been reported [58]. For the 6-pole mover, since the width of the z magnets ($\tau_m$) is on the same scale as the width of the x and y magnets, a first-order harmonic series is used. The values are reported in [58] and have been independently verified here within—Figure 4.7 displays the results from this analysis. For the 5-pole mover, since the z magnets are much larger than the x and y magnets, a third-order harmonic series is chosen. Figure 4.6 compares the magnetic flux density under the 5-pole mover along the $X_m$ and $Y_m$ axes for an airgap of 1.25″. When the position along the axis is within $2\tau$ of the center, the peak-to-peak error of the x and y components of the magnetic flux density is under 3%. However, within $1.8\tau$ of the center, the $B_z$ deviation is under 2% in both the $X_m$ and $Y_m$ directions. Thus, a box within $\pm 1.8\tau$ in the $X_m$ and $Y_m$ directions defines the central zone. Similarly, beyond $3.6\tau$ from the center, all the magnetic flux density components are within 0.1% of 0. Therefore, $\pm 1.8\tau$ to $\pm 3.6\tau$ defines the boundary where the edge effect of the Halbach is significant. The intersections of these regions in the $X_m$ and $Y_m$ directions define the *corner regions* with

the difference defining the *edge regions*. Figure 4.8 shows these regions for both the 5-pole and 6-pole movers.

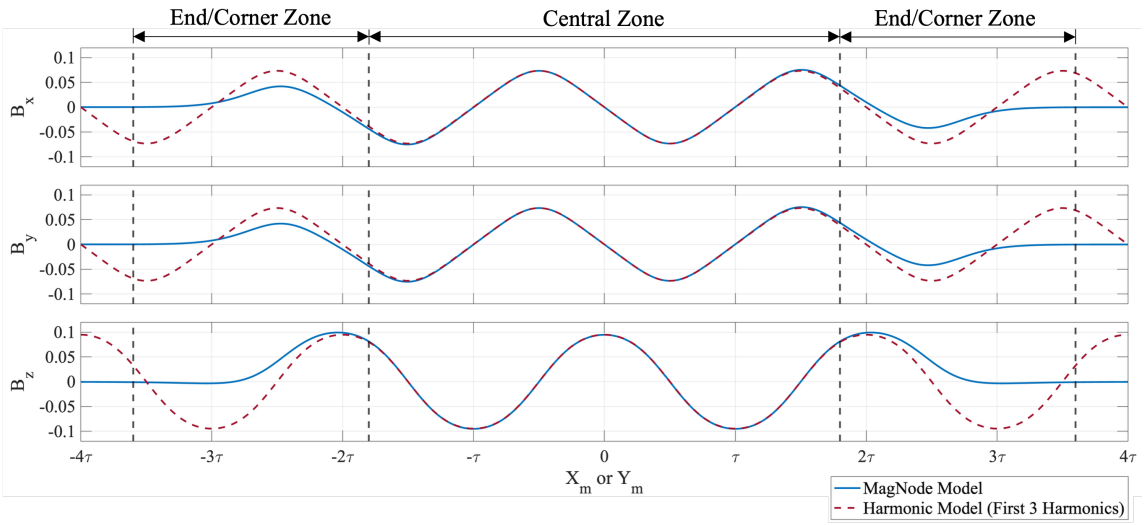



Figure 4.6: Magnetic flux density comparison between the magnetic node and harmonic models for the 5-pole mover.

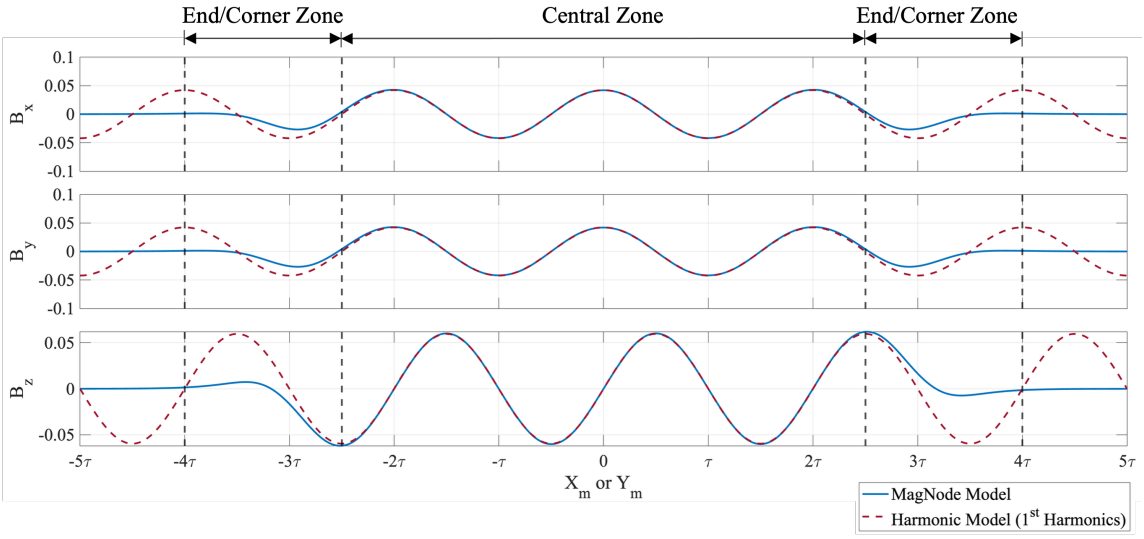



Figure 4.7: Magnetic flux density comparison between the magnetic node and harmonic models for the 6-pole mover. Results are verified using data from [58].

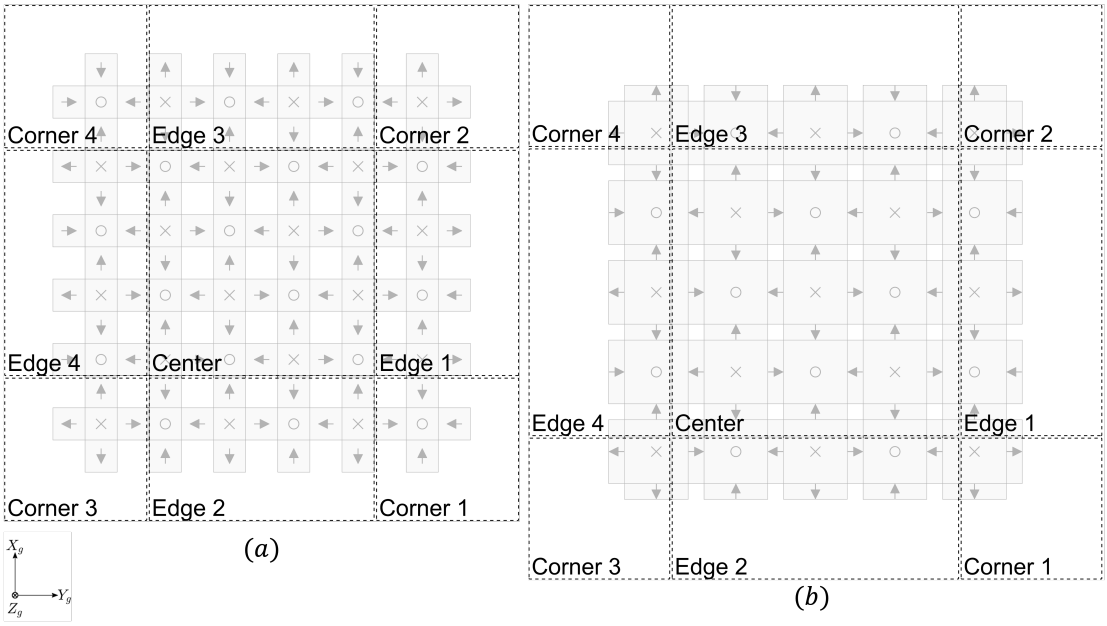



Figure 4.8: Bottom view of the designated regions for computing force and torque distributions under a 2D Halbach array. (a) corresponds to the 6-pole mover, while (b) corresponds to 5-pole mover. The division for the 6-pole mover was first done by [58] and verified for this work. The same method was applied to the 5-pole mover. Regions are to scale.

### 4.2.2 Maximum Weight of Payload

Levitation occurs only when the stator generates sufficient electromagnetic force to counteract the gravitational force acting on the mover. This force must first support the mover's own mass, and any remaining capacity can be used to lift additional load or produce horizontal acceleration. The overall levitation performance is therefore governed by a tradeoff between two competing factors: the strength of the embedded magnets and the total mass of the mover. While stronger magnets reduce the required stator effort, a heavier mover demands more from the coils. In the case of the 5-pole Halbach mover, although higher-grade magnets are used compared to the 6-pole mover, its total mass is nearly twice as large. As a result, a more detailed analysis is needed to quantify the additional payload mass each mover can carry across the stator workspace without violating system limits.

To evaluate the maximum allowable payload mass, simulations were performed over a grid of $(x, y)$ positions within the green-shaded region shown in Figure 4.9. The horizontal symmetry of the stator allows the results in this region to be applied throughout the entire

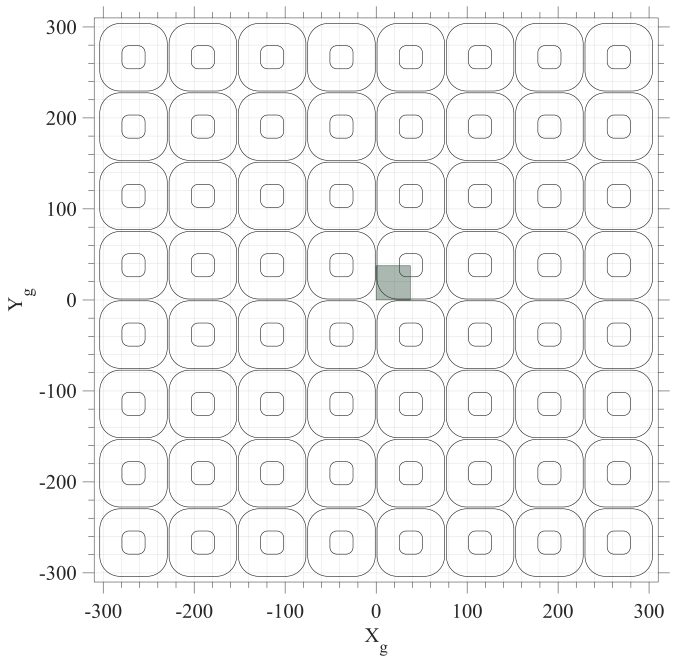



Figure 4.9: Top-down schematic of the stator assembly. The shaded green area denotes the evaluation region. Due to the symmetry of the stator layout in the $x$-$y$ plane, performance metrics computed within this region are representative of the entire working area.

working area. At each position, the required current in every coil to levitate the mover when its center is at this location was computed using the data-driven modeling approach described in Section 3.3.3. The number of coils activated is based on the positioning of the mover and is outlined in Section 5.1.1; if a current limit is reached for a particular coil, a recalibration strategy is invoked as outlined in Section 5.1.3. A strict threshold of eight simultaneously saturated coils was chosen to determine the maximum allowable payload mass—any location where this threshold is exceeded renders that loading weight as non-viable for levitation. The nominal levitation height used for this analysis is 8 mm, which corresponds to a roughly 3 mm air gap when accounting for the thicknesses of the mover's bottom plate, coil bobbin protrusion, and stator top sheet. This height represents a conservative operating point for both movers. At this air gap, the relationship between payload mass and coil saturation is shown in Figure 4.10. The plot shows the number of saturated coils as a function of payload mass; the maximum load is determined as the largest payload mass for which the coil current in all stator positions remains below or equal to the saturation limit. For an 8 mm mover z-height, the 5-pole mover can support up to 3.12 kg, and the 6-pole mover can support up to 1.54 kg.

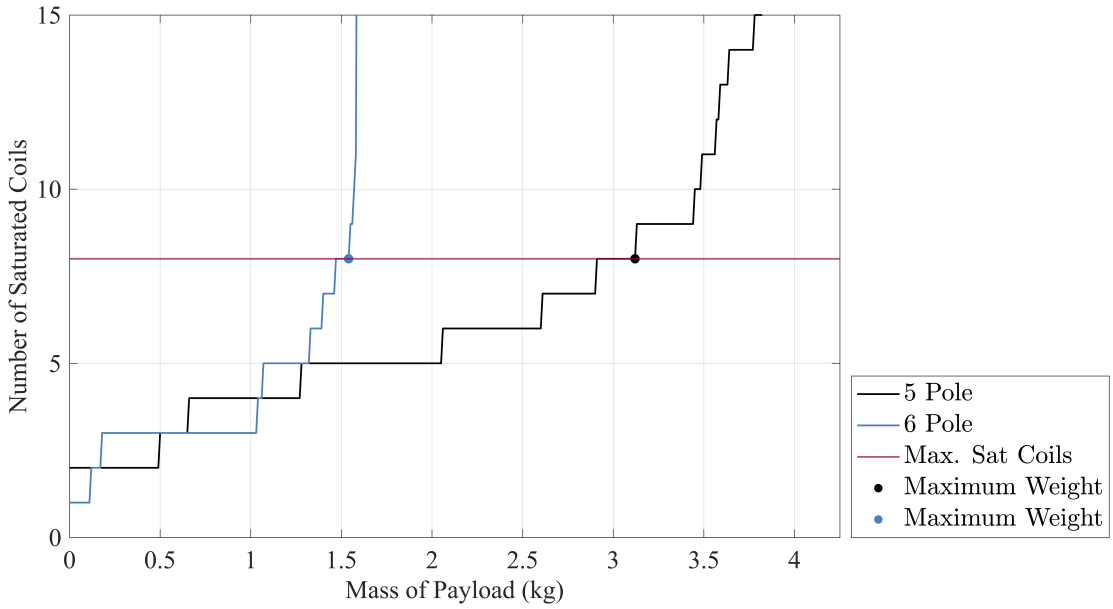



Figure 4.10: Number of saturated coils as a function of payload mass for each mover. The maximum supported payload is indicated by an 'o' marker for each respective mover. The red line denotes the maximum allowable number of saturated coils for the present stator assembly.

To further explore how the levitation height affects maximum payload capacity, simulations were carried out across a range of z-heights. Since the magnetic model used in this work is data-driven, its validity is restricted to the range of z-heights for which simulation data was fitted. For the 6-pole Halbach mover, the model was fitted using data spanning from 0 mm to 8 mm, while for the 5-pole Halbach mover, the fitting range extended from 0 mm to 15.5 mm. The simulation results, shown in Figure 4.11, illustrate the trend in maximum allowable payload mass as a function of levitation height within these ranges. Due to mechanical constraints, including the coil bobbin height, the stator top sheet thickness, and the bottom plate of the mover unit, levitation at heights below 5 mm is physically infeasible. Therefore, only values above 5 mm are shown in the plot. As expected, the maximum liftable mass increases as the air gap decreases, provided that the model remains valid within the fitted z-range.

Although using the eight-saturated-coil threshold across all stator positions provides a general bound on operating conditions, this constraint can be relaxed if the trajectory is restricted to favourable regions of the stator. As the magnetic field underneath the mover is not uniform, specific alignments between the mover magnets and underlying coils can

sustain heavier loads while still keeping the number of saturated coils below the limit. These viable regions are indicated by darker blue areas in the second row of Figures 4.12a and 4.12b. The extent of these regions decreases as the load mass increases, which implies that transporting heavier payloads is only feasible along carefully planned paths. Any stator location that requires more than eight saturated coils is shown using a common color. The top row of the same figures shows the maximum current demanded by any single coil at each stator location, for selected payload masses. These plots provide insight into how current draw and saturation are distributed spatially across the stator. Additional plots over finer grids and other loading conditions are provided in Appendix A.

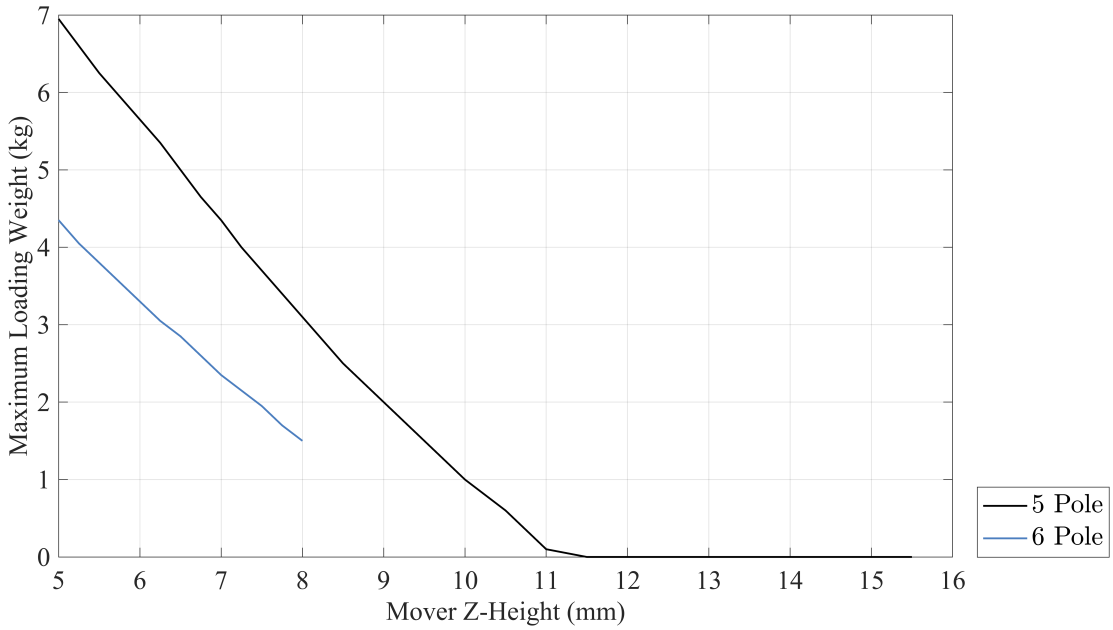
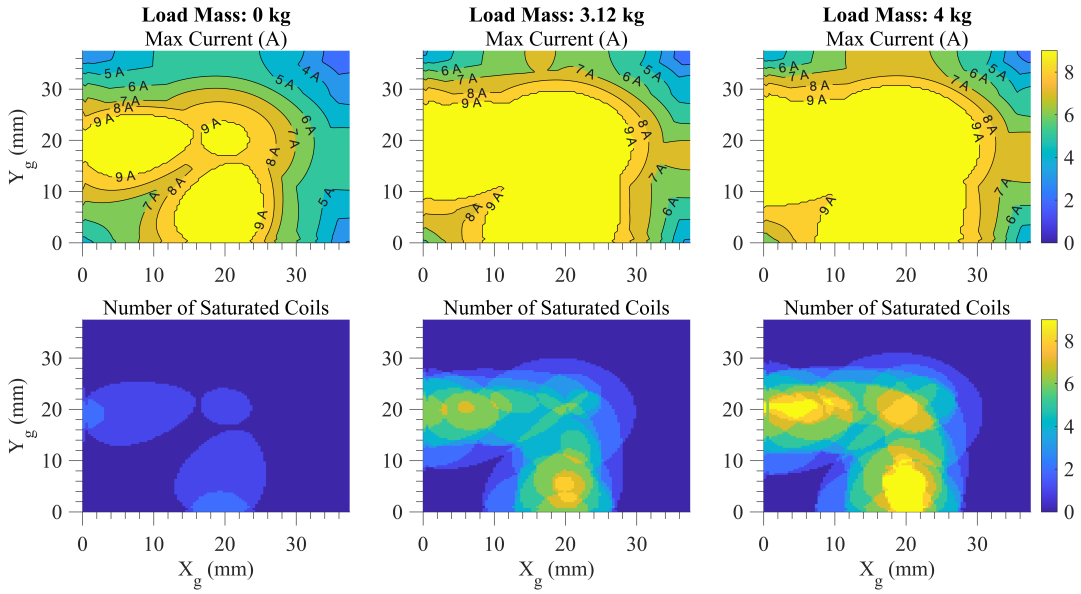
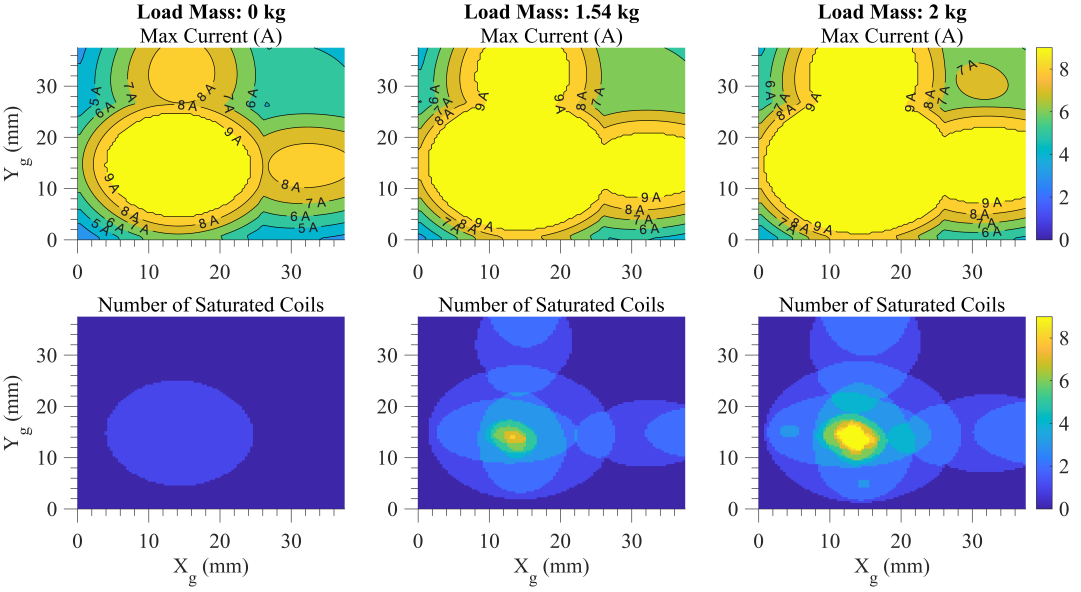



Figure 4.11: Maximum supported payload as a function of the mover's levitation height. Due to the data-driven nature of the force and torque model, the 6-pole mover is fit using data collected from 0 mm to 8 mm, while the 5-pole mover uses data spanning a range of 0 mm to 15.5 mm. Only values above 5 mm are shown, as levitation below this height is not feasible.




(a) Mover unit #2: 5-Pole Array




(b) Mover unit #1: 6-Pole Array

Figure 4.12: Maximum coil current and corresponding number of saturated coils across various stator locations for each mover configuration. Regions where levitation cannot occur due to coil saturation are highlighted in bright yellow in the saturation plots. The center column of plots corresponds to the maximum payload weight as shown in Figure 4.10.

## 4.3 Measurement and Control System

To track the mover unit's position in 3D space, a motion capture system utilizing Vicon Motion Systems' Vantage V5 active infrared cameras is implemented. The marker configuration establishes the mover unit as an object within the Vicon Tracker software, allowing it to be assigned a specific frame of reference. This frame of reference is set to the bottom center of the magnets in the mover unit (see Figure 4.13 for details). The Vicon system then outputs the translational (x, y, z) positions and rotational ($\alpha$, $\beta$, $\gamma$) angles relative to the defined object frame, which are used by the controller.

Reflective markers are placed on each mover unit to define its object frame. These markers are arranged according to the following criteria: each mover unit's marker configuration is distinct to differentiate it from others within the camera's field of view; at least three markers form two perpendicular lines to define an xy-plane; and sufficient markers are used so that even if some become occluded during rotation, at least three others remain visible. These criteria ensure accurate tracking of multiple movers simultaneously while minimizing positional errors.

For the 5-pole mover, an additional step is necessary. The stronger magnets in this unit generate large internal magnetic forces that cause the mover case to deform from a flat slab—resulting in a convex shape with the center as the lowest point of the top surface. To accurately position the object frame at the bottom center of the mover unit, an extra marker is placed at this center point. The origin is then manually shifted downwards to align with the bottom center of the magnet array. After this adjustment, the center marker is removed from the software configuration while retaining the established origin. This method ensures the coordinate system is accurately set, minimizing potential errors if other markers were used instead.

The hardware integration setup is summarized in Figure 4.14. The position data from all four cameras is collated through a power over Ethernet (PoE) switch and then transmitted to a PC over Ethernet. Also known as the Vicon Computer, this PC is where the Vicon Tracker 3.9 software is used to calculate object positions and orientations. This data is then sent to a Beckhoff C6670-0010 industrial server, which functions as the system's programmable logic controller (PLC). A separate PC is used as the engineering workstation for developing control code. The control code is written in two stages: first in MATLAB/Simulink and then in TwinCAT structured text. Any code involving electromagnetic theory is written in MATLAB/Simulink for readability and ease of matrix operations. A few examples of possible calculations include determining the controller outputs, calculating wrench matrices, or performing coil current recalculations. This code

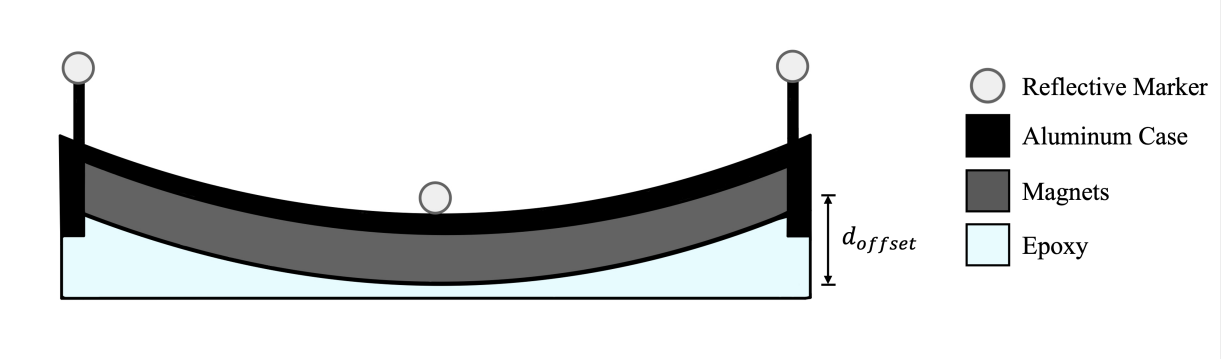



Figure 4.13: Profile view of the 5-pole mover, showing the z-direction offset distance ($d_{offset}$) from the center marker to the desired object reference frame. Note: this drawing is not to scale.

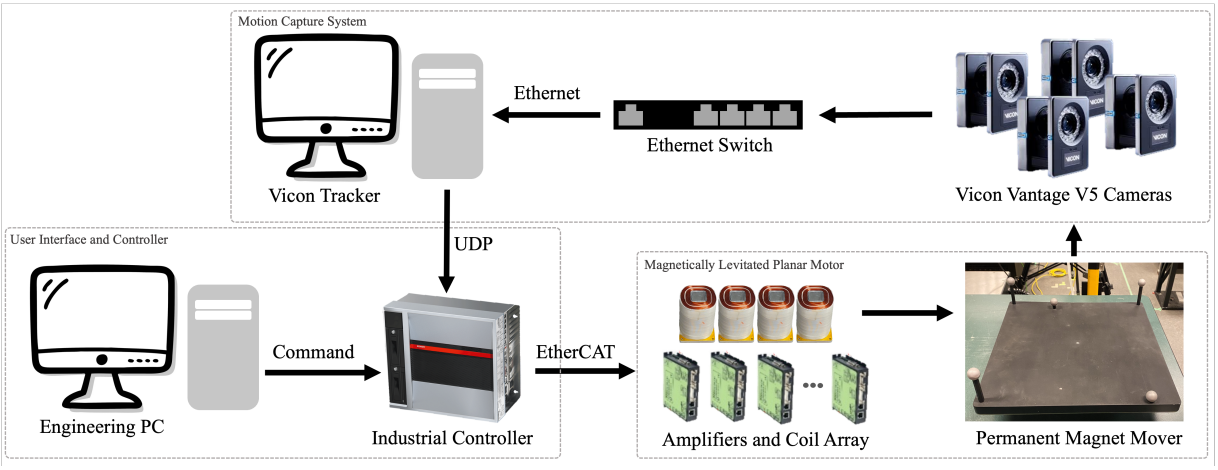



Figure 4.14: Hardware configuration of the TestBench Maglev system.

is then uploaded as a TcCOM object into the TwinCAT environment, where additional structured text programs are written to enhance real-time operation. The TwinCAT program manages the sending and receiving of control signals to enable/disable the current amplifiers and set control targets. It also handles path planning and the loading of any pre-downloaded lookup tables. The current amplifiers control the physical electromagnetic coils that influence the coil array and mover unit system, which is then read by the motion capture system, thereby completing the physical control-plant loop.

# Chapter 5

# Software Design

This section will cover the main software implementations required to conduct the operation of the Maglev platform. Two main programming interfaces exist when designing software for the implementation of the hardware. The magnetic field modeling, conversion to coil currents, and control strategy calculations take place in a MATLAB/Simulink block diagram environment. This is converted into a C++ TwinCAT compiled object and then ported into a structured text industrial PLC programming environment on the runtime PC. Any code related to path planning and management, safety precautions, and operator interfacing is conducted in this framework using TwinCAT 3.1 and Visual Studio 2019. Section 5.1 overviews algorithms related to magnetic field modeling and coil management; Section 5.2 constructs the control strategies implemented; while Section 5.3 highlights other software features to ensure safety and user operability.

## 5.1 Coil and Current Management

### 5.1.1 Active Coil Selection

As the mover unit moves across the stator, the coils that have the most effect are close to the mover unit itself. For simplicity, a coil is considered active if it is within a $18'' \times 18''$ square of the mover center. This activation square is aligned with the mover's (x,y) position and yaw orientation. If the coil's center is located within this square, the coil is considered active, as can be seen in Figure 5.1. The current of the coils outside of this region is set to zero, while the current in the coils within this region will be calculated through the Direct Wrench method described below.

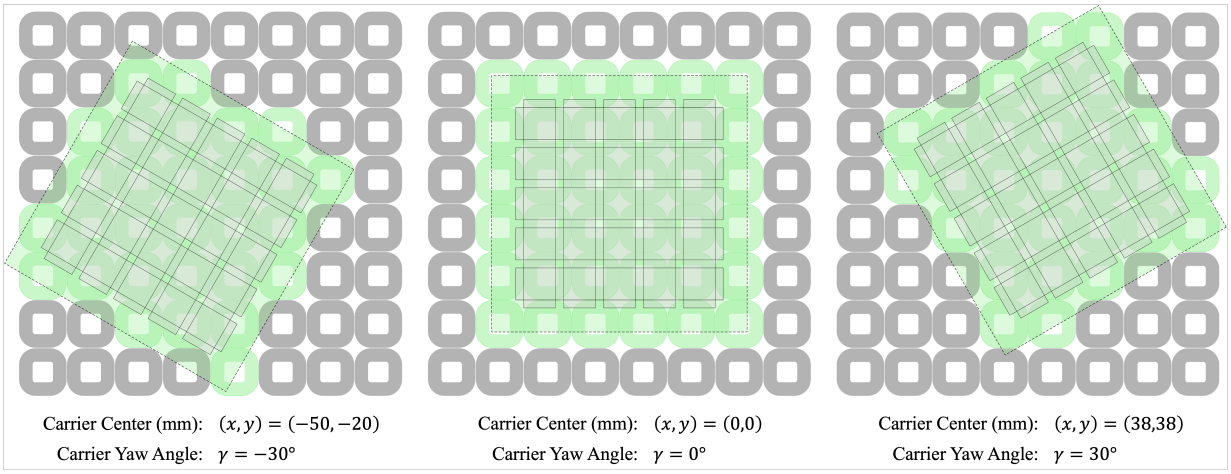



Figure 5.1: Coil activation for various positions and yaw orientations of the mover unit.

### 5.1.2 Direct Wrench Decoupling

The current flowing through the stator electromagnets directly impacts the position and orientation of the mover unit. As such, each DOF of the mover is considered an output of the system, while the current in each coil serves as an input. Because individual coils can independently affect all DOFs of the mover, the system's multiple inputs can simultaneously influence multiple outputs, leading to a cross-coupling effect. Controlling multi-input-multi-output (MIMO) systems like this one is challenging due to the complex interactions between the coils and the forces and torques acting on the mover. To address this challenge, it is essential to decouple the coil inputs from the mover's pose, a method referred to in this research as the direct wrench method.

Consider the forces and torque on the mover, from Equation 3.8. In general, the forces and torques are functions of 3 main variables: the geometric properties of the coil and mover, the relative position between the mover and the coil, and the current running through the coil. For any discrete time step of operation (i.e., every cycle of the control system), the geometric properties of the coil and mover as well as the relative position between them are fixed—it is only the current that is time agnostic and, as well will see, for each fixed position, the force and torque are linear functions with respect to the current. With this in mind, the forces and torques on the mover from *one* coil can be separated as

$$\begin{aligned} \boldsymbol{F} &= -\int_{V_{\text{coil}}} \boldsymbol{J} \times \boldsymbol{B}\,\mathrm{d}V \\ &= -\int_{V_{\text{coil}}} \left(\|J\|\hat{\boldsymbol{J}}\right) \times \boldsymbol{B}\,\mathrm{d}V \\ &= -\|J\| \int_{V_{\text{coil}}} \hat{\boldsymbol{J}} \times \boldsymbol{B}\,\mathrm{d}V \\ &= -\frac{ni}{A} \int_{V_{\text{coil}}} \hat{\boldsymbol{J}} \times \boldsymbol{B}\,\mathrm{d}V \end{aligned} \qquad , \qquad \begin{aligned} \boldsymbol{T} &= -\int_{V_{\text{coil}}} \boldsymbol{r} \times (\boldsymbol{J} \times \boldsymbol{B})\,\mathrm{d}V \\ &= -\int_{V_{\text{coil}}} \boldsymbol{r} \times (\left[\|J\|\hat{\boldsymbol{J}}\right] \times \boldsymbol{B})\,\mathrm{d}V \\ &= -\|J\| \int_{V_{\text{coil}}} \boldsymbol{r} \times (\hat{\boldsymbol{J}} \times \boldsymbol{B})\,\mathrm{d}V \\ &= -\frac{ni}{A} \int_{V_{\text{coil}}} \boldsymbol{r} \times (\hat{\boldsymbol{J}} \times \boldsymbol{B})\,\mathrm{d}V \end{aligned} \tag{5.1}$$

where the magnitude of the current density $\boldsymbol{J}$ is dependent on the number of turns $n$, individual coil current $i$, and the cross-sectional area $A$. Separating terms based on geometric properties and terms based on electrical power produces

$$\boldsymbol{F} = \left(-\frac{n}{A} \int_{V_{\text{coil}}} \hat{\boldsymbol{J}} \times \boldsymbol{B}\,\mathrm{d}V\right) i \qquad \boldsymbol{T} = \left(-\frac{n}{A} \int_{V_{\text{coil}}} \boldsymbol{r} \times (\hat{\boldsymbol{J}} \times \boldsymbol{B})\,\mathrm{d}V\right) i \tag{5.2}$$

$$\boldsymbol{F}(\boldsymbol{r}, i) = \boldsymbol{f}(\boldsymbol{r}) \cdot i \qquad \boldsymbol{T}(\boldsymbol{r}, i) = \boldsymbol{t}(\boldsymbol{r}) \cdot i \tag{5.3}$$

where $\mathbf{r}$ is the mover's position. As seen from Equation 5.3, the force and torque on the mover unit from one coil are linear in coil current. The $\boldsymbol{f}(\boldsymbol{r})$ and $\boldsymbol{t}(\boldsymbol{r})$ terms are functions only concerning the physical geometric properties of the system and are, for every snapshot in time, constant. Using this linear relation, the superposition of forces and torques from all the coils can be recast into matrix form. Given a specific coil $m$, the wrench on the mover is defined as the column vector of forces and torques acting on it. Thus,

$$\boldsymbol{w}_m(\boldsymbol{r}_m, i_m) = \begin{bmatrix} \boldsymbol{F}(\boldsymbol{r}_m, i_m) \\ \boldsymbol{T}(\boldsymbol{r}_m, i_m) \end{bmatrix} = \begin{bmatrix} \boldsymbol{f}(\boldsymbol{r}_m) \cdot i_m \\ \boldsymbol{t}(\boldsymbol{r}_m) \cdot i_m \end{bmatrix} = \begin{bmatrix} \boldsymbol{f}(\boldsymbol{r}_m) \\ \boldsymbol{t}(\boldsymbol{r}_m) \end{bmatrix} i_m = \boldsymbol{\gamma}(\boldsymbol{r}_m) i_m \tag{5.4}$$

where $\boldsymbol{\gamma}(\boldsymbol{r}_m)$ is the wrench per unit current. The total wrench acting on the mover unit is then the sum of these individual wrenches,

$$\boldsymbol{W}_{\text{total}}(\boldsymbol{r}_1, \ldots, \boldsymbol{r}_m, i_1, \ldots, i_m) = \sum_{k=1}^{m} \boldsymbol{w}_k(\boldsymbol{r}_k, i_k) \tag{5.5}$$

$$
\begin{aligned}
&= \sum_{k=1}^{m} \boldsymbol{\gamma}(\boldsymbol{r}_k)\, i_k \\
&= \begin{bmatrix} \boldsymbol{f}(\boldsymbol{r}_1) \\ \boldsymbol{t}(\boldsymbol{r}_1) \end{bmatrix} i_1 + \cdots + \begin{bmatrix} \boldsymbol{f}(\boldsymbol{r}_m) \\ \boldsymbol{t}(\boldsymbol{r}_m) \end{bmatrix} i_m \\
&= \begin{bmatrix} \boldsymbol{f}(\boldsymbol{r}_1) & \boldsymbol{f}(\boldsymbol{r}_2) & \cdots & \boldsymbol{f}(\boldsymbol{r}_m) \\ \boldsymbol{t}(\boldsymbol{r}_1) & \boldsymbol{t}(\boldsymbol{r}_2) & \cdots & \boldsymbol{t}(\boldsymbol{r}_m) \end{bmatrix} \begin{bmatrix} i_1 \\ i_2 \\ \vdots \\ i_m \end{bmatrix}
\end{aligned}
$$

$$
\boldsymbol{W}_{\text{total}}(\boldsymbol{r}_1, \ldots, \boldsymbol{r}_m, \mathbf{I}) = \boldsymbol{\Gamma}(\boldsymbol{r}_1, \ldots, \boldsymbol{r}_m) \cdot \mathbf{I} \tag{5.6}
$$

For a given position of the mover unit, the relationship between the total wrench exerted on the mover and the currents flowing through all coils remains linear. The wrench transformation matrix, denoted as $\boldsymbol{\gamma}$, characterizes the contribution of each coil to the wrench and is constant for a specific pose of the mover. With the mover's location known, the controller can determine the components of $\boldsymbol{\gamma}$ by applying a unitary current to the real-time force and torque method described in Section 3.3.3. Once the desired wrench is specified, the current distribution is obtained by inverting the wrench transformation matrix $\boldsymbol{\gamma}$. Given that the number of active coils exceeds the mover's degrees of freedom during levitation, the system is over-actuated, making $\boldsymbol{\gamma}$ a non-square matrix and generally not invertible. To resolve this, the right Moore–Penrose inverse is employed to solve for the current distribution $\mathbf{I}$, where this pseudo-inverse is given by

$$
\boldsymbol{\Gamma}^{+} = \boldsymbol{\Gamma}^{T}(\boldsymbol{\Gamma}\boldsymbol{\Gamma}^{T})^{-1}. \tag{5.7}
$$

The Moore–Penrose inverse, or simply pseudoinverse, is a solution that minimizes the energy consumption. Thus, a minimum energy solution for the current distribution—which is known as the coil map—can be calculated by

$$
\mathbf{I} = \boldsymbol{\Gamma}^{+}\boldsymbol{W}_{total} = \boldsymbol{\Gamma}^{T}(\boldsymbol{\Gamma}\boldsymbol{\Gamma}^{T})^{-1}\boldsymbol{W}_{total} \tag{5.8}
$$

### 5.1.3 Current Recalculation

Coils positioned closer to the antinodes of the magnetic field generated by the mover unit exert a greater influence. As a result, less current is required to produce a substantial force on the mover in these regions. An energy-minimizing method, such as the Moore-Penrose inverse, is used to calculate the wrench on the mover and will naturally focus the

current distribution in these areas. However, that desired current may exceed the capacity of the power supply, which is rated to provide a maximum of 9 A per coil for up to 8 coils simultaneously, with an additional 1 A buffer for uncertainties. To address this limitation, the current distribution obtained from the pseudoinverse must be adjusted. This involves redistributing the current among non-saturated coils to compensate for those that have reached their maximum capacity. Although this approach no longer minimizes energy usage, it ensures that the desired wrench is achieved.

Initially, the current distribution among the active coils is calculated using Equation 5.8. Let this be the first iteration, and define subsequent iterations by an index $k$. Now define two sets to separate coils that are within the current limit ($N$) and coils that exceed it ($S$) as

$$S = \{s | s \in \mathbb{Z}, 1 \leq s \leq 64, \|i_s\| \geq 9\}\} \tag{5.9}$$

$$N = \{n | n \in \mathbb{Z}, 1 \leq n \leq 64, \|i_n\| < 9\} \tag{5.10}$$

These two sets are mutually exclusive and exhaustive; their union makes up the entire active coil index space. The individual coil contributions in the total wrench on the mover, from Equation 5.5, can then be separated as

$$\begin{aligned} \mathbf{W} &= \begin{bmatrix} \boldsymbol{f}_{n_1} \\ \boldsymbol{t}_{n_1} \end{bmatrix} i_{n_1,k} + \cdots + \begin{bmatrix} \boldsymbol{f}_{n_1} \\ \boldsymbol{t}_{n_1} \end{bmatrix} i_{n_{|N|},k} + \begin{bmatrix} \boldsymbol{f}_{s_1} \\ \boldsymbol{t}_{s_1} \end{bmatrix} i_{s_1,k} + \cdots + \begin{bmatrix} \boldsymbol{f}_{s_1} \\ \boldsymbol{t}_{s_1} \end{bmatrix} i_{s_{|S|},k} \\ &= \begin{bmatrix} \boldsymbol{f}_{n_1} & \cdots & \boldsymbol{f}_{n_{|N|}} \\ \boldsymbol{t}_{n_1} & \cdots & \boldsymbol{t}_{n_{|N|}} \end{bmatrix} \begin{bmatrix} i_{n_1} \\ \vdots \\ i_{n_{|N|}} \end{bmatrix}_k + \begin{bmatrix} \boldsymbol{f}_{s_1} & \cdots & \boldsymbol{f}_{s_{|S|}} \\ \boldsymbol{t}_{s_1} & \cdots & \boldsymbol{t}_{s_{|S|}} \end{bmatrix} \begin{bmatrix} i_{s_1} \\ \vdots \\ i_{s_{|S|}} \end{bmatrix}_k \end{aligned} \tag{5.11}$$

$$\boldsymbol{W} = \boldsymbol{\Gamma}_N \cdot [\mathbf{I}_N]_k + \boldsymbol{\Gamma}_S \cdot [\mathbf{I}_S]_k \tag{5.12}$$

where $[\mathbf{I}_N]_k$ and $[\mathbf{I}_S]_k$ are the coil contributions from coils that are below and above the coil limit, respectively, at the $k$th current recalculation iteration. This equation can be rearranged to find the current distribution among the non-saturated coils.

$$[\mathbf{I}_N]_k = \boldsymbol{\Gamma}_N^+ \left(\mathbf{W} - \boldsymbol{\Gamma}_S \cdot [\mathbf{I}_S]_k\right) \tag{5.13}$$

where $\boldsymbol{\Gamma}_N^+$ is the pseudoinverse discussed in the previous section. Now to begin the second iteration, set the absolute value of the saturated coils to 9A while keeping their respective sign (i.e., if the second coil is saturated, $i_{2,k=1} = -10A$, then the corresponding current at

the next iteration will be $i_{2,k=2} = -9A$). This can be achieved by applying the piecewise function

$$c(x) = \begin{cases} -9 & x < -9 \\ x & -9 \leq x \leq 9 \\ 9 & 9 < x \end{cases} \tag{5.14}$$

to each element of the current distribution that is saturated. Next, subtract this contribution from the desired wrench according to Equation 5.13. Thus,

$$[\mathbf{I}_N]_{k+1} = \mathbf{\Gamma}_N^+ \left(\mathbf{W} - \mathbf{\Gamma}_S \cdot c\left([\mathbf{I}_S]_k\right)\right) \tag{5.15}$$

will produce the new current distribution among the non-saturated coils that would compensate for the magnetic field from the saturated coil. Combining this new distribution with the saturated current distributions forms the new coil map. However, new coils in this current distribution may now be saturated. As such, this recalculation procedure is repeated until the current distribution is no longer saturated or a maximum of 8 coils are saturated, since this is the limit of the power supply. This process is further solidified in Algorithm 1.

**Algorithm 1** Coil current recalculation procedure

**Require:** $\vec{\mathbf{r}}$, $\mathbf{W}$
  $k \leftarrow 1$
  $\mathbf{I}_k \leftarrow \mathbf{\Gamma}^+\mathbf{W}(\mathbf{r})$
  $S = |\mathbf{I}_k| \geq 9$
  **while** sum$(S) \leq 8$ or $k = 10$ **do**
    $k = k + 1$
    $\mathbf{I}_S = c(\mathbf{I}_k(S))$
    $\mathbf{W}_S = \mathbf{\Gamma}(:, S) \cdot \mathbf{I}_S$ ▷ saturated coil wrench contribution
    $\mathbf{W}_N = \mathbf{W} - \mathbf{W}_S$
    $\mathbf{I}_N = \mathbf{\Gamma}^+(:,\ S) \cdot \mathbf{W}_N$ ▷ redistributed coil current among non saturated coils
    $\mathbf{I}_{k+1} = [\mathbf{I}_N; \mathbf{I}_S]$ ▷ combine non-saturated and saturated coil maps
    $S = |\mathbf{I}_{k+1}| \geq 9$
    $\mathbf{I}_k \leftarrow \mathbf{I}_{k+1}$
  **end while**

### 5.1.4 Coil Measurement Adjustment

As introduced previously, the large internal magnetic forces exerted by the magnets in the 5-pole mover caused a concave deformation in the aluminum casing. Consequently, when positioned on the stator's flat surface, the corners of the mover are elevated by up to approximately 3 mm above the coils beneath it. This elevation can lead to inaccuracies in the relative placement of the coils when calculating the contribution of each coil. To address this issue, the surface profile of the mover is determined using linearly interpolated points between measured locations obtained from the motion capture system. The coil height is then adjusted between 0 and 3 mm based on the xy coordinates of the coil center. An ideal visualization of the increased height between the mover and coil due to this curvature is shown below in Figure 5.2.

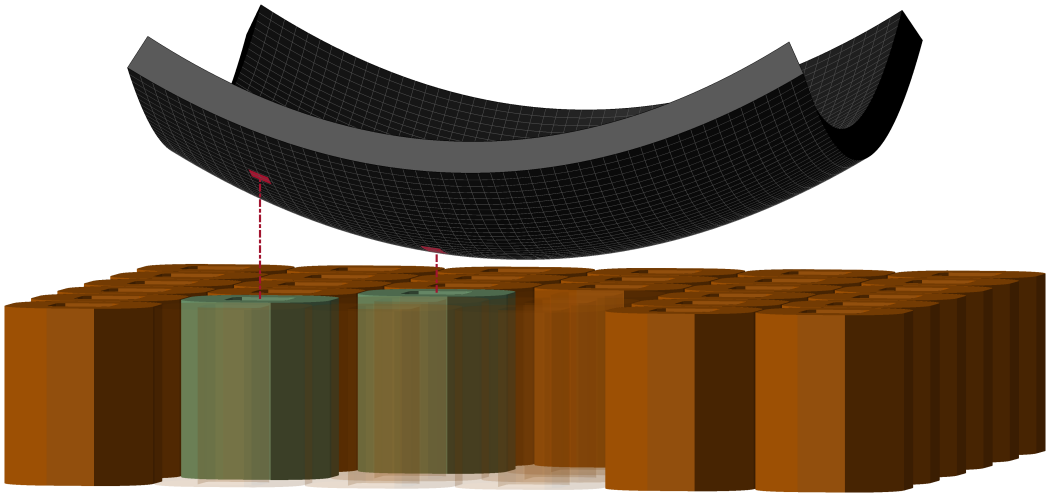


Figure 5.2: Idealized coil height adjustment from a curved mover. Coils of interest are green. Red dotted lines show the difference in z height from the mover and the coil surface. In this illustration, the air gap (i.e., the distance between the center lowest point and the coil surface, is 0.5 mm).

Reflective motion capture markers were placed on the top surface of the mover in an approximately $1'' \times 1''$ grid, with all measurements recorded in the mover's local coordinate frame. These measurements capture the relative vertical displacement, $z_{\text{offset}}(x, y)$, between each point on the surface and the geometric center. The resulting surface profile, shown in Figure 5.3, reflects deviations caused by curvature or assembly imperfections. A linear interpolation scheme—described below—is applied to estimate the $z$-offset between measured points, yielding a continuous height map used in the field compensation model.

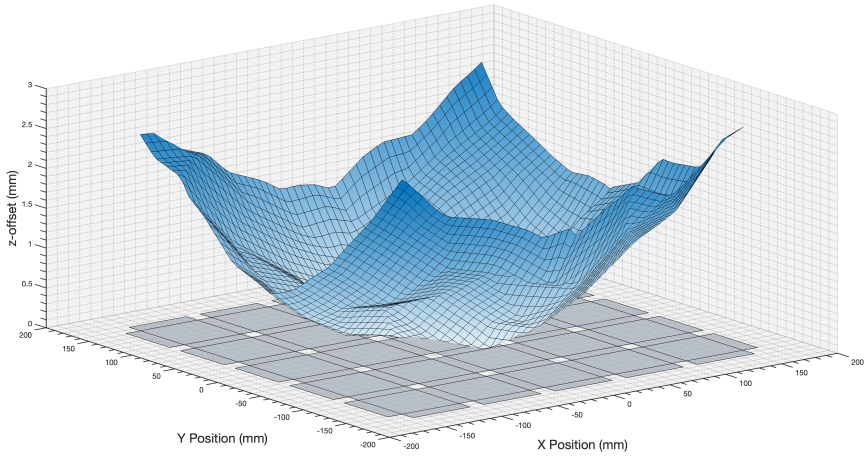



Figure 5.3: Measured curvature profile of the 5-pole Halbach array obtained through experimental mapping. A projection of a flat magnet array is shown below.

Consider a function that approximates this surface function as $z_{offset}(x, y)$ whose domain aligns with the mover. Then, given three distinct points on the surface function, $z_{offset}(x, y)$ can take the form of a plane that is fitted to these three points. As the three points become closer together, the bilinear function $z_{offset}(x, y)$ gives a better approximation to the true surface curvature of the mover. Given the general plane equation

$$z_{offset}(x, y) = Ax + By + C \tag{5.16}$$

and three points $(x_i, y_i, z_{offset,i})$ on the true surface, the unknown coefficients of the plane can be determined through matrix manipulation as

$$\begin{bmatrix} A \\ B \\ C \end{bmatrix} = \begin{bmatrix} x_1 & y_1 & 1 \\ x_2 & y_2 & 1 \\ x_2 & y_2 & 1 \end{bmatrix}^{-1} \begin{bmatrix} z_{offset,1} \\ z_{offset,2} \\ z_{offset,3} \end{bmatrix} \tag{5.17}$$

Since a minimum of three points is required to fully describe the plane approximation, how the points are grouped is crucial in accurately modeling the surface. To group the points into distinct sets of three, a Delaunay triangulation scheme is used. Delaunay triangulation organizes points in a plane such that the circumcircles of the triangles formed do not contain any points. This helps to maximize the smallest angle of the triangles formed and avoid triangles that have very small acute angles, which often lead to numerical errors in the interpolation scheme. Using this criterion, the points from the given data are shown in Figure 5.4. Using these points, the bi-linearly interpolated surface function is shown in Figure 5.3. The maximum offset a coil can have is 3mm.

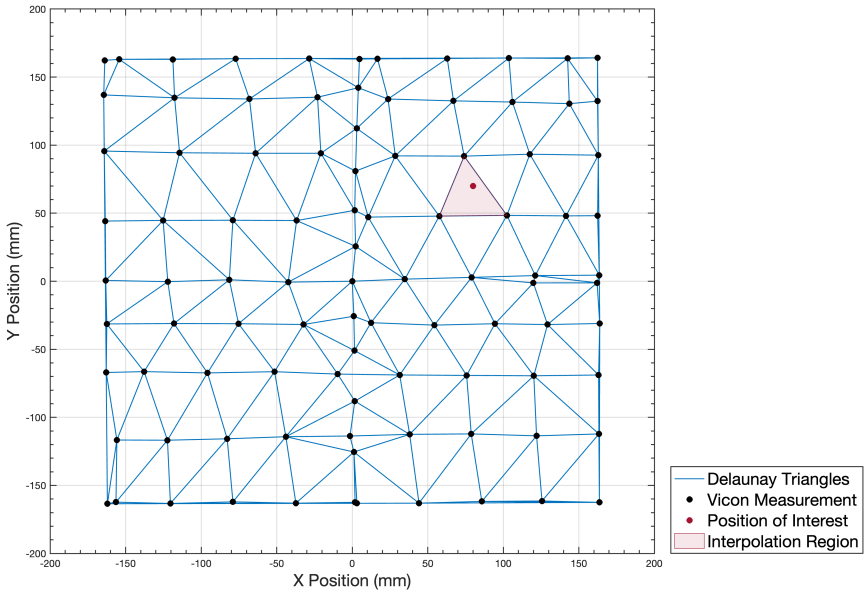



Figure 5.4: Delaunay triangulation of measured surface points for interpolating vertical z-offsets resulting from the 5-pole Halbach array's top-plate curvature.

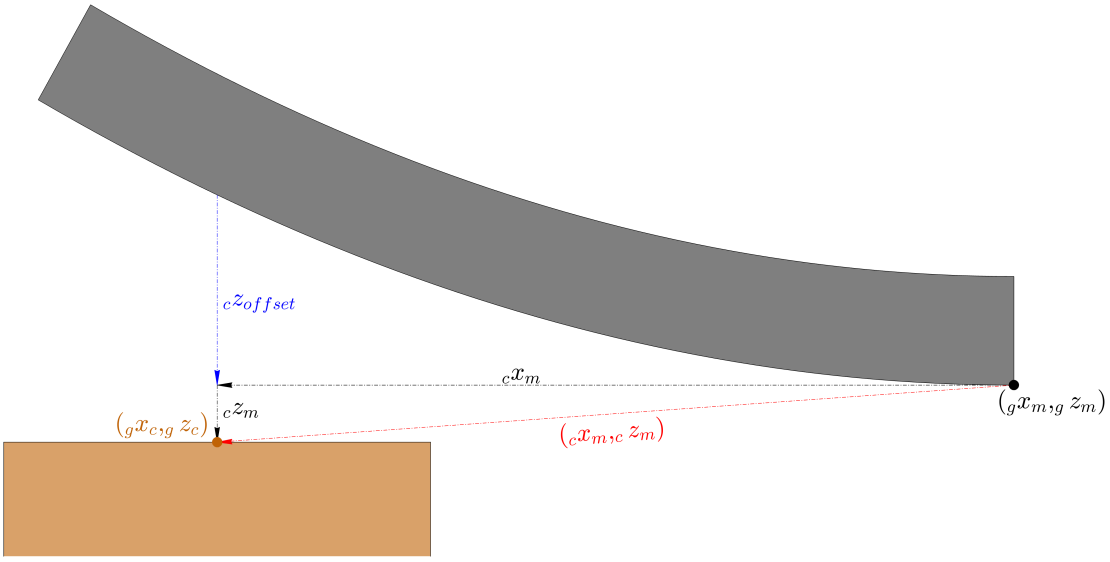



Figure 5.5: Exaggerated side view of the 5-pole Halbach array, illustrating its surface curvature and annotated with relevant geometric quantities.

## 5.2 Control Strategies

### 5.2.1 Derivative Adjustment

Typically, the derivative term adjusts the rate at which the system reaches the desired setpoint, which is crucial for achieving repeatable and precise performance. A common issue arises when the reference variable experiences a sudden change in its setpoint. For example, if the reference signal (in the x direction) jumps from 0 to 10 mm within one frame, the resulting derivative in that frame would be $\frac{10-0}{0.001} = 10,000$ mm/s. Although this command only lasts for one frame, it can saturate the controller output, causing errors in control effort, leading to unnecessary compensation, excessive stress on the system, or even triggering a power supply shutdown.

One common approach to address this is to ignore the change in the reference signal entirely. However, to achieve smooth, long-range motions, the system must be capable of handling ramp or gradually changing reference commands. When the entire change in the reference signal is ignored, the derivative term constantly counters the rest of the controller command, thereby requiring a larger integral term to compensate and potentially introducing unnecessary oscillations. As such, the change in reference is set to zero whenever a step change is detected. A threshold is defined, and the derivative of the reference signal is compared to the derivative of the measured signal and the threshold. If the change in reference exceeds both the threshold and the change in measurement, a step change is detected, and the change in the reference is ignored. The threshold is chosen to prevent coil saturation.

### 5.2.2 Adaptive Control Parameterization

The decoupling between the individual coil currents on the stator and the net forces applied on the mover greatly improves the flexibility in choosing control algorithms for the system. Each axis of motion can be treated as a single-input single-output (SISO) system and can be designed independently of other degrees of freedom. However, in flexible manufacturing applications, being able to load various types of objects without strict prior knowledge can lead to inaccurate system modeling when using conventional model-based control systems, such as a linear quadratic regulator or model predictive controller. This motivates the use of adaptive control strategies, as described in Section 3.4. An ALQR control scheme is used for this research and since each DOF is independent, the following will describe the model identification, parameter identification, and parameter convergence, when applicable, in each direction.

### z-Direction

*System Identification.* The governing equations for the system in the z-direction are given by Newton's second law. Because of the lack of friction present and negligible eddy current damping from the aluminum frame of the stator, the only forces that affect the mover in the z-direction are the applied force from the coil, the force of gravity on the mover, and the force of gravity on the load. The figure below shows the free body diagram describing the situation and the relevant forces acting on the mover and load. Applying Newton's second law to the system, the governing equations become

$$\sum F_z = m_t \frac{\mathrm{d}^2 z}{\mathrm{d}t^2} \tag{5.18}$$

$$F_{app,z} - F_{g,mover} - F_{g,load} = m_t \frac{\mathrm{d}^2 z}{\mathrm{d}t^2} \tag{5.19}$$

$$\frac{\mathrm{d}^2 z}{\mathrm{d}t^2} = \frac{1}{m_t}[F_{app,z} - m_t g] \tag{5.20}$$

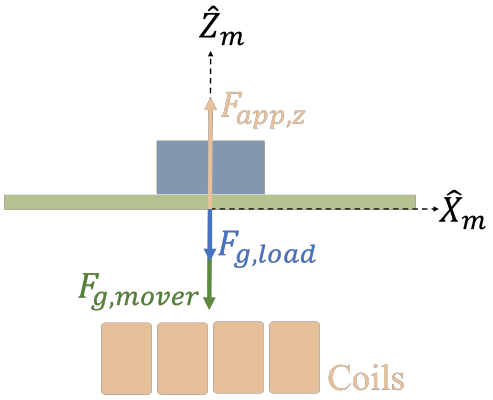



Figure 5.6: Free body diagram of payload center loading. Forces in the z-direction are only shown.

where $m_t = m_{mover} + m_{load}$ and $F_{app,z}$ is the force applied from the coil to the mover as calculated in Section 3.3.3. Defining the modified control input as $\bar{u} = F_{app,z} - m_t g$ and the error of the position is $e = z_d - z$, where $z_d$ is the desired trajectory of the z-position, then the augmented state-space realization of the error system is

$$\frac{d}{dt}\begin{bmatrix} e \\ \dot{e} \\ \int e dt \end{bmatrix} = \begin{bmatrix} 0 & 1 & 0 \\ 0 & 0 & 0 \\ 1 & 0 & 0 \end{bmatrix}\begin{bmatrix} e \\ \dot{e} \\ \int e dt \end{bmatrix} + \begin{bmatrix} 0 \\ -\frac{1}{m_t} \\ 0 \end{bmatrix}\bar{u}. \tag{5.21}$$

with system matrices

$$A = \begin{bmatrix} 0 & 1 & 0 \\ 0 & 0 & 0 \\ 1 & 0 & 0 \end{bmatrix} \quad , \quad B = \begin{bmatrix} 0 \\ -\frac{1}{m_t} \\ 0 \end{bmatrix}. \tag{5.22}$$

*Parameter Identification and Convergence.* The linear SPM of Equation 5.18, using the nomenclature present in Section 3.4, can then be expressed in the following form,

$$\underbrace{F_{app,z} - m_{mover}\left[g + \frac{\mathrm{d}^2 z}{\mathrm{d}t^2}\right]}_{z} = \underbrace{m_{load}}_{\theta_z^*}\underbrace{\left[g + \frac{\mathrm{d}^2 z}{\mathrm{d}t^2}\right]}_{\phi} \tag{5.23}$$

where $z, \phi \in \Re$ consists of the I/O measurements of the system (i.e., $F_{app,z}$ and $\frac{\mathrm{d}^2 z}{\mathrm{d}t^2}$) and $\theta_z^* \in \Re$ is the parameter that is to be estimated. Based on Theorem 3.1, the parameter error will go to zero if the signal $\phi$ is persistently excited. As a reminder, given a certain regressor signal $\phi$, then for a given $T, \alpha_0 > 0$, the signal $\phi$ will be persistently excited if it can satisfy the condition

$$\int_t^{t+T} \frac{\phi(\tau)\phi^T(\tau)}{m_s^2} d\tau \geq \alpha_0 T I \tag{5.24}$$

for some $\alpha_0, T > 0$ and $\forall t \geq 0$. Because an integral of this form is difficult to solve for an arbitrary acceleration, the following discussion will study common cases that are applicable to normal operation.

**Case 1: Stationary Levitation/Constant Velocity** $\left[\frac{\mathrm{d}^2 z}{\mathrm{d}t^2} = 0\right]$. Given that the normalizing signal is chosen as $m_s^2 = \zeta + \eta\phi^T\phi$ for some constants $\zeta, \eta > 0$, the integral on the left hand side becomes

$$\int_t^{t+T} \frac{[0+g]^2}{\zeta + \eta\,[0+g]^2} d\tau = \frac{g^2}{\zeta + \eta g^2}\int_t^{t+T} d\tau = \frac{g^2}{\zeta + \eta g^2} T$$
$$\therefore \frac{g^2}{\zeta + \eta g^2} T \geq \alpha_0 T \longrightarrow \left[\frac{g^2}{\zeta + \eta g^2} - \alpha_0\right] T \geq 0$$

but since $T > 0$ by definition, for this to be true for all time $t$

$$\frac{g^2}{\zeta + \eta g^2} - \alpha_0 \geq 0$$
$$\therefore 0 < \alpha_0 \leq \frac{g^2}{\zeta + \eta g^2} \quad , \quad \forall t > 0. \tag{5.25}$$

As such, the integral in Equation 5.24 is guaranteed to be bounded from below given that the bounding condition $\alpha_0$ is chosen to satisfy Equation 5.25.

**Case 2: Constant Acceleration** $\left[\frac{\mathrm{d}^2 z}{\mathrm{d}t^2} = a_z\right]$. Similar to case one, because there is no time dependence on the integrand of Equation 5.24, the persistence of excitement condition becomes and leads to

$$\frac{(a_z+g)^2}{\zeta+\eta\,(a_z+g)^2}T \geq \alpha_0 T \longrightarrow 0 < \alpha_0 \leq \frac{(a_z+g)^2}{\zeta+\eta\,(a_z+g)^2} \quad , \quad \forall t > 0. \tag{5.26}$$

The only time this condition is not satisfied is if the acceleration in the z-direction is exactly negative of the acceleration due to gravity (i.e., $a_z = -g$), which is only the case when no force is applied from the coils to the mover. This only occurs when the Maglev system is switched off. Therefore, during nominal operation, the case of constant acceleration is guaranteed to be persistently excited.

### Rx/Ry - Direction

*System Identification.* Similarly to before, given the Euler angles $\alpha$ and $\beta$, for rotations around $X_g$ and $Y_g$ respectively, Newton's second law for rotations can be applied to the system to calculate the net torques ($\sum T_i$) about some $i$'th direction. A key difference from the z-direction, however, is the source of the force that interacts with the mover. In the z-axis, the payload mass was treated as internal to the mover unit, so the total mass is the Halbach array mass plus the payload mass, and an external force of gravity applies to both. This guaranteed that the constructed signals would be persistently excited and parameter estimation could be achieved. However, for the torque, the force of gravity does not impart a torque on the Halbach array and payload mass. In order to achieve persistence of excitement of the parameter signals, the force imparted on the Halbach array from the payload mass is treated as external to the mover unit. As we will see, this will lead to the persistence of the excitement condition required for adaptive control. Because of the symmetry of the mover, the details for $T_x$ and $T_y$ are equivalent; thus, only the details for torques about the x-axis, $T_x$, will be shown.

$$\sum T_z = I_{mover}\frac{\mathrm{d}^2\alpha}{\mathrm{d}t^2} \tag{5.27}$$

$$T_{app,x} - T_{load} = I_{mover}\frac{\mathrm{d}^2\alpha}{\mathrm{d}t^2} \tag{5.28}$$

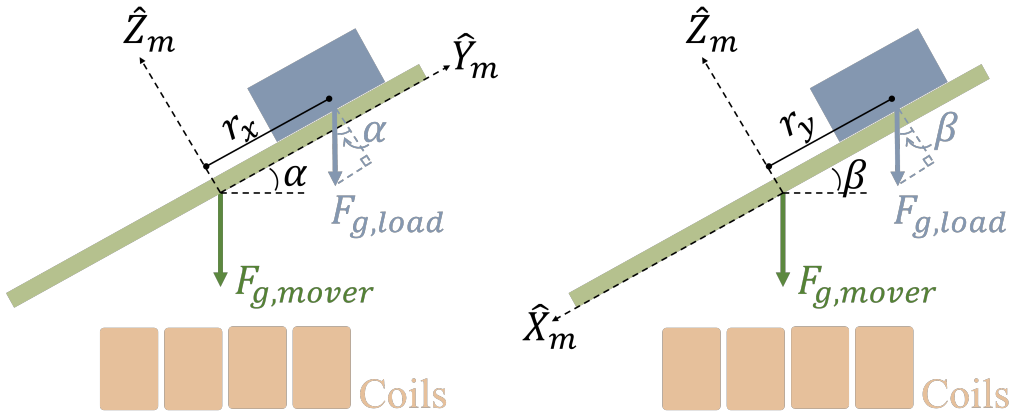



Figure 5.7: Free body diagram of payload offset loading.

$$T_{app,x} - r_x F_{g\perp,load} = I_{mover} \frac{\mathrm{d}^2\alpha}{\mathrm{d}t^2} \tag{5.29}$$

$$T_{app,x} - r_x F_{g,load} \cos\alpha = I_{mover} \frac{\mathrm{d}^2\alpha}{\mathrm{d}t^2} \tag{5.30}$$

where $r_x$ is the perpendicular distance from the center of mass of the payload and the mover frame, as shown in Figure 5.7. Given a small angle approximation, $\alpha < 10^\circ \rightarrow \cos\alpha \approx 1$, the nonlinear system equation can be reduced to a linear one as

$$T_{app,x} - r_x m_{load} g = I_{mover} \frac{\mathrm{d}^2\alpha}{\mathrm{d}t^2} \tag{5.31}$$

$$\frac{\mathrm{d}^2\alpha}{\mathrm{d}t^2} = \frac{1}{I_{mover}} \left[T_{app,x} - r_x m_{load} g\right] \tag{5.32}$$

Defining the modified control input as $\bar{u} = T_{app,x} - r_x m_{load} g$ and the error of the orientation as $e = \alpha_d - \alpha$, where $\alpha_d$ is the desired trajectory of $\alpha$, then the augmented state-space realization of the error system is

$$\frac{d}{dt}\begin{bmatrix} e \\ \dot{e} \\ \int e dt \end{bmatrix} = \begin{bmatrix} 0 & 1 & 0 \\ 0 & 0 & 0 \\ 1 & 0 & 0 \end{bmatrix} \begin{bmatrix} e \\ \dot{e} \\ \int e dt \end{bmatrix} + \begin{bmatrix} 0 \\ -\frac{1}{I_{mover}} \\ 0 \end{bmatrix} \bar{u}. \tag{5.33}$$

with system matrices

$$A = \begin{bmatrix} 0 & 1 & 0 \\ 0 & 0 & 0 \\ 1 & 0 & 0 \end{bmatrix} \quad , \quad B = \begin{bmatrix} 0 \\ -\frac{1}{I_{mover}} \\ 0 \end{bmatrix} \tag{5.34}$$

*Parameter Identification and Convergence.* The linear SPM of Equation 5.31, using the nomenclature present in Section 3.4, can then be expressed in the following form,

$$\underbrace{T_{app,x} - I_{mover}\left[\frac{\mathrm{d}^2\alpha}{\mathrm{d}t^2}\right]}_{z} = \underbrace{r_x m_{load}}_{\theta^*_\alpha} \cdot \underbrace{g}_{\phi} \tag{5.35}$$

where $\theta, \phi \in \Re$ consists of the I/O measurements of the system (i.e., $T_{app,x}$ and $\frac{\mathrm{d}^2\alpha}{\mathrm{d}t^2}$) and $\theta^*_\alpha \in \Re$ is the parameter that is to be estimated. Based on Theorem 3.1, the parameter error will go to zero if the signal $\phi$ is persistently excited. The left-hand side of the persistently excited definition (Equation 5.24) becomes,

$$\begin{aligned}
\text{LHS} &= \int_t^{t+T} \frac{\phi(\tau)\phi^T(\tau)}{m_s^2} d\tau && (5.36)\\
&= \int_t^{t+T} \frac{g^2}{\zeta + \eta g^2} d\tau && (5.37)\\
&= \frac{g^2}{\zeta + \eta g^2} \int_t^{t+T} d\tau && (5.38)\\
&= \frac{g^2}{\zeta + \eta g^2} T && (5.39)
\end{aligned}$$

Just like in the z-direction case, if $\alpha_0$ is chosen to be less than $\frac{g^2}{\zeta+\eta g^2}$, then

$$\int_t^{t+T} \frac{\phi(\tau)\phi^T(\tau)}{m_s^2} d\tau \geq \alpha_0 T \tag{5.40}$$

and the persistence of excitement condition is satisfied.

*Load Location Decoupling.* To make the parameter estimate meaningful and actionable for the end user, it is necessary to decouple it from the mass of the applied payload. Specifically, the estimated parameter $\theta_\alpha$ depends linearly on the applied payload mass. Therefore, to recover an estimate of the payload's spatial offset that is independent of its magnitude of the payload's mass, we normalize $\theta_\alpha$ by the estimated payload mass obtained from the $z$-axis force estimation algorithm.

$$\hat{y}_{load} = \frac{\theta_\alpha}{\hat{m}_{\text{load}} + \varepsilon} \tag{5.41}$$

Here, $\hat{y}_{load}$ is the estimated $y$-location of the payload in the mover's frame of reference, $\hat{m}_{\text{load}}$ is the estimated payload mass from the z-direction, and $\varepsilon$ is a small positive constant added to the denominator to prevent division by zero and mitigate spikes caused by small-magnitude mass estimates. An analogous approach is used for estimating the $x$-location of the payload in the mover's frame of reference (i.e., $\hat{x}_{load}$) using $\theta_\beta$; however, due to the right-handed nature of the mover's reference frame, a negative constant is required

$$\hat{x}_{load} = -\frac{\theta_\beta}{\hat{m}_{\text{load}} + \varepsilon}. \tag{5.42}$$

Because the force due to gravity on the payload is perpendicular to the x- and y-axes, the payload mass does not contribute to the net forces in the x and y directions and does not impart a torque about the z-axis. The persistence of the excitement condition cannot be guaranteed for such $\phi$ signals. As a result, no parameter estimation is considered for these axes—however, the estimated parameters from the previous axes can be utilized to update the mass parameters in the governing equations of the remaining axes. A smoothing factor is also defined to average the parameter estimates over a set number of control frames. Tables 5.1 and 5.2 summarize the LQR tuning parameters used in each axis. The other values of the state penalty matrix $\mathbf{Q}$ are zero to preserve the positive definiteness required for control stability (see Theorem 3.2).

Table 5.1: 6-Pole Halbach ALQR control parameters for each motion axis.

| **Axis** | $\mathbf{Q}_{1,1}$ | $\mathbf{Q}_{2,2}$ | $\mathbf{Q}_{3,3}$ | **R** | $\boldsymbol{\Gamma}$ | $\boldsymbol{\alpha}$ | **Smoothing Factor** |
|---|---|---|---|---|---|---|---|
| $x$ | 9800 | 0.5 | 2300 | 0.0001 | - | - | - |
| $y$ | 9800 | 0.5 | 2300 | 0.0001 | - | - | - |
| $z$ | 11700 | 0.5 | 2300 | 0.0001 | 750 | 150 | 5 |
| $\alpha$ | 2.8 | 0.001 | 16 | 0.0001 | 750 | 150 | 5 |
| $\beta$ | 2.8 | 0.001 | 16 | 0.0001 | 750 | 150 | 5 |
| $\gamma$ | 3.8 | 0.002 | 3.25 | 0.0001 | - | - | - |

Table 5.2: 5-Pole Halbach ALQR control parameters for each motion axis.

| Axis | $\mathbf{Q}_{1,1}$ | $\mathbf{Q}_{2,2}$ | $\mathbf{Q}_{3,3}$ | $\mathbf{R}$ | $\boldsymbol{\Gamma}$ | $\boldsymbol{\alpha}$ | Smoothing Factor |
|---|---|---|---|---|---|---|---|
| $x$ | 51150 | 50 | 40000 | 0.0001 | - | - | - |
| $y$ | 51150 | 50 | 40000 | 0.0001 | - | - | - |
| $z$ | 110000 | 1 | 563000 | 0.0001 | 550 | 175 | 5 |
| $\alpha$ | 9 | 0.01 | 56 | 0.0001 | 550 | 175 | 5 |
| $\beta$ | 9 | 0.01 | 56 | 0.0001 | 550 | 175 | 5 |
| $\gamma$ | 11.5 | 0.01 | 6.3 | 0.0001 | - | - | - |

## 5.3 Other Software Features

### 5.3.1 Calibration and Mass Compensation

The adaptive control scheme developed throughout this work is based on estimating an unknown parameter related to an external payload. For accurate tracking, it is assumed that errors in the construction of the stator, mover, and measurement systems are negligible relative to the uncertainty in the estimated parameter. However, several practical issues challenge this assumption, including camera drift over time, vertical misalignment in the coil stator assembly, and curvature in the top plate of the 5-pole Halbach array, as previously noted. Even during stationary levitation without any applied load, these imperfections can cause the net force and torque imparted by the stator to differ significantly from the true gravitational force acting on the mover. Representative examples of these deviations are summarized in Table 5.3. Such errors can be further amplified when the integral state contributes significantly to the overall control signal.

To mitigate these effects, a built-in calibration routine is employed when no external payload is present. For mass estimation, once the calibration is triggered, 3 s of $F_z$ data is collected during stationary levitation and averaged. Dividing this average force by the gravitational constant yields the practical or "effective" mass of the mover at that location. This calibrated value is then used as the known mover mass, $m_{mover}$, in the parameter identification scheme (see Equation 5.23). A similar correction is applied for torque estimation. In ideal conditions, the applied torques about the $x$ and $y$ axes should be zero when the mover is stationary and unloaded. In practice, however, misalignments and mechanical imperfections result in nonzero $T_x$ and $T_y$. During calibration, the average values of $T_x$ and $T_y$ over a 3 s window are recorded and subsequently subtracted to the

real-time torque values prior to constructing the SPM. This effectively cancels out static offset contributions introduced by construction or integration uncertainties, and can be applied in real-time at any stator location for accurate parameter estimation.

The key advantage of this approach, compared to building a static offset compensation table offline, is that it generalizes to any arbitrary location within the stator's workspace. The calibration procedure can be executed in situ, ensuring more accurate mass and torque estimation even as the system drifts due to temperature changes or long-term sensor drift. This flexibility also enables multiple workstations to operate across different stator regions with consistent estimation accuracy.

Table 5.3: Deviation between calibrated mover mass and torque offset from their true values at representative stator locations.

| | **6-Pole** | | | |
|---|---|---|---|---|
| Mover Location (x, y) mm | Estimated Mass (kg) | True Mass (kg) | Estimated Torque (Nm) | Ideal Torque (Nm) |
| (0, 0) | 7.0277 | 6.800 | -0.0119 | 0 |
| (0, -38) | 7.1082 | 6.800 | 0.0976 | 0 |
| (-38, -38) | 7.0837 | 6.800 | 0.1025 | 0 |
| | **5-Pole** | | | |
| Mover Location (x, y) mm | Estimated Mass (kg) | True Mass (kg) | Estimated Torque (Nm) | Ideal Torque (Nm) |
| (0, 0) | 12.0515 | 11.800 | -0.1860 | 0 |
| (0, -38) | 12.0915 | 11.800 | -0.0735 | 0 |
| (-38, -38) | 12.0396 | 11.800 | 0.0609 | 0 |

To extend this compensation approach to dynamic trajectories, the desired path is first executed without any payload applied. During this run, $F_z$, $T_x$, and $T_y$ are recorded and, in the case of $F_z$, normalized by gravitational acceleration. A moving average filter with a 0.1 s window is applied to smooth out measurement noise. This resulting mass and torque offset profile is stored and reused during actual trajectory execution to pre-compensate the SPM input signals. This dynamic calibration ensures consistent parameter estimation accuracy throughout trajectory operation, even in the presence of system imperfections and sensor drift.

### 5.3.2 End User Upgrades

The user control interface is shown in Figures 5.8-5.9, with several features highlighted to improve the end-user experience:

1. **Live Coil Tracking Map.** This component visualizes which coils are currently active and indicates saturation by changing the coil color to red when excessive current is requested. It also helps users identify mover positions that distribute power more evenly across the stator.

2. **Real-Time Payload Mass and Location Estimation Display.** These values are smoothed for display purposes to provide a stable visual readout. The raw, unsmoothed values are retained in the backend and used by the adaptive control algorithm for accurate parameter updates.

3. **Adaptive Control Toggle and Calibration Button.** A toggle switch allows users to conveniently enable or disable the adaptive control scheme. The calibration button enables accurate force and torque offset estimation at any location on the stator, ensuring consistent parameter identification.

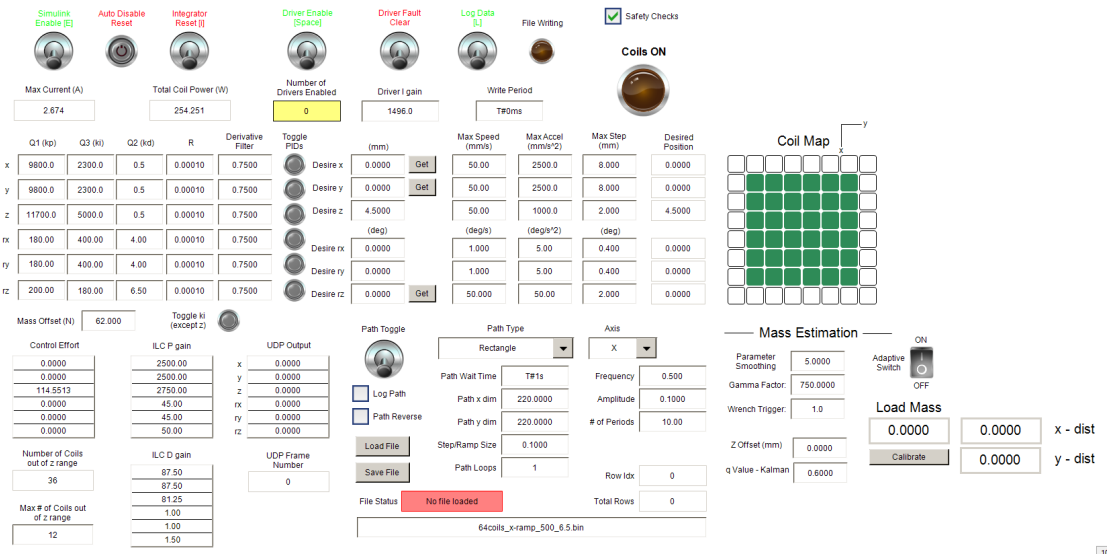



Figure 5.8: Complete user interface for monitoring and controlling the magnetic levitation system.

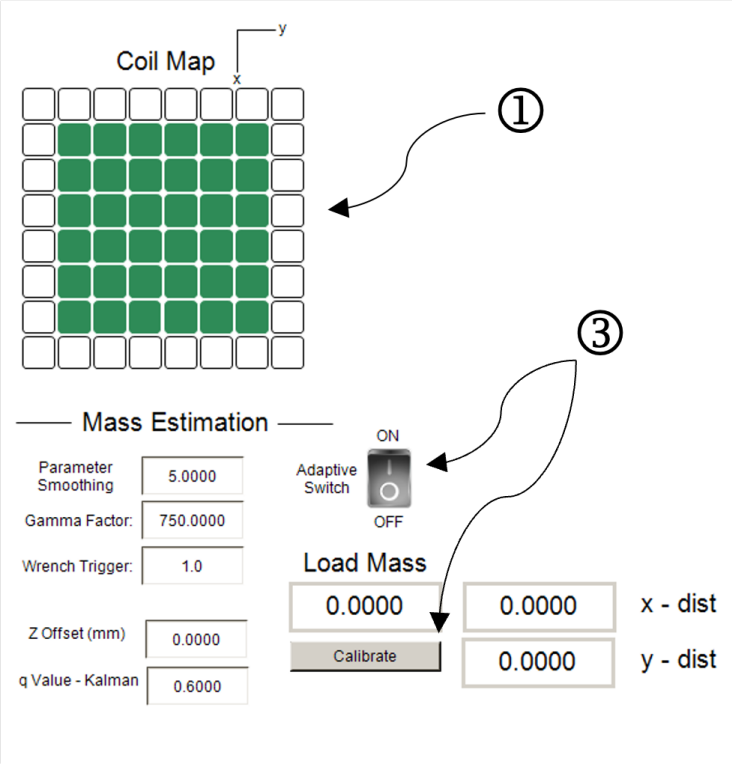



Figure 5.9: Zoomed in view of the user interface illustrating elements that enhance usability and operator interaction.

# Chapter 6

# Results and Discussion

This chapter presents the experimental validation of the adaptive payload estimation and control framework developed throughout this work. The objective of these experiments is to evaluate the performance, robustness, and practical applicability of the proposed parameter estimation scheme under various loading conditions and mover configurations. A series of four experiments were conducted using two magnetically levitated planar movers—one based on a 6-pole Halbach array and the other on a 5-pole design. Each experiment targets a specific operational challenge: Experiment 1 evaluates single mass estimation during stationary levitation; Experiment 2 investigates mass estimation accuracy during sequential mass loading; Experiment 3 focuses on the localization of applied loads across the surface of the mover; and Experiment 4 examines the behavior of the estimator and control signals during dynamic trajectory tracking with mid-path loading and unloading. Together, these experiments demonstrate the feasibility and limitations of real-time payload mass and location estimation in a magnetically levitated environment. Table 6.1 provides a high-level overview of the system's performance, summarizing the average values, absolute errors, and percentage differences across the first three experiments.

## 6.1 Experiment 1: Single Mass Loading

This experiment evaluates the accuracy with which each mover can estimate the mass of a single load applied during stationary levitation. For each mover type, three distinct load masses were selected within the range of achievable stator current. The 6-pole Halbach mover was tested with 0.250 kg, 0.500 kg, and 1.000 kg loads, while the 5-pole Halbach mover was tested with 1.000 kg, 2.013 kg, and 2.264 kg. Experiments were conducted at

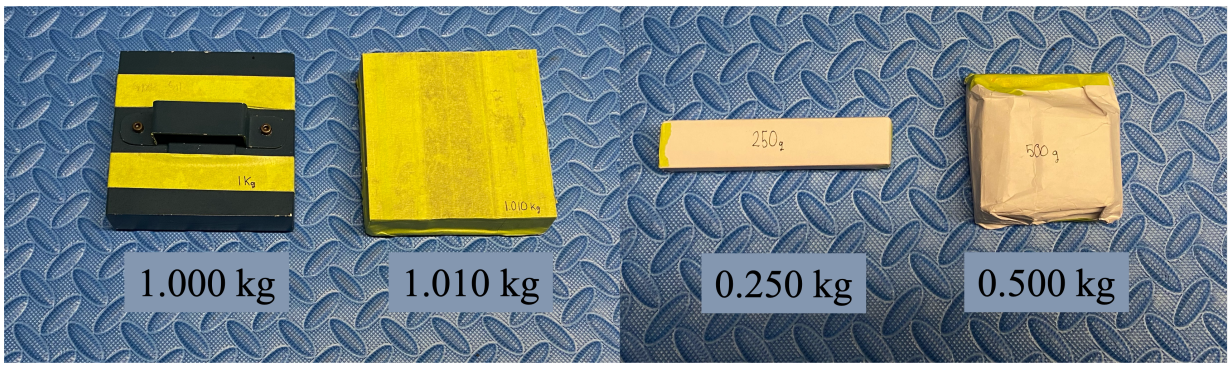



Figure 6.1: Payloads used throughout experiments. They are composed of aluminum. Paint, tape, and paper are used to cover reflective surfaces so as not to interfere with the motion caption system. Masses are constructed and weighed using a 1g precision scale.

three distinct levitation positions: (1) with the mover centered above a single coil, (2) centered between two adjacent coils, and (3) centered between four adjacent coils.

The loading procedure for each trial was as follows: the mover was first levitated at the desired location and held stationary during a 3 s calibration period. It was then kept hovering for at least 3 s before a load was gently placed at the center of the mover. After allowing the system to stabilize for a minimum of 5 s, the load was removed, followed by a final stabilization period of at least 3 s. This procedure was repeated at least three times per levitation location. The best trial from each location is summarized in Figure 6.3 for the 6-pole mover and Figure 6.4 for the 5-pole mover.

For the 6-pole Halbach configuration, the lowest MAPE occurred when the mover was centered above four coils, yielding a MAPE of 3.2% and an absolute error of 16 g. The four-sigma standard deviation across trials was approximately 10 g. The average convergence rate was $1.75\,\mathrm{kg\,s^{-1}}$, with the system reaching steady state in approximately 1 s.

In contrast, the best performance for the 5-pole Halbach configuration was observed when the mover was centered above a single coil, achieving a MAPE of 0.6% and an absolute error of 11 g. The four-sigma standard deviation was approximately 13 g, and the average convergence rate was $5.0\,\mathrm{kg\,s^{-1}}$, with a settling time of approximately 1.5 s.

When averaged across all loading masses and locations, the 5-pole Halbach achieved a reduction of approximately 2.75% in estimation error compared to the 6-pole Halbach. The average absolute error for the 6-pole mover was 20.7 g, whereas the 5-pole mover reduced this to 12.6 g. The average $1\sigma$ standard deviation for the 6-pole mover was 2.3 g, while the 5-pole mover exhibited a slightly higher value of 3.4 g. Considering a $4\sigma$ confidence interval,



Figure 6.2: Example of center loading on the 6-pole Halbach mover, levitated at a height of 6 mm.

the 5-pole array can resolve a minimum change in payload mass of approximately 15 g, compared to 10 g for the 6-pole array. This increased sensitivity of the 6-pole configuration is expected, as its lower load capacity amplifies the relative impact of small changes in vertical force.

Interestingly, the 6-pole mover performed best when centered above four coils, while the 5-pole mover yielded the most accurate results when centered above a single coil. This difference is likely due to the magnetic geometry of each array. In the 5-pole mover, the central magnet is aligned directly above a coil, allowing the resulting force to act in the strongest region of the magnetic field. In the 6-pole mover, the central region of the array contains no magnet; however, when centered above four coils, the surrounding magnets are better aligned with the underlying stator coils. This improves symmetry and concentrates force generation in the stronger magnetic zones. Conversely, when the mover is positioned above weaker regions of the array, force generation is distributed over a larger area and becomes more susceptible to magnetic modeling errors.

Notably, during the loading and unloading phases, the 5-pole mover exhibited significant overshoot in the estimated payload mass. This was largely attributed to the manual loading procedure: introducing a hand into the Vicon tracking scene interferes with the marker visibility. Since the 6-pole mover uses more tracking markers, it is less sensitive to partial

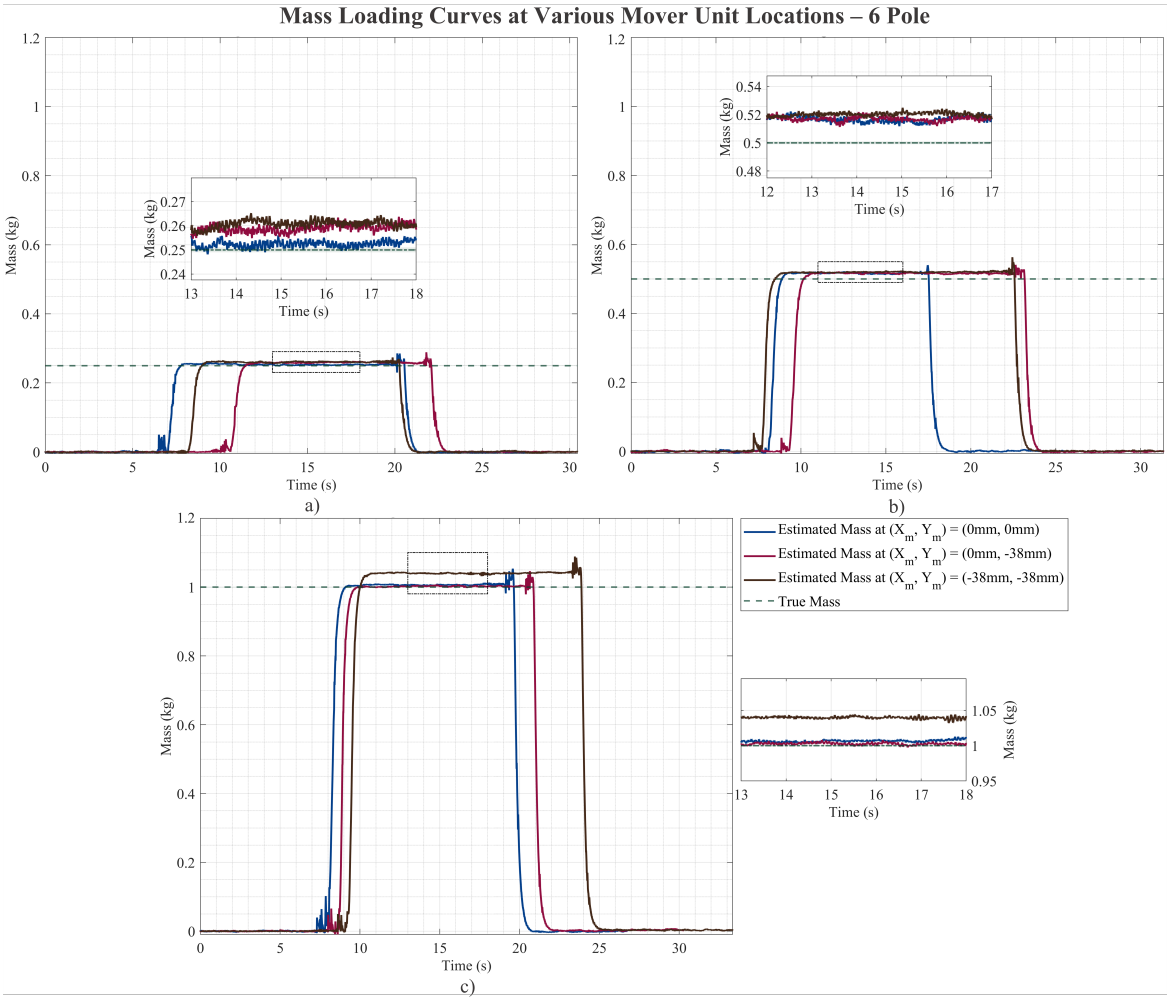



Figure 6.3: Summary of mass loading performance at three stator locations for the 6-pole Halbach mover. The zoomed-in region highlights the response within the boxed area. Note that the initial and final loading times were not held constant between trials.

occlusion, though this comes at the cost of reduced available space for placing the payload. Despite these disturbances, the adaptive estimator rapidly recovers after the occlusion is removed. From the onset of camera interference to within 5 % of the steady state response, the average settling time was approximately 2.5 s for the 5-pole array and 1.75 s for the 6-pole array.

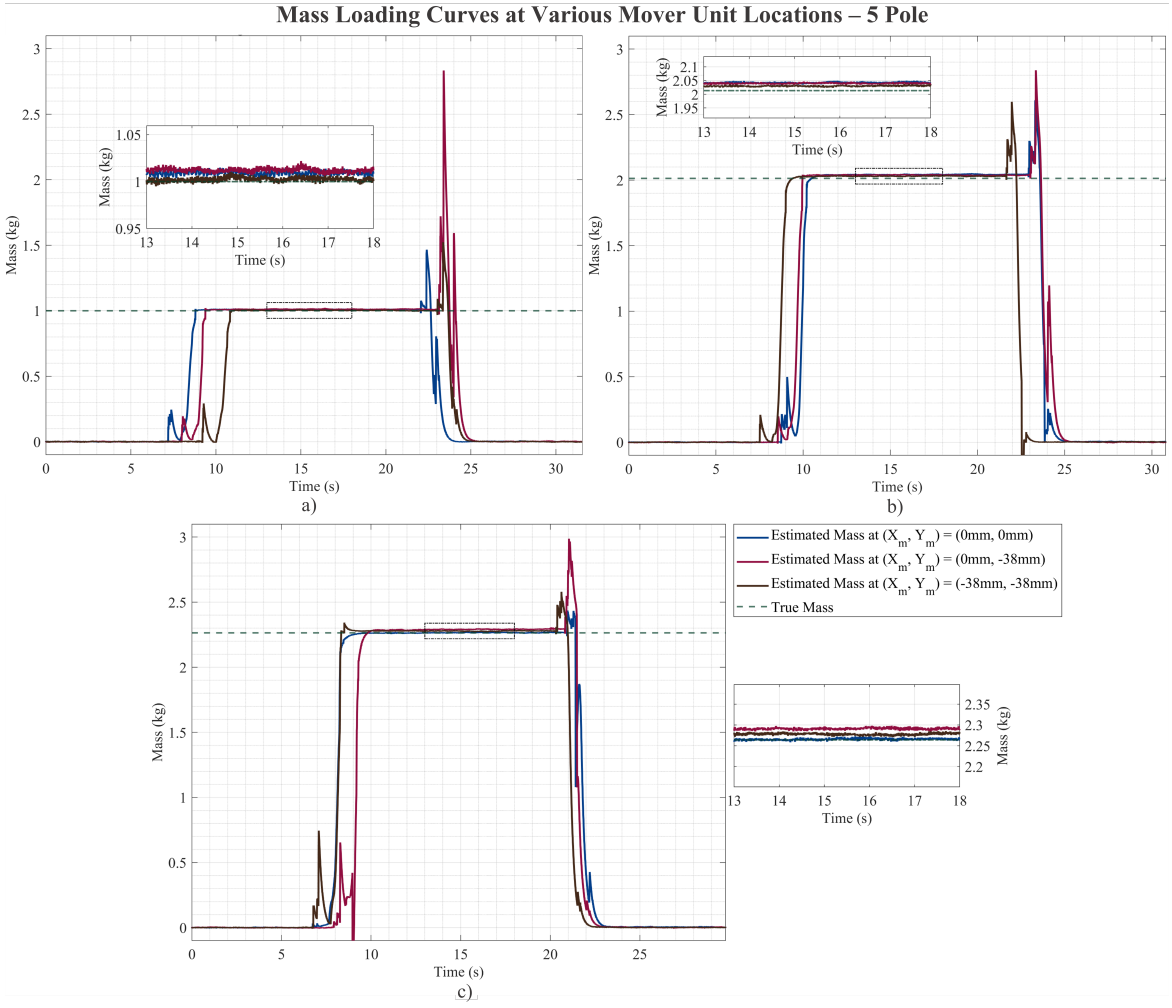



Figure 6.4: Summary of mass loading performance at three stator locations for the 5-pole Halbach mover. The zoomed-in region highlights the response within the boxed area. Note that the initial and final loading times were not held constant between trials.

## 6.2 Experiment 2: Sequential Mass Loading

This experiment aims to assess the accuracy with which each mover can estimate the total loading mass applied when multiple payloads are applied successively. For each mover unit, at least two distinct payload masses were selected where the total is within the range of achievable stator current. The 6-pole Halbach mover was loaded with masses of 0.250 kg, 0.500 kg, and 0.250 kg, in that order respectively; the 5-pole Halbach mover was successively loaded with 1.010 kg, 1.000 kg, 0.250 kg, and 0.250 kg. Experiments were conducted at three distinct mover positions: (1) with the mover centered above a single coil, (2) centered between two adjacent coils, and (3) centered above four adjacent coils.

The loading procedure for each trial was as follows: the mover was first levitated at the desired location and held stationary while undergoing a 3 s calibration period. It was then kept hovering for a minimum of 3 s before a load was gently placed at the center of the mover. After allowing the system to stabilize for at least 2 s, the next load is applied as close to the center as possible, this is repeated until all the loads are used and then followed by a final stabilization period of at least 3 s. This procedure was repeated a minimum of three times for each levitation location. The best result from each location is summarized in Figure 6.5 for the 6-pole mover and Figure 6.6 for the 5-pole mover. The plots corresponding to the other mover locations are located in Appendix A.2.

Similar to the previous experiment, the lowest MAPE for the 6-Pole Halbach occurred when the mover was centered above four coils, yielding an average MAPE of 1.9% and an absolute error of 12 g. The four-sigma standard deviation across trials was approximately 9 g. The average convergence rate was $0.9\,\mathrm{kg\,s^{-1}}$, with the system reaching steady state in approximately 1.3 s.

In contrast, the best performance for the 5-pole Halbach configuration was observed when the mover was centered above a single coil, achieving a MAPE of 1.1% and an absolute error of 22 g. The four-sigma standard deviation was approximately 12 g, and the average convergence rate was $2.3\,\mathrm{kg\,s^{-1}}$, with a settling time of approximately 2.1 s.

The results demonstrate that both mover configurations are capable of accurately tracking incremental changes in load mass, even when applied in rapid succession. In general, the estimated mass trajectories closely follow the expected staircase profile corresponding to each added load. After each loading event, the system exhibits a clear transient period, but returns to steady-state estimates within approximately 2 s in most cases. However, the 6-pole Halbach mover showed a tendency to slightly overestimate intermediate mass values, particularly during the second and third loading steps. This behaviour is likely due to its lower load-carrying limit, which makes it more sensitive to transient disturbances

and estimation noise, especially when operating near its maximum supported mass.

Across all mover positions and steps, the mean absolute percentage error and absolute error were approximately 2.5% and 15 g for the 6-pole array, and 1.5% and 30 g for the 5-pole array. This suggests that while the 6-pole configuration is more accurate in absolute terms for lighter loads, the 5-pole configuration offers better relative consistency across a broader loading range.

A significant challenge in this experiment emerges when the load mass has a large physical footprint, as this increases the likelihood of occluding the tracking markers and introduces greater sensitivity to placement errors. In other words, stacking multiple weights reduces the visibility of Vicon markers on the mover. As in Experiment 1, each time a load is added, the operator's hand or the payload itself may occlude markers, introducing transient disturbances in the tracking data. These artifacts are particularly disruptive in configurations with fewer markers, as observed in some 5-pole trials. Nevertheless, the adaptive estimator proved robust, typically recovering within 1.5 to 2.5 s, depending on the mover's position and payload size.

Importantly, the cumulative error over subsequent payload additions remained approximately linear, as indicated by Table 6.1. This suggests that the adaptive estimation does not drift over the loading progression. When averaged over all evaluated stator locations, the absolute difference between the ideal and observed total payload mass positioned on the 5-pole array increased by approximately 1.5 g to 2 g per 100 g of applied mass. The MAPE remained steady at around 1.5% throughout the entire loading procedure. Looking at the 6-pole mover array, the scaling of the absolute difference increased slightly at approximately 2 g to 3 g per 100 g, with an overall MAPE of roughly 2.5%. However, the MAPE remained steady throughout the loading procedure, only varying by less than half a percent in no consistent direction. For both movers, the absolute error compounded throughout the progression of the loading, but consistently fluctuated within a narrow range of 0.5 percentage points. While this performance exceeds that of some previous magnetic suspension balances (see Section 2.4 for a discussion on MSBs), the distinction between how the absolute error and percent error scale may be important depending on the fidelity required in the machining or conveying applications.

The successful sequential loading capabilities of this system are a critical feature for real-world applications. Tools, parts, or other components may be added or removed during operation, so the ability to account for these variations enhances overall system performance. Future improvements could include the display of real-time confidence intervals or stepwise MAPE calculations to give operators immediate feedback on estimation reliability. In addition, implementing a "staged loading mode" with user-guided timing

or visual prompts could reduce user-induced variability and improve the repeatability of results across various stator locations.

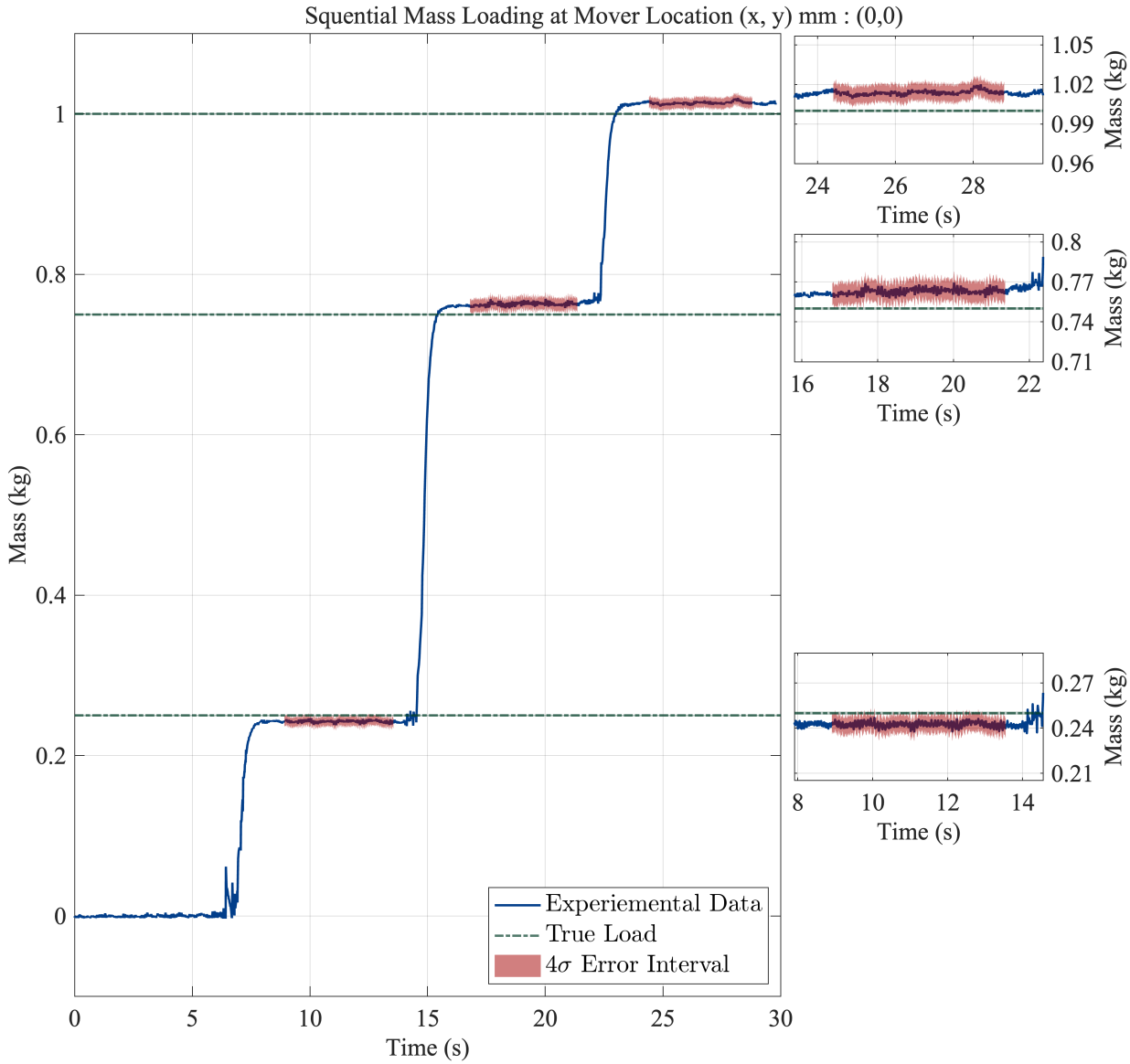



Figure 6.5: Summary of successive mass loading performance when the 6-Pole Halbach is between 4 coils. The zoomed-in region highlights the response within the boxed area. Note that the exact loading times between trials were not held constant.

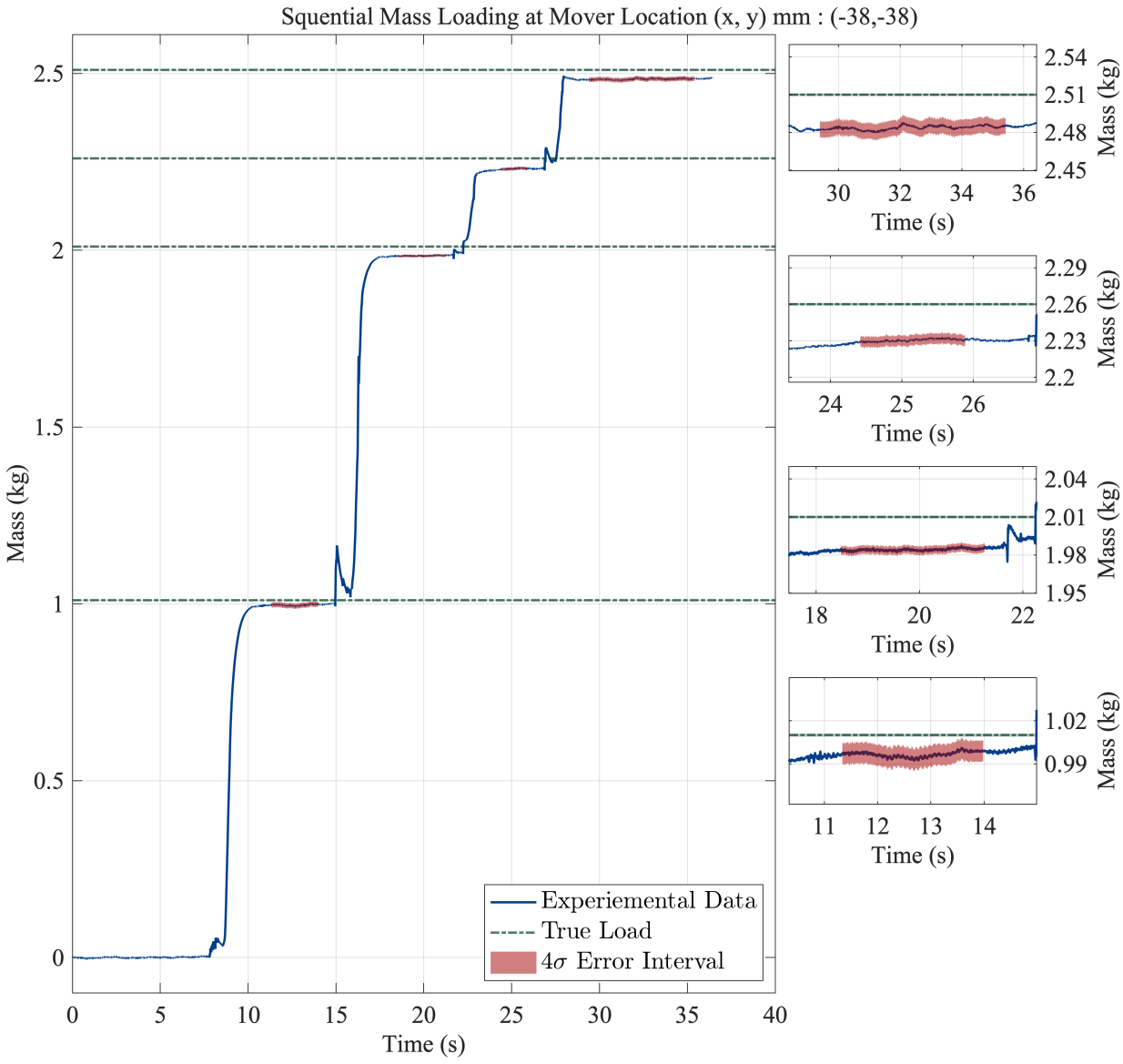



Figure 6.6: Summary of successive mass loading performance when the 5-Pole Halbach is above a single coil. The zoomed-in region highlights the response within the boxed area. Note that the exact loading times between trials were not held constant.

## 6.3 Experiment 3: Offset Mass Loading

This experiment aims to assess the accuracy with which each mover can estimate the location of an applied payload placed on top of the mover. For each mover unit, at least seven distinct loading positions were identified and marked. At each location, a plastic square spacer with a side length of approximately 3.6 cm (3 cm for the 6-pole mover) was affixed at the center to help constrain the center of mass of the applied payload within a well-defined region. During each trial, the payload was carefully placed onto the square to concentrate the loading effect within the spacer's boundary. The mass of the payload used during the 6-Pole array experiment was 0.25kg and 1kg for the 5-Pole experiments.

The loading procedure was as follows: the mover was first levitated at the desired location and held stationary during a 3 s calibration period. It was then kept hovering for a minimum of 3 s before the load was gently placed on the square spacer. After allowing the system to stabilize for at least 5 s, the load was removed, followed by a final stabilization period of at least 3 s. This procedure was repeated a minimum of three times for each levitation location before moving the spacer to a new location.

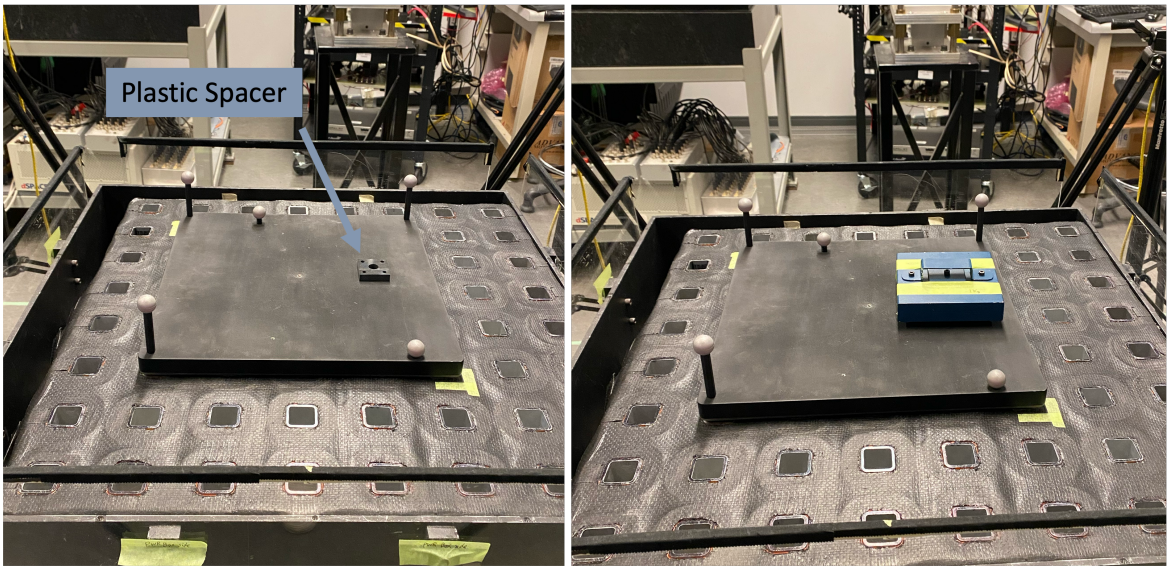



Figure 6.7: Example of side loading on the 5-pole Halbach mover, levitated at a height of 7 mm. A plastic spacer is used to constrain the load's center of mass within a smaller, well-defined area.

A summary of the various payload loading positions tested for the 6-pole Halbach array, and the corresponding estimates from the algorithm, is shown in Figure 6.8; detailed parameter estimates for a selected loading location are shown in Figure 6.9. Figures 6.10 and 6.11 present the corresponding results for the 5-pole Halbach array.

For the 5-pole Halbach array, the average absolute error in the estimated $x$-location of the applied load is 1.2 cm, with a standard deviation of 1.0 cm. In the $y$-direction, the average absolute error increases to 2.1 cm, with a larger standard deviation of 2.3 cm. The average absolute error in the estimated load mass is approximately 36 g. This is slightly higher than the payload mass estimate from the single-mass loading experiments. In contrast, the 6-pole Halbach array shows significantly improved performance: the average absolute error in the $x$-location is only 0.50 cm with a standard deviation of 0.25 cm, while the average absolute error in the $y$-location is 0.41 cm with a standard deviation of 0.15 cm. The corresponding average absolute error in mass estimation is 11 g with a standard deviation of 1.5 g, which is consistent with the single-mass loading experiments.

A key factor contributing to the discrepancy between the two systems is likely the curvature of the top plate on the 5-pole mover. As illustrated in Figure 6.10, estimation accuracy degrades significantly as the payload position moves toward the outer edges of the mover. The standard deviation in these peripheral locations increases substantially, indicating less reliable parameter estimation. Conversely, when the load is placed closer to the center of the mover, the confidence intervals are smaller, suggesting more stable and accurate results. On the other hand, this effect is not observable with the loading results from the 6-pole mover. The standard deviations across the payload's various loading locations remain fairly constant.

The error in location estimation is further influenced by the mover's position relative to the underlying coils. When the 5-pole mover is centered above four coils, the average position error is less than 1 cm. However, when it is centered above a single coil, the absolute position error can exceed 3 cm. A possible explanation is that, when the mover is centered between four coils, the edges of the Halbach array are directly above coil centers. Since torque generation is most effective in these regions, payload applications near the mover's edge are better supported by the actuator field, resulting in more accurate parameter estimation. In contrast, when the mover is centered above a single coil, the payload-induced torques must be balanced by coils farther from the payload's position, amplifying the impact of modeling inaccuracies, especially in a system with structural curvature like the 5-pole array. This effect is noticeable, but slightly more muted for the 6-pole array—the average absolute error in payload location when the mover is above one coil is 0.45 cm while the error is 0.5 cm when above four coils.

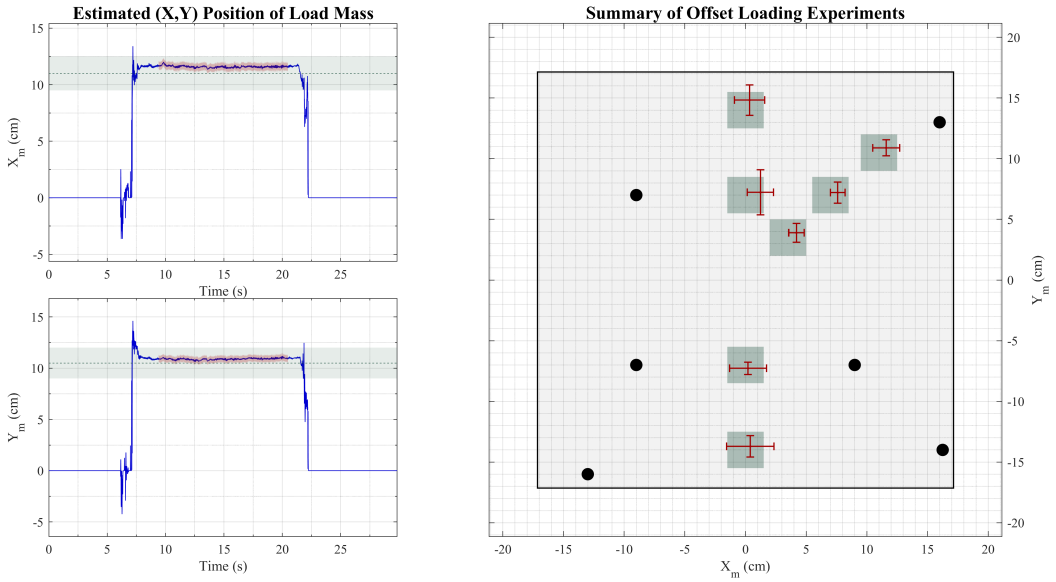



Figure 6.8: Summary of loading location estimates for the 6-pole Halbach mover. The green boundary represents the acceptable error region around the true loading location, while red error bars indicate the $3\sigma$ standard deviation of the estimated positions. Results are averaged over each mover location. Black circles represent the Vicon marker and the shaded gray region denotes the boundary of the mover.

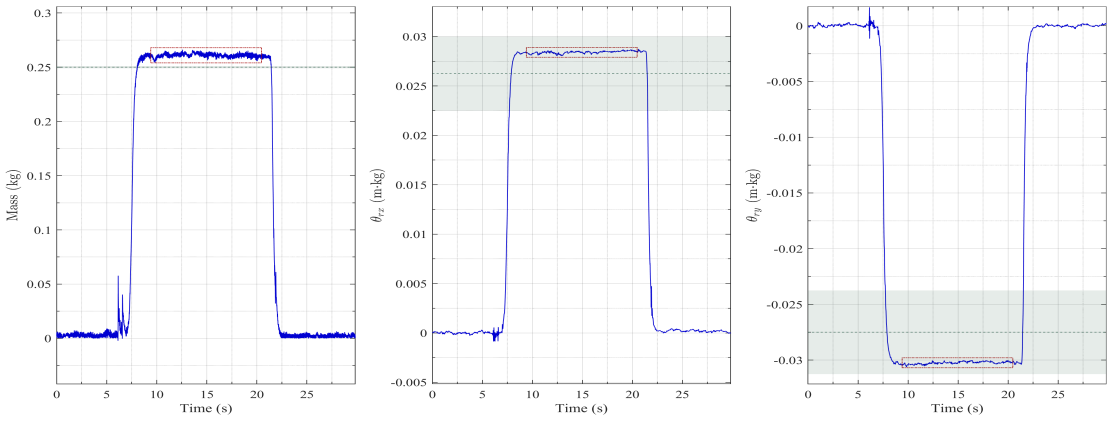



Figure 6.9: Direct parameter estimate curves at loading location (11 cm, 10.5 cm) for the 6-pole Halbach array. The green boundary shows the error interval for the true loading location, while the red box denotes the steady state region.

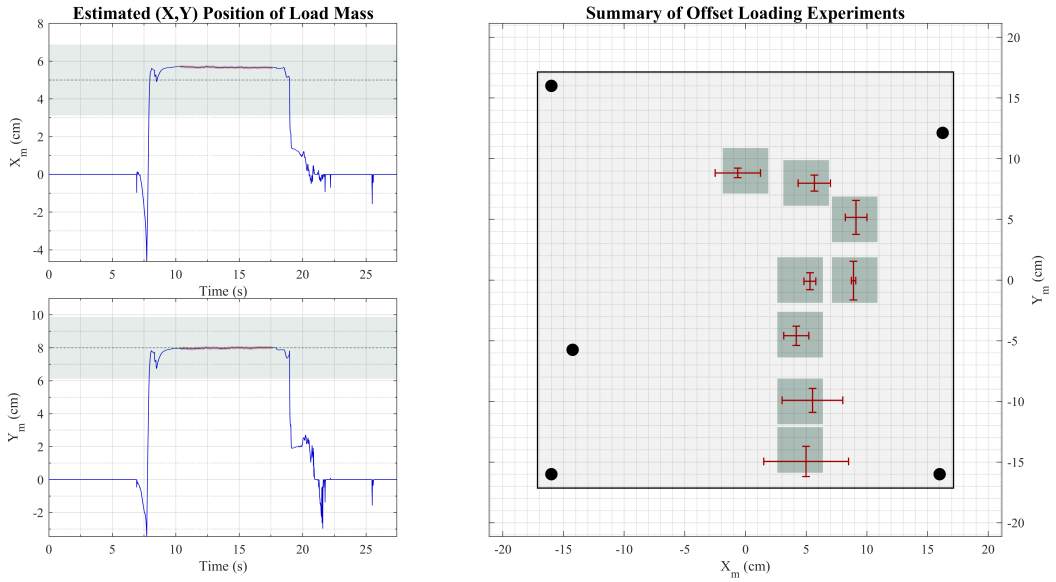



Figure 6.10: Summary of loading location estimates for the 5-pole Halbach mover. The green boundary represents the acceptable error region around the true loading location, while red error bars indicate the $1\sigma$ standard deviation of the estimated positions. Results are averaged over each mover location. Black circles represent the Vicon markers and the shaded gray region denotes the boundary of the mover.

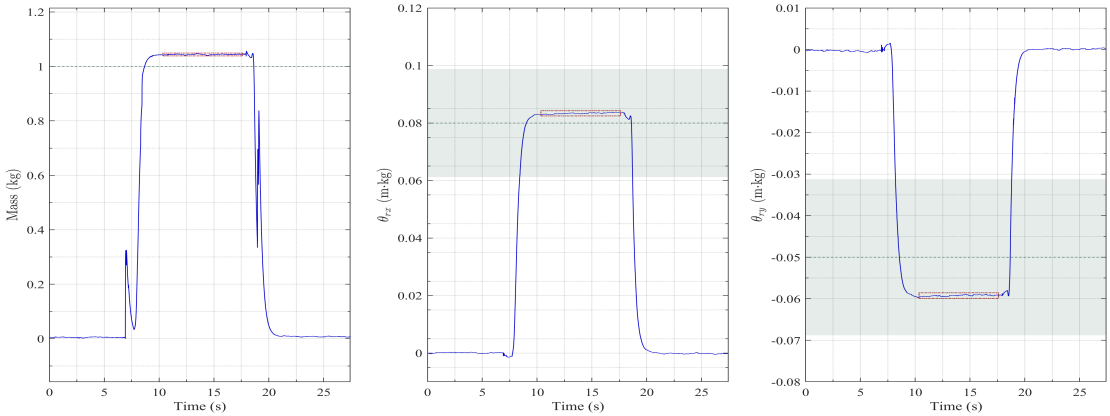



Figure 6.11: Direct parameter estimate curves at loading location (5.0 cm, 8.0 cm) for the 5-pole Halbach array. The green boundary shows the error interval for the true loading location, while the red box denotes the steady state region.

## 6.4 Experiment 4: Mass Loading During Trajectory Tracking

This experiment evaluates how the system responds to load mass changes during dynamic motion. Specifically, it investigates the performance of the mass estimation algorithm and its influence on the control signals when a load is introduced and removed mid-trajectory.

In this test, the mover follows a square trajectory around the stator starting with no external payload. Partway through the trajectory, a known load mass is gently placed on the mover. Before the trajectory is completed, the payload is removed. This sequence allows assessment of how quickly and accurately the estimator responds to sudden changes in payload under dynamic conditions. The following figures illustrate the trajectory tracking response, the real-time mass estimate, and the corresponding behaviour of the control signals throughout the loading and unloading events.

Referring to Figure 6.14, prior to applying any mass compensation, the error in the estimated payload mass can reach as high as 25%. After incorporating the mass compensation profile shown in Figure 6.12, the maximum steady-state error is reduced by approximately a factor of 9, to around 3% (Figure 6.14). Upon application of the load, the parameter estimate converges in approximately 1.4 s, with a maximum convergence rate of $2.6\,\mathrm{kg\,s^{-1}}$. When the load is removed, a similar convergence rate of $2.8\,\mathrm{kg\,s^{-1}}$ is observed.

Examining the dynamic response curves in Figure 6.13, the most pronounced difference is seen in the vertical ($z$) direction following load application. The non-adaptive LQR controller takes nearly 5 s to recover and track the reference trajectory, whereas the ALQR maintains comparable performance to its nominal case with no load present. A similar trend is observed in the yaw response: the standard LQR controller exhibits increased oscillation amplitude, while the ALQR effectively suppresses oscillations and maintains trajectory tracking performance despite the external disturbance.

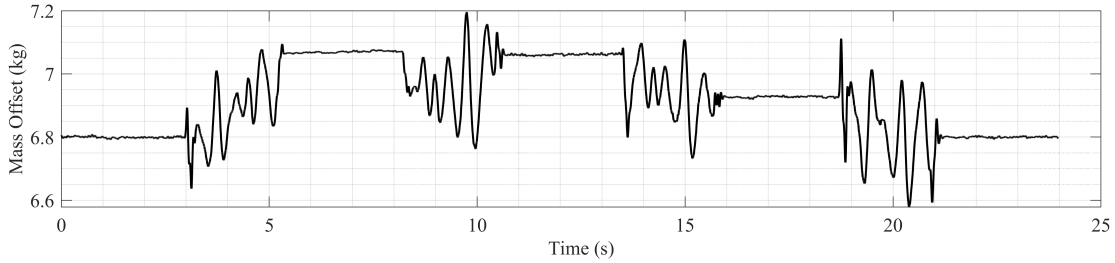



Figure 6.12: Mass offsetting profile for a rectangle trajectory

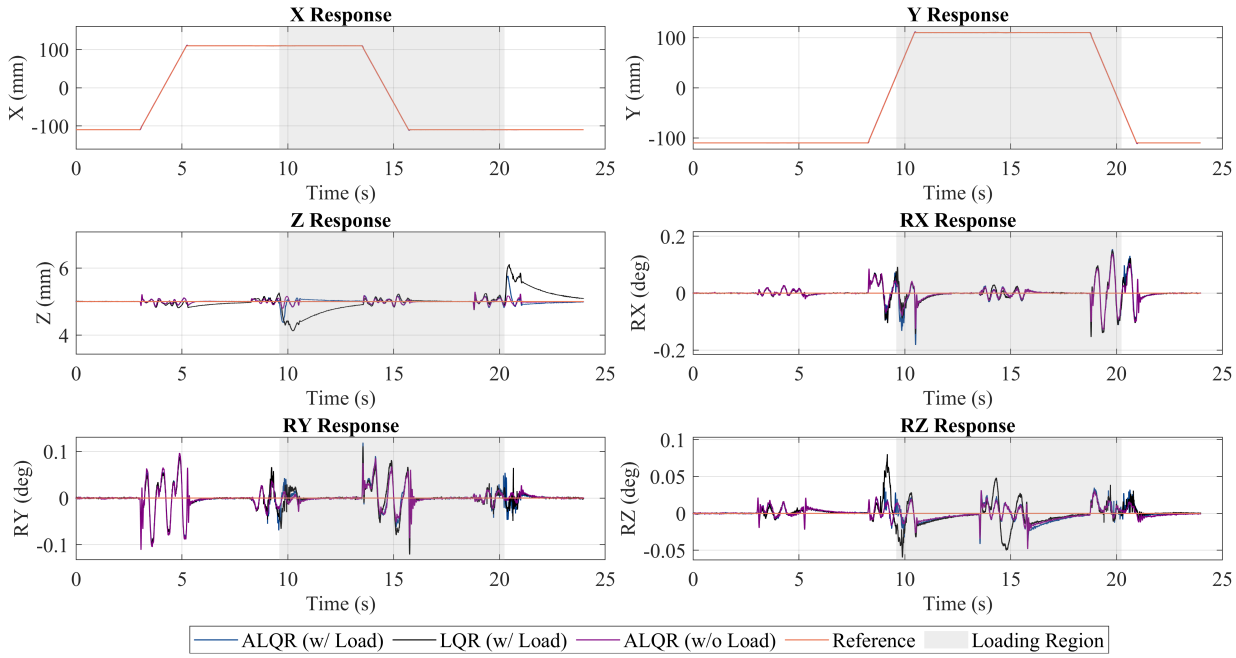



Figure 6.13: Control signals for the 6-Pole Halbach mover during the rectangle trajectory tracking.

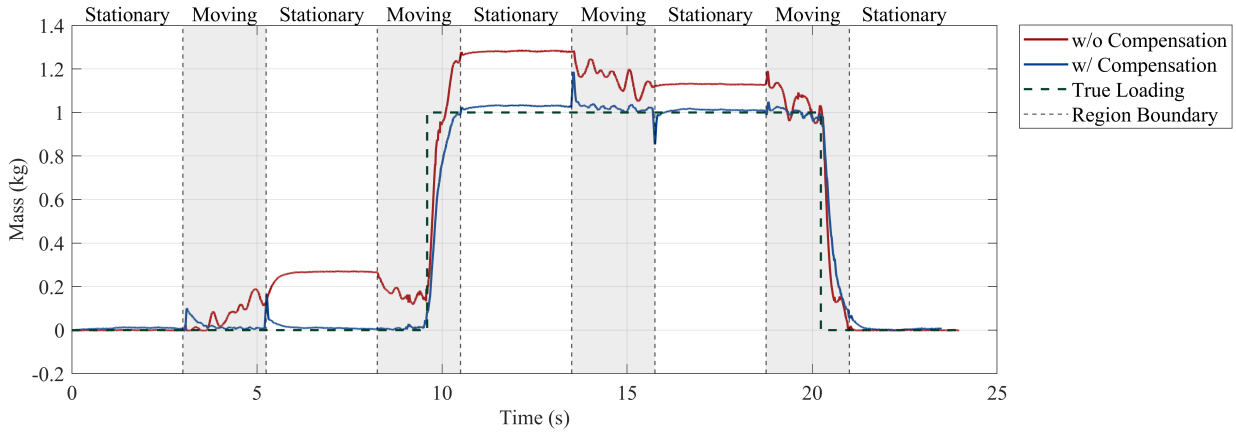



Figure 6.14: Mass loading curve while the mover is tracking a rectangle trajectory for the 6-Pole Halbach mover

Table 6.1: Summary of real-time estimation results for payload mass and center-of-mass location during levitation experiments.

| | | **5 Pole** | | | | | | | | | | | | | | | |
|---|---|---|---|---|---|---|---|---|---|---|---|---|---|---|---|---|---|
| | | Average | | | | Above 1 Coil | | | | Above 2 Coil | | | | Above 4 Coil | | | |
| Experiment Type | Target Payload Mass (kg) | $\mu$ (kg) | $\sigma$ (g) | MAPE (%) | $\lvert\Delta\rvert$ (g) | $\mu$ (kg) | $\sigma$ (g) | MAPE (%) | $\lvert\Delta\rvert$ (g) | $\mu$ (kg) | $\sigma$ (g) | MAPE (%) | $\lvert\Delta\rvert$ (g) | $\mu$ (kg) | $\sigma$ (g) | MAPE (%) | $\lvert\Delta\rvert$ (g) |
| Single Loading | 1 | 1.0115 | 3.1 | 0.8 | 8.2 | 1.0015 | 3.5 | 0.16 | 1.6 | 1.0115 | 3.2 | 1.2 | 11.5 | 1.0114 | 3.1 | 1.1 | 11.4 |
| | 2.013 | 2.0429 | 3.5 | 1.3 | 25.4 | 2.0294 | 3.2 | 0.8 | 16.4 | 2.0428 | 3.4 | 1.5 | 29.8 | 2.0429 | 3.5 | 1.5 | 29.9 |
| | 2.264 | 2.2787 | 3.6 | 0.7 | 15.3 | 2.2804 | 3.6 | 0.7 | 16.4 | 2.2855 | 3.7 | 0.9 | 21.5 | 2.2719 | 3.5 | 0.3 | 7.9 |
| Sequential Loading | 1.01 $\rightarrow$ | 1.0217 | 2.8 | 1.4 | 14 | 1.014 | 3.0 | 1.1 | 11 | 1.0238 | 3.0 | 1.4 | 14 | 1.0274 | 2.8 | 1.7 | 17 |
| | 2.01 $\rightarrow$ | 2.0363 | 2.8 | 1.5 | 31 | 2.0214 | 2.8 | 1.2 | 25 | 2.0386 | 2.9 | 1.4 | 29 | 2.0489 | 2.9 | 1.9 | 39 |
| | 2.26 $\rightarrow$ | 2.289 | 2.8 | 1.5 | 34 | 2.2678 | 2.8 | 1.0 | 23 | 2.2824 | 2.8 | 1.4 | 32 | 2.3067 | 2.7 | 2.1 | 47 |
| | 2.51 | 2.546 | 3.0 | 1.6 | 41 | 2.5245 | 3.0 | 1.2 | 30 | 2.5483 | 2.9 | 1.5 | 38 | 2.5653 | 3.0 | 2.2 | 55 |
| | Target Payload Location [(x,y) cm] | $\mu$ (cm) | $\sigma$(cm) | MAAPE (%) | $\lvert\Delta\rvert$ (cm) | $\mu$ (cm) | $\sigma$ (cm) | MAAPE (%) | $\lvert\Delta\rvert$ (cm) | $\mu$ (cm) | $\sigma$ (cm) | MAAPE (%) | $\lvert\Delta\rvert$ (cm) | $\mu$(cm) | $\sigma$ (cm) | MAAPE (%) | $\lvert\Delta\rvert$ (cm) |
| Side Loading | (0, 9) | (-0.6, 11.0) | (0.4, 1.9) | (157, 24) | (0.6, 2.3) | (-0.6, 12) | (0.4, 0.3) | (157, 34) | (0.6, 3.2) | (-0.8, 12.2) | (0.4, 0.1) | (157, 34) | (0.8, 3.2) | (-0.4, 8.4) | (0.4, 0.4) | (157, 5.6) | (0.4, 0.5) |
| | (4.5, 0) | (5.7, -0.1) | (0.7, 0.5) | (24, 157) | (1.2, 0.4) | (6.6, 0.2) | (0.3, 0.5) | (42, 157) | (2.1, 0.4) | (5.3, -0.5) | (0.1, 0.4) | (19, 157) | (0.8, 0.5) | (5.1,-0.04) | (0.2,0.4) | (13,157) | (0.6,0.3) |
| | (4.5, -4.5) | (5.0,-6.1) | (0.8,1.0) | (17,32) | (0.8,1.6) | (5.8, -6.8) | (0.03, 0.3) | (29, 47) | (1.3, 2.3) | (5.1,-6.7) | (0.5,0.1) | (14,46) | (0.6,2.2) | (4.1,-4.7) | (0.1,0.1) | (9.0,5.3) | (0.4,0.2) |
| | (4.5, -10) | (6.4, -13.6) | (1.0, 2.3) | (39, 33) | (1.9, 3.6) | (7.5, -15.7) | (0.2, 0.7) | (58, 52) | (3.0, 5.7) | (6.7, -15.2) | (0.5, 0.3) | (46, 48) | (2.2, 5.2) | (5.3, -11) | (0.3, 0.3) | (17, 10) | (0.8, 1) |
| | (4.5, -14) | (6.7, -20) | (1.2, 3.5) | (43, 37) | (2.1, 5.6) | (6.9, -21.6) | (0.3, 0.7) | (49, 50) | (2.4, 7.6) | (8.0, -22,2) | (0.3, 1.3) | (65, 53) | (3.5, 8.2) | (5.2, -15.1) | (0.2, 0.4) | (14.4, 7.9) | (0.7, 1.1) |
| | (5, 8) | (5.8, 9.5) | (0.7, 1.3) | (16, 20) | (0.8, 1.7) | (6.5, 10.3) | (0.6, 0.6) | (29, 29) | (1.5, 2.4) | (5.2, 10.4) | (0.2, 0.3) | (3.6, 29) | (0.2, 2.4) | (5.8, 7.8) | (0.1, 0.2) | (15, 2.1) | (0.7, 0.2) |
| | (9, 0) | (9.9, 0.2) | (1.6, 0.2) | (13, 157) | (1.2, 0.2) | (9.1, 0.2) | (0.2, 0.2) | (2, 157) | (0.2, 0.2) | (12, 0.3) | (0.4, 0.1) | (32, 157) | (3.0, 0.3) | (8.7, 0.02) | (0.2, 0.1) | (3.9, 157) | (0.3, 0.08) |
| | (9, 5) | (9.6, 6.3) | (1.4, 0.9) | (11, 24) | (1.0, 1.3) | (11.3, 7.0) | (0.7, 0.6) | (25, 37) | (2.3, 2.0) | (8.4, 6.7) | (0.3, 0.2) | (6.6, 33) | (0.6, 1.7) | (8.9, 5.2) | (0.2, 0.02) | (1.5, 3.3) | (0.1, 0.2) |
| | | **6 Pole** | | | | | | | | | | | | | | | |
| | | Average | | | | Above 1 Coil | | | | Above 2 Coil | | | | Above 4 Coil | | | |
| Experiment Type | Target Payload Mass (kg) | $\mu$ (kg) | $\sigma$ (g) | MAPE (%) | $\lvert\Delta\rvert$ (g) | $\mu$ (kg) | $\sigma$ (g) | MAPE (%) | $\lvert\Delta\rvert$ (g) | $\mu$ (kg) | $\sigma$ (g) | MAPE (%) | $\lvert\Delta\rvert$ (g) | $\mu$ (kg) | $\sigma$ (g) | MAPE (%) | $\lvert\Delta\rvert$ (g) |
| Single Loading | 0.250 | 0.2588 | 2.0 | 3.9 | 9.9 | 0.2618 | 2.0 | 4.7 | 11.8 | 0.2597 | 2.3 | 3.9 | 9.7 | 0.2579 | 2.4 | 3.1 | 7.9 |
| | 0.5 | 0.5182 | 2.5 | 3.9 | 19.7 | 0.5226 | 2.1 | 4.5 | 23 | 0.5190 | 2.6 | 3.8 | 19 | 0.5174 | 2.5 | 3.5 | 17 |
| | 1.0 | 1.0253 | 2.4 | 3.1 | 31 | 1.0436 | 2.2 | 4.4 | 44 | 1.0294 | 2.4 | 2.9 | 29 | 1.0223 | 2.4 | 2.2 | 22 |
| Sequential Loading | 0.250 $\rightarrow$ | 0.2430 | 2.2 | 2.8 | 7 | 0.2432 | 2.2 | 2.7 | 7 | 0.2410 | 2.3 | 3.6 | 9 | 0.2447 | 2.1 | 2.1 | 5 |
| | 0.750 $\rightarrow$ | 0.7668 | 2.2 | 2.2 | 17 | 0.7743 | 2.0 | 3.2 | 24 | 0.7614 | 2.3 | 1.5 | 11 | 0.7646 | 2.4 | 1.9 | 15 |
| | 1.0 | 1.0246 | 2.2 | 2.5 | 25 | 1.0369 | 2.1 | 3.7 | 37 | 1.0203 | 2.2 | 2 | 20 | 1.0166 | 2.2 | 1.7 | 17 |
| | Target Payload Location [(x,y) cm] | $\mu$ (cm) | $\sigma$(cm) | MAAPE (%) | $\lvert\Delta\rvert$ (cm) | $\mu$ (cm) | $\sigma$ (cm) | MAAPE (%) | $\lvert\Delta\rvert$ (cm) | $\mu$ (cm) | $\sigma$ (cm) | MAAPE (%) | $\lvert\Delta\rvert$ (cm) | $\mu$(cm) | $\sigma$ (cm) | MAAPE (%) | $\lvert\Delta\rvert$ (cm) |
| Side Loading | (0, 7) | (0.8, 7.5) | (0.6, 0.4) | (157, 7.1) | (1.0, 0.5) | (0.4, 7.7) | (0.9, 0.3) | (157, 9.6) | (0.7, 0.7) | (1.1, 7.7) | (0.3, 0.2) | (157, 9.8) | (1.1, 0.7) | (1.0, 7.1) | (0.4, 0.2) | (157, 1.7) | (1.0, 0.1) |
| | (0, -7) | (0.2, -7.0) | (0.2, 0.5) | (157, 6.0) | (0.2, 0.4) | (0.1, -6.7) | (0.1, 0.3) | (157, 4.3) | (0.1, 0.3) | (0.4, -6.5) | (0.1, 0.1) | (157, 6.9) | (0.4, 0.5) | (0.2, -7.5) | (0.1, 0.3) | (157, 6.6) | (0.2, 0.5) |
| | (0, 14) | (0.1, 14.5) | (0.4, 0.4) | (157, 4.0) | (0.4, 0.6) | (-0.2, 14.7) | (0.3, 0.5) | (157, 5.2) | (0.3, 0.7) | (0.1, 14.7) | (0.5, 0.2) | (157, 5.0) | (0.4, 0.7) | (0.4, 14.1) | (0.4, 0.2) | (157, 1.3) | (0.4, 0.2) |
| | (0, -14) | (0.4, -14.0) | (0.3, 0.7) | (157, 4.1) | (0.4, 0.6) | (0.1, -13.6) | (0.3, 0.1) | (157, 3.0) | (0.2, 0.4) | (0.6, -13.5) | (0.1, 0.3) | (157, 3.7) | (0.6, 0.5) | (0.5, -14.8) | (0.2, 0.2) | (157, 5.6) | (0.5, 0.8) |
| | (3.5, 3.5) | (4.1, 3.8) | (0.3, 0.2) | (17.8, 8.0) | (0.6, 0.3) | (4.0, 4.0) | (0.4, 0.3) | (13.1, 13.1) | (0.5, 0.5) | (4.3, 3.8) | (0.1, 0.1) | (22.7, 8.4) | (0.8, 0.3) | (4.1, 3.6) | (0.03, 0.1) | (17.5, 2.5) | (0.6, 0.1) |
| | (7, 7) | (7.5, 7.1) | (0.3, 0.2) | (7.8, 2.5) | (0.5, 0.2) | (7.7, 7.2) | (0.3, 0.1) | (10.4, 3.3) | (0.7, 0.2) | (7.6, 7.1) | (0.04, 0.1) | (9.0, 1.5) | (0.6, 0.1) | (7.3, 7.0) | (0.3, 0.2) | (4.3, 2.4) | (0.3, 0.2) |
| | (11, 10.5) | (11.4, 10.5) | (0.2, 0.4) | (4.0, 2.7) | (0.4, 0.3) | (11.3, 10.8) | (0.3, 0.1) | (2.4, 2.6) | (0.3, 0.3) | (11.6, 10.3) | (0.03, 0.5) | (5.2, 3.8) | (0.6, 0.4) | (11.4, 10.5) | (0.3, 0.2) | (4.0, 1.3) | (0.4, 0.1) |

# Chapter 7

# Conclusion and Future Work

## 7.1 Conclusion

This thesis presented the development of a magnetically levitated planar motion platform equipped with real-time payload mass and location estimation capabilities. A novel 5-pole Halbach array mover was constructed to enhance force density across the stator's working region, increasing payload capacity by approximately 2 times that of an existing 6-pole design. A current-wrench decoupling algorithm and data-driven force modeling method were employed to enable real-time control and precision movement of the mover. Additionally, calibration procedures were devised to compensate for construction irregularities in the stator and mover as well as modeling inaccuracies. Following this, a comprehensive adaptive control architecture was implemented, allowing the system to maintain stability and accurately estimate the external loading parameters of a payload during both stationary levitation and dynamic motion.

Throughout a series of levitation experiments, the magnetically levitated planar motor demonstrated robust performance across a variety of testing conditions. In the single-mass loading experiments, the system was able to estimate the mass of unknown payloads with high accuracy, achieving mean absolute percentage errors (MAPEs) as low as 0.6% on the 5-pole array. The lowest MAPE was achieved when the center of the 5-pole mover was directly above a single coil in the stator. The 6-pole mover—used here as a comparative benchmark—achieved a lowest MAPE of 2.2% when the mover's center was in between four adjacent coils. Payload mass convergence was generally achieved within approximately three seconds for both mover designs, even under conditions involving occlusions in the motion sensing system. The minimum resolvable mass difference, based on a $4\sigma$ confidence

interval, was as low as 10 g in some configurations. When multiple payloads were added in sequence, the system maintained stable estimation without significant drift. As well, MAPE error was shown to remain consistent throughout the successive loading, regardless of the order in which the weights were applied. These experiments confirm the robustness of the parameter identification strategy across time and successive disturbances.

The platform was also able to infer the spatial location of payloads on the mover during operation. Results showed that estimation accuracy was sensitive to both mover design and payload position. The 6-pole Halbach array exhibited payload location absolute errors below 1 cm in both axes, while the 5-pole array produced approximately double the deviations. Additionally, the absolute error increased when payloads were placed near the edge of the mover of the 5-pole mover—this was not as clearly observable for the 6-pole mover array. This discrepancy was primarily attributed to the physical curvature of the mover frame induced by the internal magnetic forces. The estimation error also varied between stator locations. This was attributed to the spatial arrangement of permanent magnets and coils, which influenced the spatial coupling between torque generation and estimation. For the most accurate estimation, when the 5-pole mover was centered over four coils, an improved localization accuracy was achieved due to more favourable coil-to-magnet alignment. This phenomenon had a more pronounced impact on the 5-pole array compared to the 6-pole array.

In the final experiment, the system was tested while tracking a trajectory and dynamically loading a payload. Without any compensation, the estimated payload mass deviated by up to 25%, leading to degraded tracking and delayed convergence in the estimation results. By applying a precomputed spatial mass compensation profile, steady-state errors in the payload mass estimates were reduced to 3% throughout the entire trajectory of the mover. As well, the adaptive controller was able to converge the mover's position to the desired track within 1.4 seconds when a payload was applied and subsequently removed—matching the performance of the unloaded case and outperforming the non-adaptive baseline. This demonstrated the system's robustness in preserving stability and estimation accuracy under dynamic loading conditions.

Taken together, these results demonstrate that the developed magnetically levitated planar motor can operate reliably under the adaptive and dynamic conditions demanded by flexible manufacturing environments. The integration of high-precision planar motion, real-time payload estimation, and adaptive compensation positions this system for seamless incorporation with external manipulators, intelligent workstations, and shared autonomy frameworks. As constructed, this platform is not merely a prototype but a fully deployable solution for intelligent and flexible magnetic levitation.

## 7.2 Future Work

The development of this levitation platform builds upon the innovative contributions of many researchers and is expected to continue evolving in versatility and capability for future work. While there are numerous directions for improvement, several key areas for future development are outlined below:

- One natural extension of this work is the integration of the existing platform with external robotic systems—such as external robotic arms, wheeled robots, unmanned aerial vehicles, or other magnetically levitated movers. Research into such multi-robot interactions could advance object handling, optimize path planning for multiple robotic systems, and enable novel manufacturing processes. The ability to estimate both mass and location of payloads in real-time could also facilitate intelligent hand-offs between workstations, improve alignment during exchange, or enhance safety during shared manipulation tasks.

- Improving the sensing infrastructure is another critical avenue for potential research. While infrared motion capture systems offer precise tracking, they remain a significant source of error due to the occlusions of the reflective markers, inconsistent drift in measurement values, and workspace constraints imposed by the cameras' location and field of view. Exploring alternative sensing options such as onboard inertial measurement units, computer vision systems, or embedded magnetic field sensors could reduce reliance on external infrastructure and make the system more robust in practical settings.

- Exploring alternative control paradigms may yield additional gains in adaptability and performance. While the ALQR controller used in this work proved effective, neural network-based controllers or reinforcement learning approaches may enable better generalization across unmodeled disturbances, actuator nonlinearities, or more complex payload geometries.

- While this work adopts certain assumptions to linearize the governing equations, future efforts could focus on developing a more comprehensive treatment of the system's nonlinear dynamics. Such an approach would eliminate the need for the small-angle approximation and enable more accurate modeling of external factors, including magnetic damping from sheets on the stator surface or mutual magnetic interference between multiple mover units. As well, this work relies on the assumption that the payload behaves as a rigid body. Shifting the focus toward non-rigid and

non-uniform loads would significantly improve the flexibility of magnetic levitation systems in handling more complex and realistic manipulation tasks.

- While the system has demonstrated accuracy in estimating payload parameters within the designed operating range, future research could investigate methods to extend the payload capacity of existing movers. One approach is to increase the system's available power by enhancing the power supply. This increase in power could, in turn, be used to support heavier payloads or provide larger horizontal accelerations. Additionally, research could explore incorporating supplementary magnetic materials within the stator to augment the magnetic field generated by the coils, potentially improving lifting capacity without solely relying on increased electrical input.

# References


[1] S. A. Howard, C. DellaCorte, and M. J. Dube, "Magnetic levitation for long-life space mechanisms: Technology assessment and remaining challenges," *NASA/TM—2019-220052*, 2019. Available at http://ntrs.nasa.gov.

[2] W. Morales, R. Fusaro, and A. Kascak, "Permanent magnetic bearing for spacecraft applications," *NASA/TM—2003-211996/REV1*, 2008. Available at http://ntrs.nasa.gov.

[3] D. J. Clark, M. J. Jansen, and G. T. Montague, "An overview of magnetic bearing technology for gas turbine engines," *NASA/TM—2004-213177*, 2004. Available at http://ntrs.nasa.gov.

[4] Maglev Aero, "MagLev HyperDrive." [Online]. Available at https://maglevaero.com/, 2025.

[5] S. M. Knowlton, B. Yenilmez, R. Amin, and S. Tasoglu, "Magnetic levitation coupled with portable imaging and analysis for disease diagnostics," *Journal of Visualized Experiments*, vol. 120, p. e55012, 2017.

[6] N. G. Durmus, C. T. H., S. Guven, K. Sridhar, A. A. Yildiz, G. Calibasi, I. Ghiran, R. W. Davis, L. M. Steinmetz, and U. Demirci, "Magnetic levitation of single cells," *Proceedings of the National Academy of Sciences*, vol. 112, no. 28, pp. E3661–E3668, 2015. Available at https://www.pnas.org/doi/abs/10.1073/pnas.1509250112.

[7] Z. Liu, Z. Long, and X. Li, *Maglev Train Overview*, pp. 1–28. Berlin, Heidelberg: Springer, Berlin, Heidelberg, 2015.

[8] B. Jones, "Flying without wings: The world's fastest trains," *CNN Travel*, 2023. [Online]. Accessed on: August 8, 2025.

[9] W. Kim and D. L. Trumper, "High-precision magnetic levitation stage for photolithography," *Precision Engineering*, vol. 22, no. 2, pp. 66–77, 1998. Image reprinted with permission from Elsevier.

[10] A. Jain, P. Jain, F. T. Chan, and S. Singh, "A review on manufacturing flexibility," *International Journal of Production Research*, vol. 51, no. 19, pp. 5946–5970, 2013.

[11] L. L. Koste and M. K. Malhotra, "A theoretical framework for analyzing the dimensions of manufacturing flexibility," *Journal of Operations Management*, vol. 18, no. 1, pp. 75–93, 1999.

[12] J. J. Browne, D. Dubois, K. Rathmill, S. Sethi, and K. Stecke, "Classification of flexible manufacturing systems," *The FMS magazine*, vol. 2, no. 2, pp. 114–117, 1984.

[13] A. K. Sethi and S. P. Sethi, "Flexibility in manufacturing: A survey," *International Journal of Flexible Manufacturing Systems*, vol. 2, no. 4, pp. 289–328, 1990.

[14] Omnia Wheel Ltd., "Omni Directional Sortation." [Online]. Available at https://www.omniawheel.com/conveyor-systems, 2023.

[15] Planar Motor Inc., "M4 XBot." [Online]. Available at https://www.planarmotor.com/en/m4-xbot, 2025.

[16] Beckhoff Automation Ltd., "Beckhoff Automation: XPlanar for Flying Motion Control." [Online]. Available at https://www.materialhandling247.com/product/xplanar_for_flying_motion_control/beckhoff_automation, 2025.

[17] B. V. Jayawant, "Electromagnetic suspension and levitation," *Reports on Progress in Physics*, vol. 44, no. 4, pp. 411–477, 1981.

[18] M. T. Thompson, "Eddy current magnetic levitation. models and experiments," *IEEE Potentials*, vol. 19, no. 1, pp. 40–44, 2000.

[19] E. H. Brandt, "Levitation in physics," *Science*, vol. 243, no. 4889, pp. 349–355, 1989.

[20] K. B. Ma, Y. V. Postrekhin, and W. K. Chu, "Superconductor and magnet levitation devices," *Review of Scientific Instruments*, vol. 74, no. 12, pp. 4989–5017, 2003.

[21] M. D. Simon, L. O. Heflinger, and A. K. Geim, "Diamagnetically stabilized magnet levitation," *American Journal of Physics*, vol. 69, no. 6, pp. 702–713, 2001.

[22] F. Wicks, "The blacksmith's motor," *Mechanical Engineering*, vol. 121, no. 7, pp. 66–69, 1999.

[23] M. B. Khamesee, N. Kato, Y. Nomura, and T. Nakamura, "Design and control of a microrobotic system using magnetic levitation," *IEEE/ASME Transactions on Mechatronics*, vol. 7, no. 1, pp. 1–14, 2002.

[24] "Electromagnetic levitation," *Nature*, vol. 146, no. 3699, p. 398, 1940.

[25] W. Kim, D. L. Trumper, and J. B. Bryan, "Linear motor-leviated stage for photolithography," *CIRP Annals*, vol. 46, no. 1, pp. 447–450, 1997.

[26] K. S. Jung and Y. S. Baek, "Study on a novel contact-free planar system using direct drive DC coils and permanent magnets," *IEEE/ASME Transactions on Mechatronics*, vol. 7, no. 1, pp. 35–43, 2002.

[27] S. Verma, W. Kim, and J. Gu, "Six-axis nanopositioning device with precision magnetic levitation technology," *IEEE/ASME Transactions on Mechatronics*, vol. 9, no. 2, pp. 384–391, 2004.

[28] Z. Zhang and C.-H. Menq, "Six-Axis Magnetic Levitation and Motion Control," *IEEE Transactions on Robotics*, vol. 23, no. 2, pp. 196–205, 2007.

[29] I. J. C. Compter, "Electro-dynamic planar motor," *Precision Engineering*, vol. 28, no. 2, pp. 171–180, 2004.

[30] J. W. Jansen, C. M. M. van Lierop, E. A. Lomonova, and A. J. A. Vandenput, "Magnetically levitated planar actuator with moving magnets," *IEEE Transactions on Industry Applications*, vol. 44, no. 4, pp. 1108–1115, 2008.

[31] J. M. M. Rovers, J. W. Jansen, and E. A. Lomonova, "Multiphysical analysis of moving-magnet planar motor topologies," *IEEE Transactions on Magnetics*, vol. 49, no. 12, pp. 5730–5741, 2013.

[32] J. W. Jansen, *Magnetically levitated planar actuator with moving magnets : electromechanical analysis and design*. PhD Dissertation, Eindhoven University of Technology, 2007.

[33] C. Trakarnchaiyo, Y. Wang, and M. B. Khamesee, "Design of a compact planar magnetic levitation system with wrench–current decoupling enhancement," *Applied Sciences*, vol. 13, no. 4, 2023.

[34] X. Lu, M. Dyck, and Y. Altintas, "Magnetically levitated six degree of freedom rotary table," *CIRP Annals*, vol. 64, no. 1, pp. 353–356, 2015. Image reprinted with permission from Elsevier.

[35] F. Xu, K. Zhang, and X. Xu, "Development of magnetically levitated rotary table for repetitive trajectory tracking," *Sensors*, vol. 22, no. 11, 2022.

[36] C. Elbuken, M. B. Khamesee, and M. Yavuz, "Design and implementation of a micromanipulation system using a magnetically levitated MEMS robot," *IEEE/ASME Transactions on Mechatronics*, vol. 14, no. 4, pp. 434–445, 2009. Contains public sector information licensed under the Open Government Licence v3.0 and available at https://www.nationalarchives.gov.uk/doc/open-government-licence/version/3/.

[37] G. Akoun and J. Yonnet, "3D analytical calculation of the forces exerted between two cuboidal magnets," *IEEE Transactions on Magnetics*, vol. 20, no. 5, pp. 1962–1964, 1984.

[38] J. M. M. Rovers, J. W. Jansen, and E. A. Lomonova, "Modeling of relative permeability of permanent magnet material using magnetic surface charges," *IEEE Transactions on Magnetics*, vol. 49, no. 6, pp. 2913–2919, 2013.

[39] F. Bancel, "Magnetic nodes," *Journal of Physics D: Applied Physics*, vol. 32, no. 17, pp. 2155–2161, 1999.

[40] J. Yonnet and H. Allag, "Three-dimensional analytical calculation of permanent magnet interactions by "magnetic node" representation," *IEEE Transactions on Magnetics*, vol. 47, no. 8, pp. 2050–2055, 2011.

[41] H. Cho, C. Im, and H. Jung, "Magnetic field analysis of 2-D permanent magnet array for planar motor," *IEEE Transactions on Magnetics*, vol. 37, no. 5, pp. 3762–3766, 2001.

[42] J. W. Jansen, C. M. M. van Lierop, E. A. Lomonova, and A. J. A. Vandenput, "Modeling of magnetically levitated planar actuators with moving magnets," *IEEE Transactions on Magnetics*, vol. 43, no. 1, pp. 15–25, 2007.

[43] J. W. Jansen, J. P. C. Smeets, T. T. Overboom, J. M. M. Rovers, and E. A. Lomonova, "Overview of analytical models for the design of linear and planar motors," *IEEE Transactions on Magnetics*, vol. 50, no. 11, p. 8206207, 2014.

[44] J. M. M. Rovers, J. W. Jansen, and E. A. Lomonova, "Analytical calculation of the force between a rectangular coil and a cuboidal permanent magnet," *IEEE Transactions on Magnetics*, vol. 46, no. 6, pp. 1656–1659, 2010.

[45] M. R. Hamers, *Actuation principles of permanent magnet synchronous planar motors: a literature survey*, vol. 2005.149 of *DCT rapporten*. Technische Universiteit Eindhoven, 2005.

[46] B. Kou, F. Xing, L. Zhang, C. Zhang, and Y. Zhou, "A real-time computation model of the electromagnetic force and torque for a maglev planar motor with the concentric winding," *Applied Sciences*, vol. 7, no. 1, 2017.

[47] H. S. Choi, S. H. Lee, Y. S. Kim, K. T. Kim, and I. H. Park, "Implementation of virtual work principle in virtual air gap," *IEEE Transactions on Magnetics*, vol. 44, no. 6, pp. 1286–1289, 2008.

[48] SimuTech Group, "Calculating motor torque with ansys maxwell." [Online]. Available at https://simutechgroup.com/calculating-motor-torque-with-ansys-maxwell/, 2024.

[49] F. R. Ismagilov, R. R. Urazbakhtin, and A. R. Khakimyanov, "Modeling and validation of calculation models of an electric motor made of amorphous soft magnetic material," in *2024 International Russian Automation Conference (RusAutoCon)*, pp. 861–867, 2024.

[50] Y. M. Du, P. Xia, and L. Y. Xiao, "Calculating magnetic force of permanent magnet using maxwell stress method," *IEEE Transactions on Applied Superconductivity*, vol. 10, no. 1, pp. 1392–1394, 2000.

[51] J. de Boeij, E. Lomonova, and J. Duarte, "Contactless planar actuator with manipulator: A motion system without cables and physical contact between the mover and the fixed world," *IEEE Transactions on Industry Applications*, vol. 45, no. 6, pp. 1930–1938, 2009.

[52] X. Zhang, C. Trakarnchaiyo, H. Zhang, and M. B. Khamesee, "Magtable: A tabletop system for 6-dof large range and completely contactless operation using magnetic levitation," *Mechatronics*, vol. 77, p. 102600, 2021.

[53] J. de Boeij, E. Lomonova, and A. J. A. Vandenput, "Look-up table based real-time commutation of 6-DOF planar actuators," in *2007 IEEE International Conference on Control Applications*, pp. 1118–1123, 2007.

[54] C. Trakarnchaiyo and M. B. Khamesee, "A novel wrench–current decoupling strategy to extend the use of small lookup data for a long-range maglev planar motor," *Actuators*, vol. 12, no. 9, 2023.

[55] J. Peng, Y. Zhou, and G. Liu, "Calculation of a new real-time control model for the magnetically levitated ironless planar motor," *IEEE Transactions on Magnetics*, vol. 49, no. 4, pp. 1416–1422, 2013.

[56] D. Yuan, M. Zhang, Y. Zhu, L. Wang, X. Li, and C. Hu, "Extended unified wrench model suitable for the end effect of the ironless permanent magnet planar motor," *IET Electric Power Applications*, vol. 13, no. 3, pp. 402–409, 2019.

[57] Y. Zhu, D. Yuan, M. Zhang, F. Liu, and C. Hu, "Unified wrench model of an ironless permanent magnet planar motor with 2D periodic magnetic field," *IET Electric Power Applications*, vol. 12, no. 3, pp. 423–430, 2018.

[58] Z. Xu, X. Zhang, and M. B. Khamesee, "Real-time data-driven force and torque modeling on a 2-D halbach array by a symmetric coil considering end effect," *IEEE Transactions on Magnetics*, vol. 58, no. 11, pp. 1–10, 2022.

[59] Planar Motor Inc., "Hygienic Planar Motor." [Online]. Available at https://www.planarmotor.com/en/videos, 2022.

[60] E. C. Benck, C. Stambaugh, E. Mulhern, P. Abbott, and Z. Kubarych, "Progress on vacuum-to-air mass calibration system using magnetic suspension to disseminate the planck-constant realized kilogram," *Acta IMEKO*, vol. 6, no. 2, 2017. Image copyright license available at https://creativecommons.org/licenses/by/4.0/.

[61] X. Yang, R. Kleinrahm, M. O. McLinden, and M. Richter, "The magnetic suspension balance: 40 years of advancing densimetry and sorption science," *International Journal of Thermophysics*, vol. 44, no. 11, 2023.

[62] J. W. Clark, "An electronic analytical balance," *Review of Scientific Instruments*, vol. 18, no. 12, 1947.

[63] C. Hu, Z. Wang, Y. Zhu, M. Zhang, and H. Liu, "Performance-oriented precision LARC tracking motion control of a magnetically levitated planar motor with comparative experiments," *IEEE Transactions on Industrial Electronics*, vol. 63, no. 9, pp. 5763–5773, 2016.

[64] Z. Xu, C. Trakarnchaiyo, C. Stewart, and M. B. Khamesee, "Modular maglev: Design and implementation of a modular magnetic levitation system to levitate a 2d halbach array," *Mechatronics*, vol. 99, p. 103148, 2024.

[65] P. K. Sinha and A. N. Pechev, "Model reference adaptive control of a maglev system with stable maximum descent criterion," *Automatica*, vol. 35, no. 8, pp. 1457–1465, 1999.

[66] B. Bidikli, "An observer-based adaptive control design for the maglev system," *Transactions of the Institute of Measurement and Control*, vol. 42, no. 14, pp. 2771–2786, 2020.

[67] M. Chen, C. Tsai, and L. Fu, "A novel design and control to improve positioning precision and robustness for a planar maglev system," *IEEE Transactions on Industrial Electronics*, vol. 66, no. 6, pp. 4860–4869, 2019.

[68] T. Zheng, X. Xu, X. Lu, L. Hao, and F. Xu, "Learning adaptive sliding mode control for repetitive motion tasks in maglev rotary table," *IEEE Transactions on Industrial Electronics*, vol. 69, no. 2, pp. 1836–1846, 2022.

[69] M. B. Hesse, "Action at a distance in classical physics," *Isis*, vol. 46, no. 4, pp. 337–353, 1955.

[70] J. F. Herbst and J. J. Croat, "Neodymium-iron-boron permanent magnets," *Journal of Magnetism and Magnetic Materials*, vol. 100, no. 1, pp. 57–78, 1991.

[71] K&J Magnetics, Inc, "Magnet grades." [Online]. https://www.kjmagnetics.com/blog/magnet-grade#section-1, n.d.

[72] K. Halbach, "Physical and optical properties of rare earth cobalt magnets," *Nuclear Instruments and Methods in Physics Research*, vol. 187, no. 1, pp. 109–117, 1981.

[73] J. Mallinson, "One-sided fluxes – a magnetic curiosity?," *IEEE Transactions on Magnetics*, vol. 9, no. 4, pp. 678–682, 1973.

[74] J. Courty and É. Kierlik, "Les magnets, aimants à un seul pôle?," *Pour la Science*, vol. 391, 2010.

[75] K. Halbach, "Application of permanent magnets in accelerators and electron storage rings (invited)," *Journal of Applied Physics*, vol. 57, no. 8, pp. 3605–3608, 1985.

[76] Z. T. Dydek, A. M. Annaswamy, and E. Lavretsky, "Adaptive control and the NASA X-15 program: A concise history, lessons learned, and a provably correct design," in *2008 American Control Conference*, pp. 2957–2962, 2008.

[77] P. Ioannou and B. Fidan, *Adaptive Control Tutorial*. 3600 University City Science Center, Philadelphia, PA: Society for Industrial and Applied Mathematics, 2006.

[78] F. L. Lewis, D. L. Vrabie, and V. L. Syrmos, "Optimal control of continuous-time systems," in *Optimal Control*, ch. 3–4, pp. 110–176, 177–212, John Wiley & Sons Ltd., 2012.

[79] C. Stewart, "Implementation of a modular magnetic levitation planar motor," Master's thesis, University of Waterloo, 2023. Available at http://hdl.handle.net/10012/19092.

[80] Z. Xu, *Design, Implementation, and Control of a Magnetic Levitated Planar Motor*. PhD Dissertation, University of Waterloo, 2024. Available at http://hdl.handle.net/10012/20268.

[81] B. L. Bowerman, R. T. O'Connell, and B. L. Bowerman, *Forecasting, Time Series, and Regression: An Applied Approach*. Thomson Brooks/Cole, fourth ed., 2005.

[82] S. Kim and H. Kim, "A new metric of absolute percentage error for intermittent demand forecasts," *International Journal of Forecasting*, vol. 32, no. 3, pp. 669–679, 2016.

[83] S. Makridakis, "Accuracy measures: theoretical and practical concerns," *International Journal of Forecasting*, vol. 9, no. 4, pp. 527–529, 1993.

# APPENDICES

# Appendix A

# Supplementary Figures and Extended Plots

This appendix contains additional plots and figures that provide detailed insights into the mover's performance at specific stator locations. These visualizations are included here either because they are too extensive for the main text or because they offer supplementary information that supports the analysis presented in the primary chapters.

## A.1 Maximum Payload Mass Analysis - Supplementary Plots

Section 4.2.2 presents the analysis conducted to determine the maximum load each mover can support across the entire working area without exceeding the allowable number of saturated coils. The plots provided in Figures A.1 and A.2 are extensions of Figure 4.12 by sampling a finer grid of weights slightly above and below the estimated maximum. Although it is physically possible to levitate loads exceeding the identified maximum, such operation is constrained to specific stator regions where the number of saturated coils remains below eight. This constraint must be considered in trajectory planning to ensure feasible actuation. In the saturated coil plots, regions shaded in blue correspond to lower power demands for vertical levitation, indicating greater available control authority for motion in the horizontal plane.

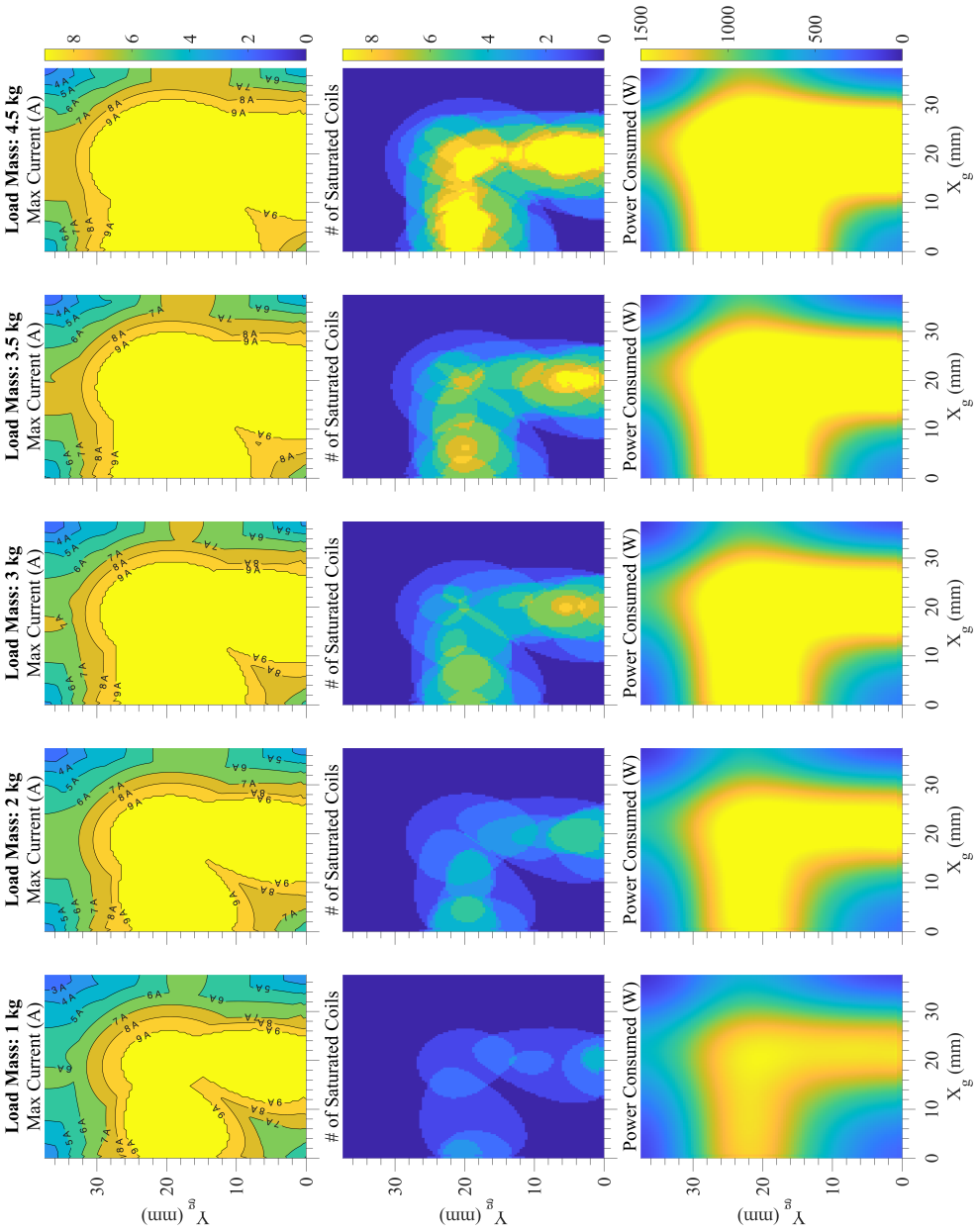



Figure A.1: Extended plots for the 5-pole mover showing the maximum coil current, # of saturated coils, and power consumption when levitating a load mass at various stator locations. The point $(X_g, Y_g) = (0, 0)$ corresponds to the center between four coils, $(X_g, Y_g) = (0, 38)$ and $(38, 0)$ represent positions between two adjacent coils, and $(X_g, Y_g) = (38, 38)$ denotes the center of a single coil.

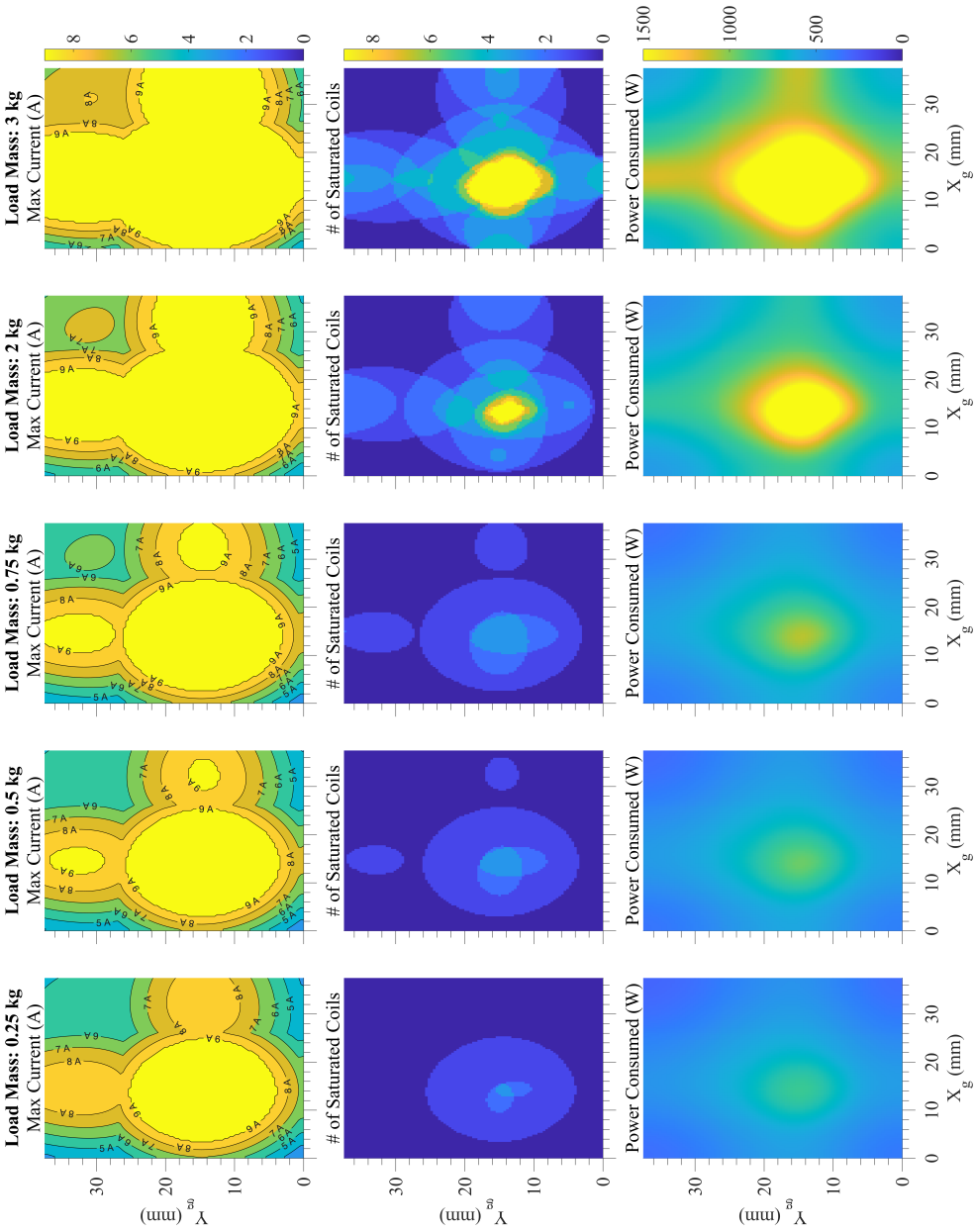



Figure A.2: Extended plots for the 6-pole mover showing the maximum coil current, # of saturated coils, and power consumption when levitating a load mass at various stator locations. The point $(X_g, Y_g) = (0, 0)$ corresponds to the center between four coils, $(X_g, Y_g) = (0, 38)$ and $(38, 0)$ represent positions between two adjacent coils, and $(X_g, Y_g) = (38, 38)$ denotes the center of a single coil.

## A.2 Experiment 2 - Alternative Stator Locations

The following plots refer to the sequential loading experiments for both the 6-pole and 5-pole Halbach arrays. The plots shown are for mover locations that performed slightly worse than the plots shown in Section 6.2. The results from the plots are also summarized in Table 6.1.

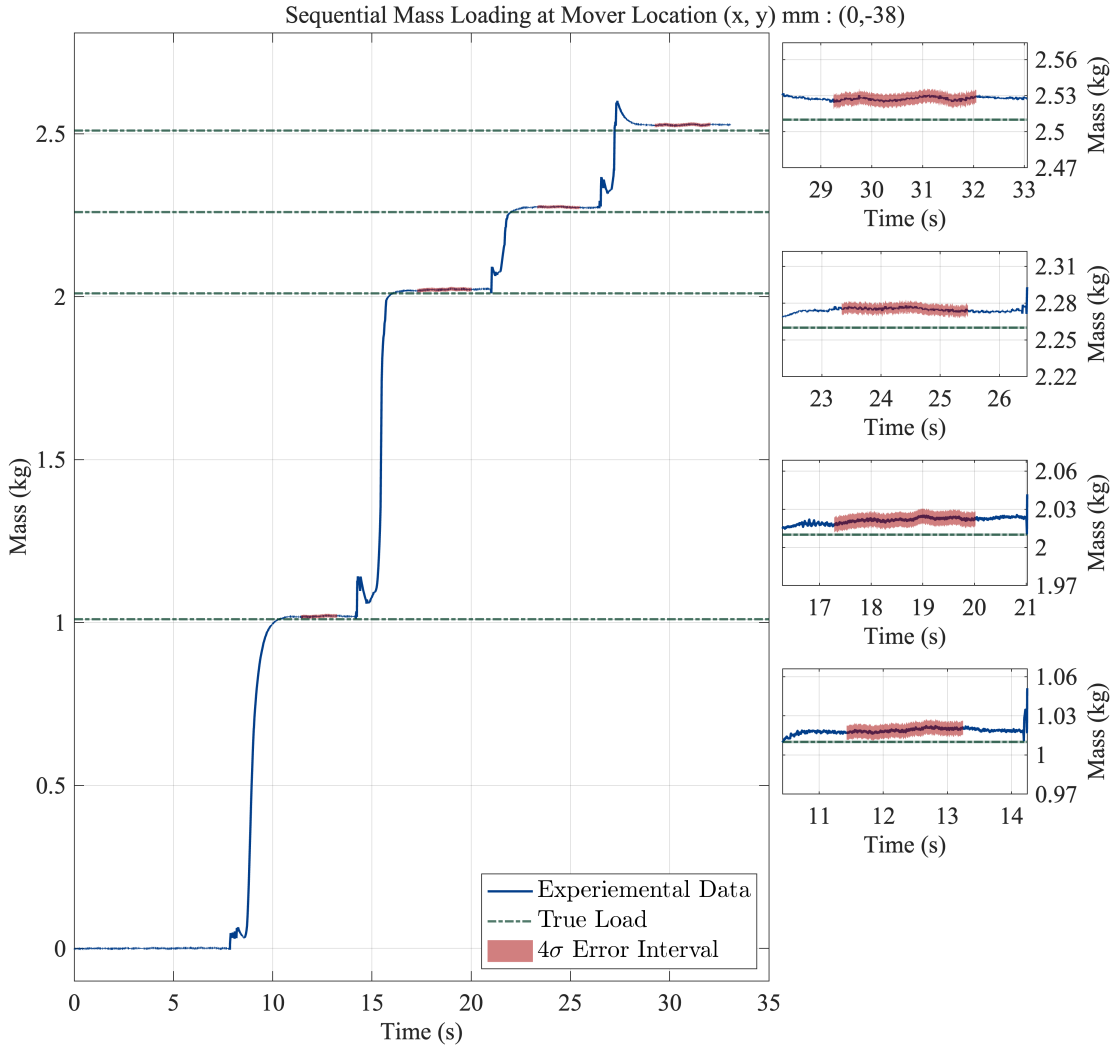



Figure A.3: Summary of successive mass loading performance when the 5-Pole Halbach is between 2 coils. The zoomed-in region highlights the response within the boxed area. Note that the exact loading times between trials were not held constant.

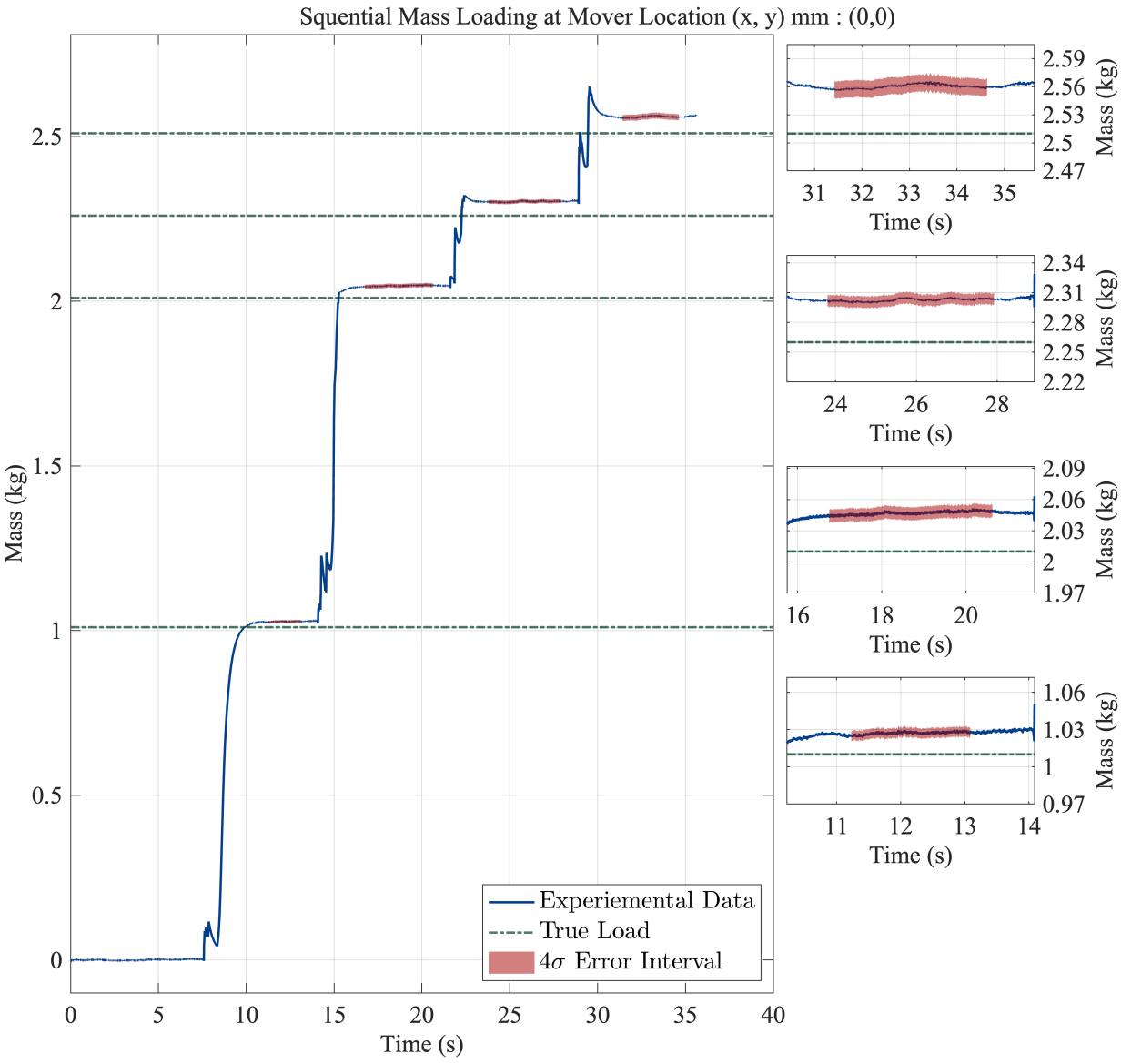



Figure A.4: Summary of successive mass loading performance when the 5-Pole Halbach is between 4 coils. The zoomed-in region highlights the response within the boxed area. Note that the exact loading times between trials were not held constant.

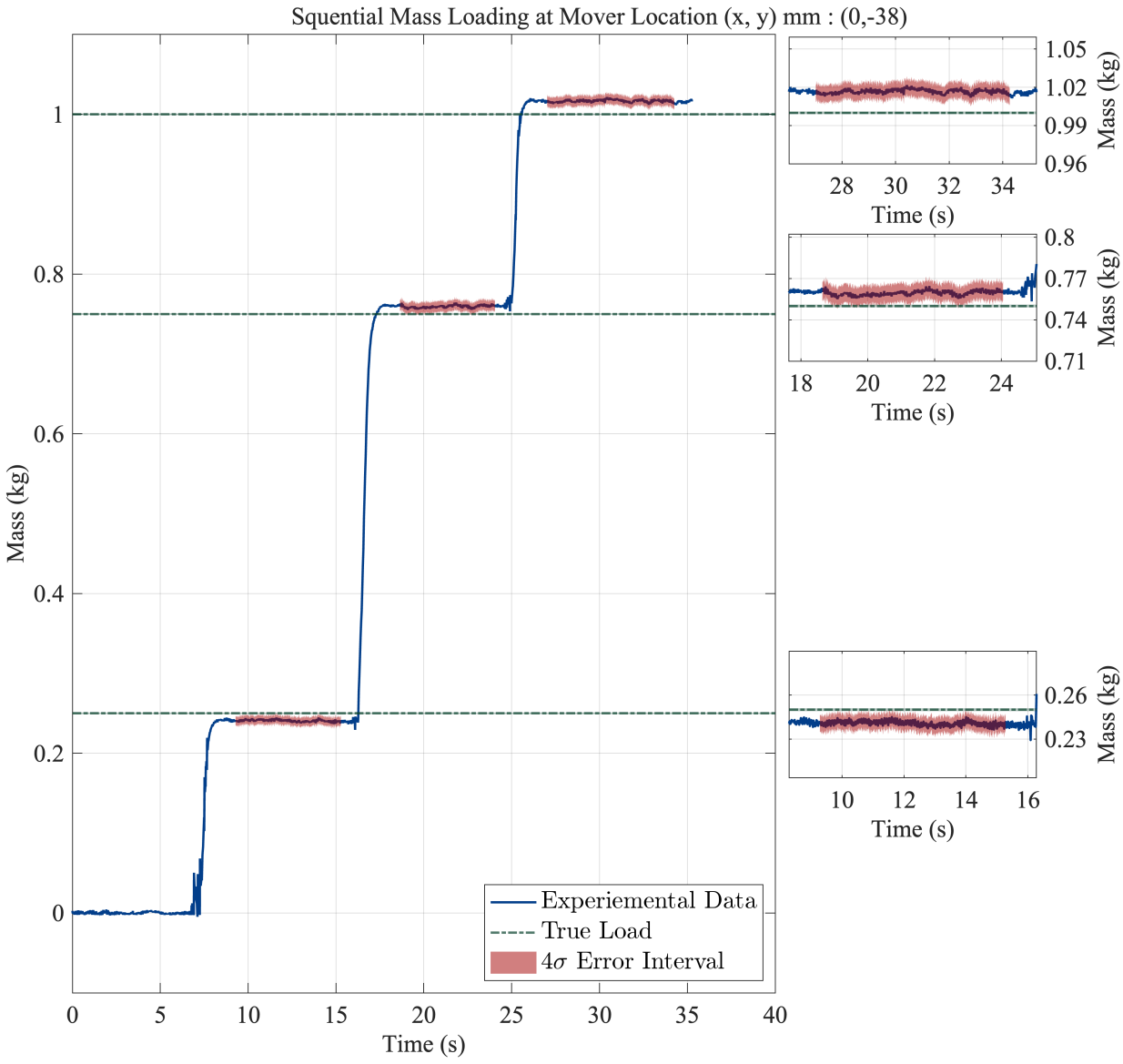



Figure A.5: Summary of successive mass loading performance when the 6-Pole Halbach is between 2 coils. The zoomed-in region highlights the response within the boxed area. Note that the exact loading times between trials were not held constant.

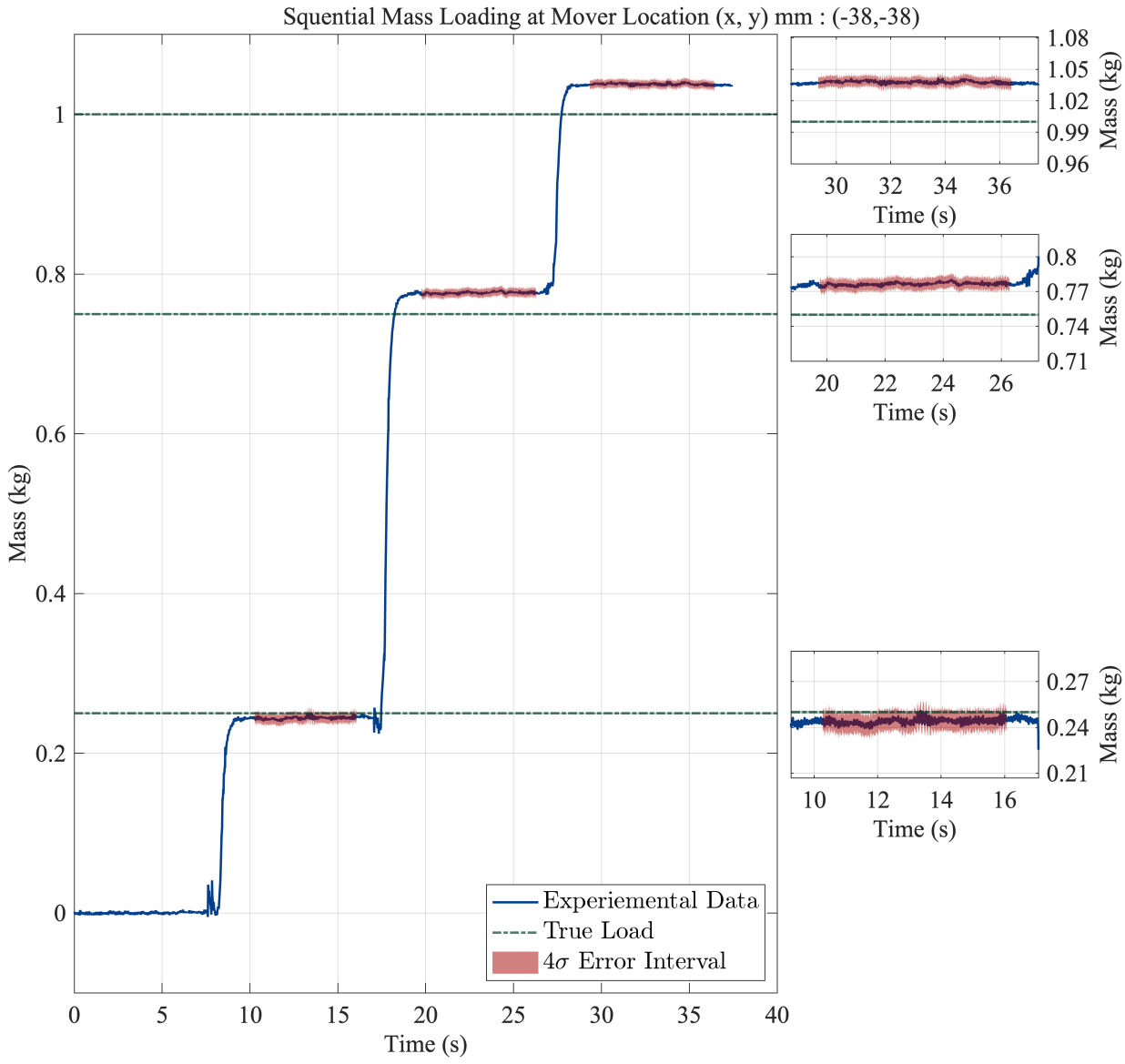



Figure A.6: Summary of successive mass loading performance when the 6-Pole Halbach is above a single coil. The zoomed-in region highlights the response within the boxed area. Note that the exact loading times between trials were not held constant.

# Appendix B

# Extended Description of Mathematical Concepts

## B.1 Statistical Measures

Many statistical measures exist to quantify the discrepancy between measured outputs and a reference ground truth. These metrics differ in their sensitivity to outliers, assumptions about data distribution, and interpretability on the end user. Selecting an appropriate error metric is essential, not only for objective comparison but also for fostering reader intuition when interpreting results. Among the most interpretable metrics for assessing accuracy are those expressed in percentage terms, which provide a direct sense of absolute error magnitude.

One widely used metric in this category is the *mean absolute percentage error* (MAPE), which captures the average absolute deviation of predicted values from actual values as a percentage of the actual values [81]. Given a set of $n$ scalar predictions $F = \{F_1, F_2, ..., F_n\}$ and corresponding actual values $A = \{A_1, A_2, ..., A_n\}$, MAPE is defined as:

$$\text{MAPE} = \frac{1}{n} \sum_{i=1}^{n} \left| \frac{A_i - F_i}{A_i} \right| \times 100. \tag{B.1}$$

MAPE has become a staple for its simplicity, ease of computation, and intuitive percentage-based interpretation. Moreover, it is scale-independent, allowing it to be applied across datasets with varying units. However, MAPE exhibits a significant drawback:

as any $A_i$ approaches zero, the corresponding term in the summation diverges, potentially rendering the overall metric unbounded. This can severely distort the evaluation, particularly in datasets containing small or zero-valued ground truths.

To mitigate this issue, Kim et al. proposed the *mean arctangent absolute percentage error* (MAAPE) [82], a bounded alternative that maintains the benefits of MAPE while enhancing robustness near zero-valued targets. For the same prediction and ground truth sets previously stated, MAAPE is defined as:

$$\text{MAAPE} = \frac{1}{n}\sum_{i=1}^{n} \tan^{-1}\left(\left|\frac{A_i - F_i}{A_i}\right|\right) \times 100. \tag{B.2}$$

This formulation interprets the normalized error as an angular deviation, effectively bounding each term within a finite range due to the asymptotic nature of the arctangent function. As a result, the metric remains bounded across the entire domain even in the presence of extreme errors or near-zero actual values. Like MAPE, MAAPE is absolute, scale-invariant, and computationally efficient, while offering improved resilience to outliers. As shown in Figure B.1, MAAPE offers a slightly more balanced penalty between positive and negative errors than MAPE—the penalty function of MAAPE, like MAPE, is still asymmetric.

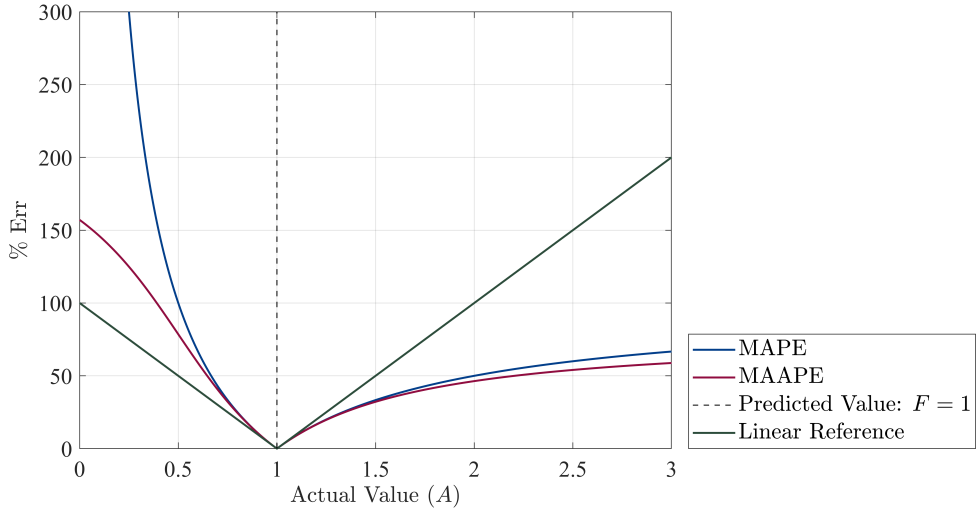



Figure B.1: Behavior of the MAPE and MAAPE statistical measures as the true value approaches zero. A constant predicted value $F = 1$ is used in all calculations. A linear reference line is included to highlight the increasing asymmetry of both error functions near zero true values.

In the context of the magnetic levitation system analyzed in this work, MAAPE is employed to evaluate errors in the estimated loading location of the levitated payload, where true values of zero may occur. Conversely, MAPE is used to assess the accuracy of the estimation in the payload mass itself, as the true values in that case are consistently bounded away from zero—as well, MAPE is more commonly understood by non-technical audiences [83].